Research & Development

2019

This issue is dedicated to Trans-Trio-Sciences international co-operation between Gent, Gödöllő and Baia Mare.
The professional discussion about the published topics were organized in the frame of Synergy 2019 international Conference, Gödöllő, Hungary.
Special thanks go to Hungarian Academy of Sciences, Committee on Mechanical Structures, Subcommittee on Tribology for the organization, too.

Mechanical Engineering Letters, Szent István University

Technical-Scientific Journal of the Mechanical Engineering Faculty,
Szent István University, Gödöllő, Hungary

HU ISSN 2060-3789

Páter K. u. 1., Gödöllő, H-2103 Hungary
dekan@gek.szie.hu, www.gek.szie.hu,

Volume 18 (2019)

This volume contains the selected articles of Trans- Trio Sciences workshop held in the frame of Synergy International Conference, 2019, Gödöllő, Hungary

Synergy 2019, Session : Materials and Industrial Technologies

- materials and testing
- tribology
- industrial technologies

Contents

Experimental results of a small-scale thermal system

Viktor ERDÉLYI[1], János TÓTH[2], László JÁNOSI[1], István FARKAS[2]
[1]Department of Mechatronics, Szent István University,
Institute for Mechanical Engineering Technology
[2]Department of Physics and Process Control, Szent István University
Institute of Environmental Systems

Abstract

This study presents the ongoing research conducted in the field of thermal systems which are commonly used in agriculture and in other fields to utilize the solar thermal energy. This paper describes a small-scale physical system that is controlled by hardware-in-the-loop (HIL) method. In this paper the parameter identification of this small-scale system is presented. The solar thermal input is realized by a heating element, which can provide a 51.15 W power in total. The input energy is controllable via Pulse Width Modulation (PWM) to mimic the stochastic changes in weather. The heat storage unit is a 1 litre in volume isolated tank, which contains also the heat exchanger unit. The working fluid in this system is water which is forced by custom made peristaltic pumps both on the "collector" side and on the output. In this way the mass flow rate of the pump can be controlled on the heat exchanger and on the user side, as well. The user side is modelled by a water-air heat exchanger force-cooled by air with a help of a varying speed fan. The temperatures are measured on several points of the system which are used to control the flow rates. Measurements were done on this small-scale system in order to verify the sub-models of the whole system described by the SimSolar block oriented function library, as follows: solar collector, heat storage, pump. The identified model can be used to simulate various controlling algorithms. This method will be used to select energetically optimal controlling algorithms of real systems.

Keywords

Solar thermal energy, HIL, Simulation, Embedded system, Small scale system

1. Introduction

The development of solar systems has accelerated significantly in recent years. As a result, many experiments have been carried out and many prototype systems have been built. Generally speaking, setting up a physical system to run experiments is extremely costly. Computer-aided modelling techniques can

greatly reduce these costs by drastically reducing the design time and cost of physical systems and control algorithms.

Such solutions have a long history in the automotive industry and are increasingly being used in industrial production. Thus, model-based design may help to optimize our systems [1]. This design method uses mathematical models and their simulation to reduce costs and speed up the test phase [2]. This approach is also useful for analysing and developing an existing solution [3].
To extend the model-based design, in this paper the real system was complemented with (hardware-in-the-loop) HIL simulation, which uses real-time model data as feedback. This can be achieved by embedded systems and sensors. The "hardware" part can be a Field Programmable Gate Array (FPGA) or other embedded system, such as a single circuit board / board integrated computer (Raspberry Pi), or, in this case, a free software and an open source electronics development platform (Arduino) [4]. There are two main approaches to HIL simulation. In the first case, the simulation runs on a single machine, and the embedded system acts as an interface between reality and model space. In this way, complex simulations can be made without the hardware limitation of the embedded system. Alternatively, the entire simulation runs on an embedded system, making the system portable, but this solution requires more advanced hardware due to its increased computing requirements [5].

The aim of the article is to construct a small-scale model and to identify its most important elements (solar collector model, heat storage model) to optimize the usage of renewable heating sources in pig and poultry houses, because heating with fossil fuels is extremely expensive. This method allows us to compare different control algorithms and to find a solution to maintain optimal thermal variables in a pig stall. The presented simulations were performed with the custom written SimSolar software, which provides block-oriented modelling environment [6].

2. Small-scale model

First, a small-scale model of a solar collector unit was created. The precise energy input was assured by the electronic control of the electric heater unit. This heater was used to mimic the real-life collector unit. The domestic hot water tank is heated by the hot water provided by the collector circuit with the help of a water-to-water heat exchanger. A model for domestic hot water usage is a water to air heat exchanger. The model has been designed to allow room for further improvements that may be either planned or required based on test data.
The miniature model uses eight DS18B20 digital temperature sensors for measurement purposes: three in the heat storage unit, one in the collector unit, one at the inlet and outlet points of the collector, one at the output of the user (water-air heat exchanger) and one to measure ambient temperature.

Figure 1. shows a schematic diagram of the experimental device and Figure 2. shows the actual experimental system. Two FDM (Fused Deposition Modelling)

printed peristaltic pumps were used to provide flowrate in both collector and user circuit. Because peristaltic pumps operate on the principle of displacement, they are capable of precisely adjusting the flow rate of the working fluid with the utilized stepper motors. One A4988 stepper motor driver module was used per motor.

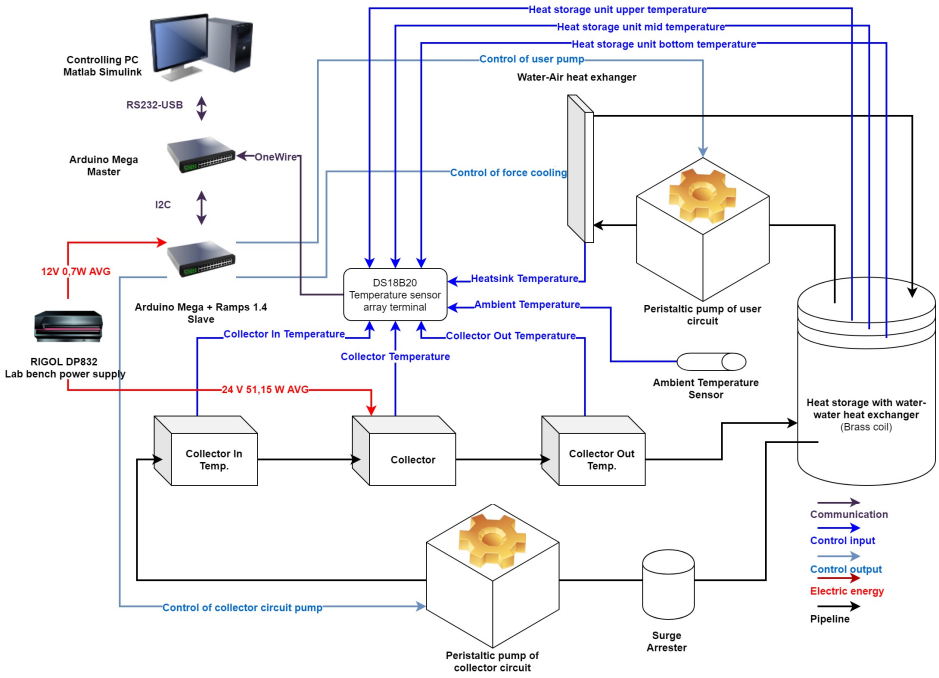

Figure 1. Block diagram of the small-scale model

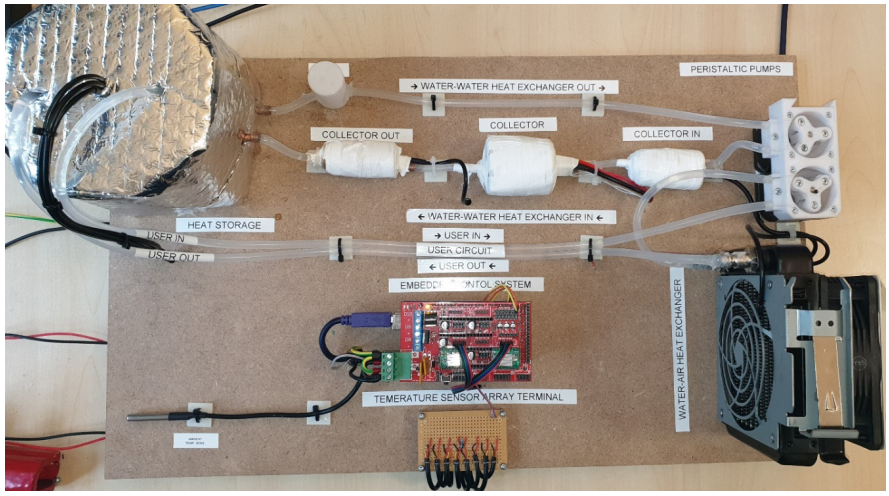

Figure 2. Small-scale model

As a heat reservoir, a polypropylene plastic container insulated with a roof insulation material was used. A copper coil was used as a water-to-water heat exchanger to heat the domestic hot water with the energy carried by the working fluid in the collector circuit.

During the measurements the temperature rise of the heating cycle was examined. An average heating power of 51.15 W was used to heat the collector circuit fluid and the collector circuit pump was driven at 316 rpm, representing 0.357 l min^{-1} flow rate thus 0.0059 kg s^{-1} mass flow rate:

$$\frac{dV}{d\tau} = v\, L\, N\, n\,. \tag{1}$$

Due to the characteristics of the small-scale model, the power input of the heater is approximately 10% of the average heating power per square meter of a real solar collector, so the model was subsequently applied in a scale of 1:10.

3. Models of the solar system

The mathematical models used in the identification, which are part of the SimSolar library, are described below. All the important elements of the system, such as the solar collector, the heat storage tank and the pumps were modelled. The indicators, that characterize the quality of identification will be also presented.

Model of the collector

In solar thermal systems, solar collectors convert the radiant energy of the sun into heat. Therefore, these devices are the main components of the system, as the system is designed to optimally capture and transport energy, which is primarily done here. The model of a solar thermal collector of the SimSolar library is presented.

The Hottel-Vhillier model [7] is interpreted as shown in Figure 3.

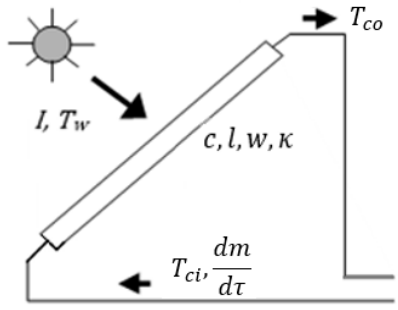

Figure 3. Schematic diagram of the solar collector model

The mathematical model can be written as:

$$T_{co}(\tau) = T_w(\tau) + \frac{I(\tau)}{\kappa_{aw}} + \left(T_{ci}(\tau) - T_w(\tau) - \frac{I(\tau)}{k_{aw}}\right) exp\left(-\frac{\kappa_{mw}\ w\ l}{c_m\ \frac{dm}{d\tau}}\right). \quad (2)$$

Model of the heat storage

Heat storages are an important element of the solar thermal system, as the time of the usage of the collected energy does not necessarily coincide with the time of the collection, so this energy must be stored for later use.

The interpretation of the heat storage model [7] is shown in Figure 4.

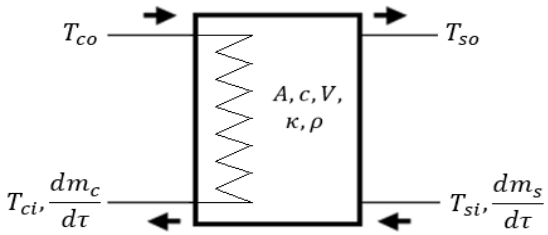

Figure 4. Schematic diagram of the heat storage

$$T_{ci}(\tau) = \left(T_{co}(\tau) - T_{so}(\tau)\right) exp\left(-\frac{\kappa_s\ A_s}{c_s\ \frac{dm_c}{d\tau}}\right) + T_{so}(\tau), \quad (3a)$$

$$c_s\ V_s\ \rho_s\ \frac{dT_{so}}{d\tau} = c_s\ \frac{dm_s}{d\tau}\ \left(T_{si}(\tau) - T_{so}(\tau)\right) + c_s\ \frac{dm_c}{d\tau}\ \left(T_{co}(\tau) - T_{ci}(\tau)\right). \quad (3b)$$

Among the parameters in the model, measurement-based identification was required for the κ_s heat transfer coefficient, while the other parameters were known.

Model of the pump

The pump circulates the working fluid in the system, which allows the flow of the liquid through the collector circuit to be controlled. The current pump model describes a pump with a linear characteristic, i.e. the output mass flow rate is the product of the maximum mass flow rate and the control signal:

$$\frac{dm}{d\tau} = \frac{dm}{d\tau}_{max}\ u(\tau). \quad (4)$$

Parameter identification was not required for this model as the pump was running at maximum speed throughout the measurement, for which the mass flow was known.

Quality indicators

Mean and maximum deviation measures were used to estimate the accuracy of the identification. These are defined as follows:

The mean deviation expresses the difference between the *T* measured and the *T'* simulated results over the entire simulation time interval, which contains $n > 0$ measurement points, and is thus suitable for evaluating the accuracy of the models:

$$\varepsilon = \frac{1}{n}\sum_{k=1}^{n} abs(T(k) - T^{'}(k)). \tag{5}$$

In addition to estimating the full interval, maximum deviation is also an important feature of the identified model to determine whether the mathematical model is capable to achieve the desired accuracy. The definition of the maximum deviation is:

$$\Delta = max(abs(T(\tau) - T'(\tau))). \tag{6}$$

4. Identification of the Model of the System

The objective of the identification task is to determine the unknown parameters of the model based on the measurement results so that the simulation with the specified parameters is as close as possible to the measurement results. To accomplish this task, we define the quadratic deviation as a target function of the studied $[\tau_0; \tau_1]$ interval [7]:

$$J(p_1,p_2,\ldots,p_j) = \int_{\tau_0}^{\tau_1} \left(y(t) - y'(t,p_1,p_2,\ldots,p_j)\right)^2 dt. \tag{7}$$

Measurements were made at discrete time points, and the simulation uses a numerical solution, so the discrete form of the target function was used, which, for *n* measurement points, is:

$$J(p_1,p_2,\ldots,p_j) = \sum_{k=1}^{n} \left(y(k) - y'(k,p_1,p_2,\ldots,p_j)\right)^2. \tag{8}$$

The purpose of the actual execution of the identification task is the objective function, which should be minimized by specifying the actual parameters:

$$\min_{p_1,p_2,\ldots,p_j} J(p_1,p_2,\ldots,p_j) \longrightarrow p_1,p_2,\ldots,p_j. \tag{9}$$

The small-scale system was identified in two parts. Based on the measurement data, first the solar collector then the heat storage was identified. The measurement data used to solve this problem is shown in Figure 5, which is the collector, storage, and ambient temperature values. Mathematical sub-models are included in the SimSolar Simulink library [8]. The simulation was done in a block-oriented way, which greatly facilitates the application of control algorithms to real systems in the HIL approach.

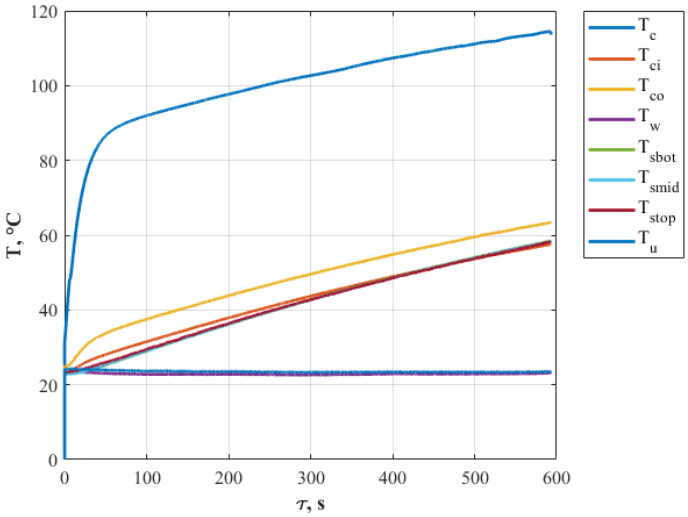

Figure 5. Measurement data used for identification

5. Results

During the identification of the small-scale system, the heat transfer coefficients of each element were identified, the other parameters being either directly measurable or available from the manufacturer's catalogue.

As described earlier, due to the nature of the solar system as a substitute for the solar collector, its length and width cannot be interpreted, so we have set these values to 1 for the correct operation of the model. This assumption was used to convert the input energy into irradiation-like energy, which was determined to be 511.5 W m^{-2}.

Other technical parameters of the solar collector:

- pump mass flow rate: 0.0059 kg s^{-1}
- working fluid: water.

Technical parameters of the heat storage with heat exchanger:

- storage volume: 10^{-3} m^3,
- storage area: 0.2674 m^2,
- initial temperature: 22.9°C,

– pump mass flow rate: 0.0059 kg s^{-1}
– working fluid: water.

The result of solar collector identification is shown in Figure 6. The mean deviation of the identification is 1.0°C and the maximum deviation is 5.3°C, which is sufficiently accurate for further testing. The heat transfer coefficients κ_{aw} and κ_{mw} of the collector are 6.31 W m^{-2} K^{-1} and 2.41 W m^{-2} K^{-1}, respectively. The difference between the values of the identified parameters for the model and the same type of parameters for real solar collectors can be explained by differences in the similarity of the systems.

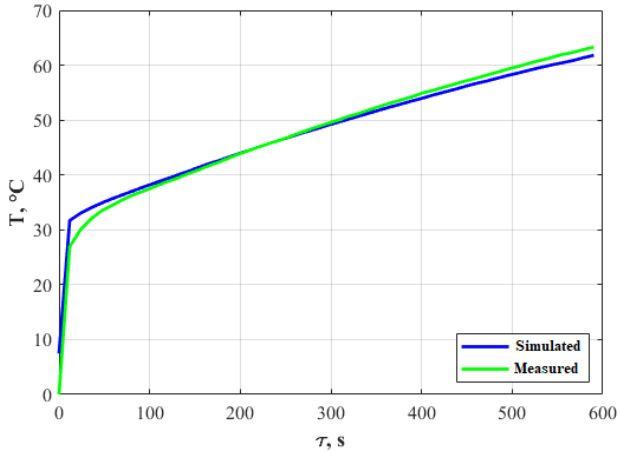

Figure 6. Collector simulation and measurement results

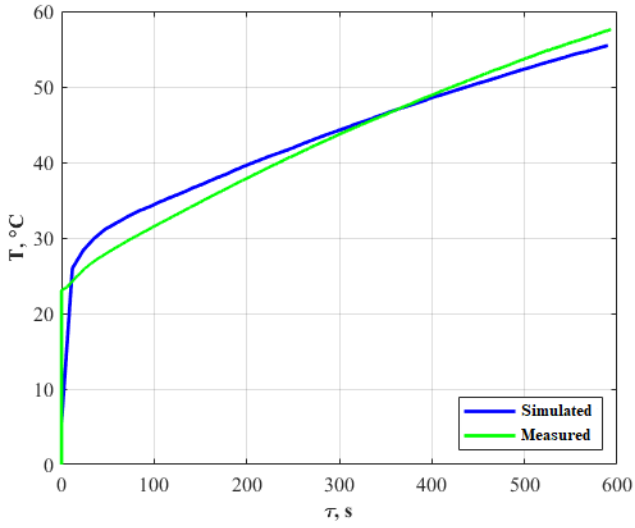

Figure 7. Simulation and measurement results of the heat storage

The result of the heat storage identification is shown in Figure 7, with an average deviation of 2.6°C and a maximum deviation of 4.3°C, which corresponds to the accuracy required for further tests. The identified storage κ_s have a heat transfer coefficient of 24.79 W m^{-2} K^{-1}. The average temperature of the reservoir was used for identification.

Summary

In the present work, a small-scale model for a solar thermal system was made on which HIL measurements were performed. The measurement results were used for parameter identification of the mathematical models of collector and heat storage from the SimSolar library.

The heat transfer coefficient between the absorber and the environment in the solar collector model was determined to be 6.31 W m^{-2} K^{-1} and the value of the heat transfer coefficient between the working fluid and the environment was 2.41 W m^{-2} K^{-1}. The results obtained are based on the specificity of the heat input solution used in the small-scale model and the electric heating unit used as a virtual solar collector.

The average heat transfer coefficient (24.79 W m^{-2} K^{-1}) of the heat storage tank was determined by averaging the values of the temperature measuring points in the tank.

The accuracy of the results obtained is acceptable from an engineering point of view. This means that the small-scale system can now be treated as a physical-based model, providing the opportunity for further investigations to select optimal control algorithms.

The method thus created also provides the opportunity to identify real systems, that is, the tests can be extended to real solar thermal systems and thus the optimization of control algorithms on the small-scale system can be generalized.

References

[1]Paterno, F., (2012). Model-based design and evaluation of interactive applications, ISBN: 978-1-447-10445-2

[2]Erdélyi. V., Jánosi. L. (2017). Digital twin and shadow in smart pork fetteners, Proceedings of the 5 th International Scientific Conference on Advances in Mechanical Engineering, Debrecen, Hungary, ISBN 978-963-473-304-1 pp. 142-146.

[3]Bilčík, M. Božiková, M., Petrović, A., Malínek, M. Cviklovič, V., Olejár, M. Ardonová, V. (2018). Analysis of selected photovoltaic panels operating parameters as a function of partial shading and intensity of reflected radiation, Acta Technologica Agriculturae, Vol. 21, pp. 14–17.

[4]Velasquez, D.R., Collazos, V.T., Mines, J.M. (2017). A low-cost hardware-in-the-loop real time simulation of control systems, Proceedings of the 2017

IEEE 24th International Congress on Electronics Electrical Engineering and Computing, INTERCON 2017, ISBN 978-150906362-8

[5]Ilyas, A., Ayyub, M., Khan, M.R., Jain, A., Husain, M. (2018). Realisation of incremental conductance the MPPT algorithm for a solar photovoltaic system, International Journal of Ambient Energy, Volume 39, Issue 8, pp. 873-884, ISSN: 0143-0750

[6]Tóth, J., Farkas I. (2017). Developing a Simulink library for solar energy applications, R&D in Mechanical Engineering Letters, Gödöllő, Hungary, Vol. 16, pp. 89-95. HU ISSN 2060-3789

[7]Farkas I. (1999). Számítógépes szimuláció, 45-68. o

[8]Tóth J., Farkas I. (2018). Blokk-orientált szimulációs keretrendszer napkollektoros alkalmazások vizsgálatára, Energiagazdálkodás, 59. évf., 5. sz., 24-29. o. ISSN: 0021-0757

Non-destructive inspection methods of diffusion bonding on 1.4404 specimens welded in a Gleeble 3800 thermomechanical simulator

Tétény BAROSS[1], Péter BERECZKI[2], László JÁNOSI[3], Miklós PALÁNKAI[1], Botond SÁNTA[4], Gábor VERES[1]

[1]Wigner FK RMI, PO Box 49, H-1525 Budapest, Hungary,
[2]Department of Material Science, University of Dunaújváros,
[3]Department of Mechatronics, Szent István University,
[4]Department of Physics, Budapest University of Technology and Economics

Keywords

diffusion bonding, non-destructive methods, Gleeble 3800 physical simulator, creep deformation

Abstract

Diffusion bonding methods are the one of the candidate welding methods for Plasma Facing Components(PFC) in fusion reactors. The reliability of these joints can be crucial in a reactor environment since the low maintainability of the PFC components. For diffusion bonding methods the Gleeble 3800 thermomechanical simulator can provide an advantageous experiment compared to having a furnace with radiation heating and axial forces in a vacuum chamber – the heating is performed by Joule heating with 50 Hz alternating current passed through the specimens by grips at the ends. Gleeble System is applies direct resistance heating up to 10,000°C/second and apply maximum static pressure 20 t [Uniduna, 2016] under mid 10-5 Torr range.

With the two prepared 1.4404 samples the possible non-destructive methods were studied to be able to validate the welded joints in nuclear environment. The article summarizes two non-destructive methods of specimens as the four point electrical resistance test and thermal conduction tests. In future work the non-destructive methods shall be examined on welded specimens.

1. Introduction

Diffusion bonding method is a very promising method for same or different materials, where large surfaces have to be welded or the mating materials have different thermal properties. The reliable welded surface is crucial also in view of thermal conduction since the fusion reactor first wall elements have to withstand the large 1-2.5 MW/m^2 heating power. So the non-destructive methods on the 1.4404 samples were developed for the conduction properties of the samples.

For diffusion bonding methods the Gleeble 3800 thermomechanical simulator can provide an advantageous experiment compared to having a furnace with radiation heating and axial forces in a vacuum chamber, where the heating is performed by Joule heating with 50 Hz alternating current passed through the specimens by grips at the ends. Gleeble System is applies direct resistance heating up to 10,000°C/second and apply maximum static pressure 20 t [Uniduna, 2016] under mid 10-5 Torr range.

The article summarizes the non-destructive methods of specimens as the electrical resistance and thermal conduction tests were performed on prepared samples. With calculation the difference of electrical resistance was validated and it was shown that the thermal measurement's sensitivity is enough for further specimens.

2. Physical simulations on Gleeble 3800 thermomechanical system

A Gleeble 3800 thermomechanical simulator (Dynamic Systems Inc.) is a physical simulator of material behavior, which is able to combine heating and mechanical loading in different scenarios. This is allowed the system to simulate physically the diffusion bonding process. The author of the article has the possibility to make these diffusion weldings in a Gleeble labor at University of Dunaújváros in Hungary.

The HIP hot isostatic pressing a type of diffusion bonding applies two phenomena in one time: the elevated temperature under recrystallization and isostatic pressure, however in labor environment the isostatic pressure is changed to uniaxial pressure of flat components perpendicular to the two contact surfaces.

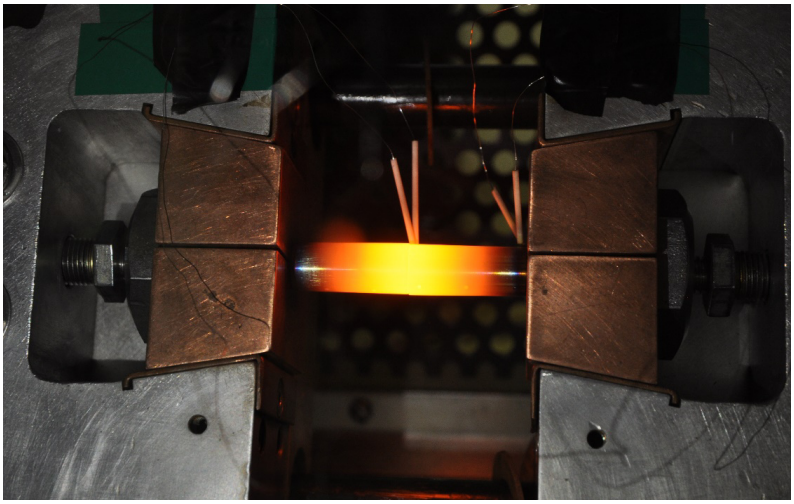

Figure 1. Diffusion bonding in a General Purpose Mobile Conversion Unit of Gleeble 3800, [Gleeble lab, UNIDUNA]

During the process mating surfaces are planarized under pressure. Bond takes place by deformation and diffusion processes at the bond interfaces, where under 50-80% of the melting temperature Tm and specific pressure 10-50 Mpa – molecular activity increases and supports the diffusion processes under 60-120 min. Due to the long process and high temperature the continuous contact of bonding surfaces thanks to several diffusion processes the surface roughness and voids disappear.

3. Non-destructive tests of diffusion bonded specimens

Four point resistance test were performed on two prepared specimens for testing the reliability of the surface resistance measurement.
Similar to the electrical resistance tests thermal conductance tests were performed on the same prepared specimens for testing the sensitivity of the measurements.

Electrical resistance test
For the measurements we have prepared two specimens. For simulation of the welded edge additional 12 holes were drilled into the middle of one specimen Nr. (2), decreasing the full cross-section of the original one and increasing the electrical resistance. The other reference specimen (1) has the same geometry without holes. The holes for electrode screws and the base materials are the same for both cases.

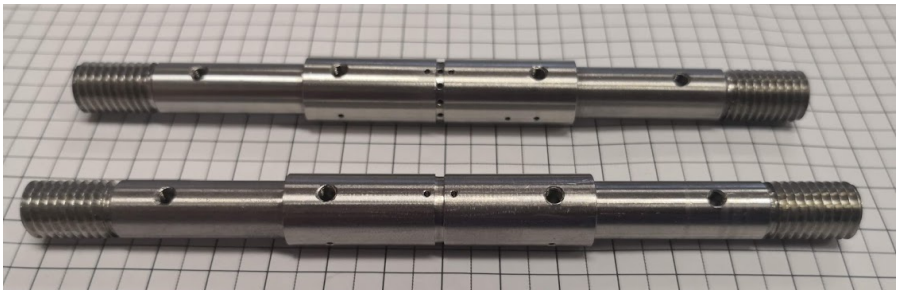

Figure 2. Simplified geometry for the electrical resistance without and with holes

Modelling of the electrical resistance
It is worth to estimate the expected order of magnitude of the electrical resistance before the measurements. Both specimens were approximated with the following model. The specimen was divided into three section, look at Figure 3.,where the drilled holes only in the middle section were modelled, in any other cross-sections the body modelled as full cross-sectional solid.

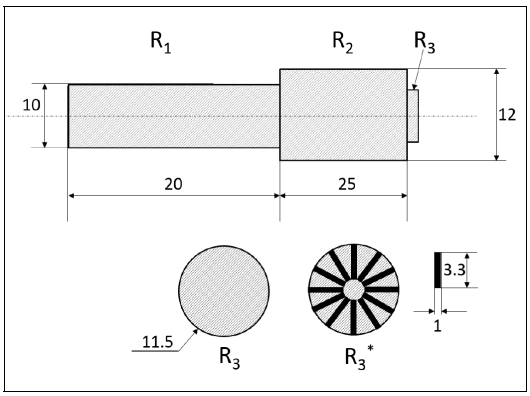

Figure 3. Simplified geometry for the electrical resistance without and with holes

In this way the approximating with cylinders the electrical resistance can be calculated easily with the following equation:

$$R = \rho \frac{l}{A},$$

where the length of the cylinder is l [mm], A is the cross-section $\rho = 0.074 \cdot 10^{-6}$ Ωm is the specific electrical resistivity of the 1.4404 stainless steel [1]. The resistance of the full specimen will be calculated as a series electrical circuit, where the middle section deviate in the two specimen. So the sensitivity of the measurement shall be important for the exact and reliable results.

Following the rough geometry and the calculations the results are shown in Table 1. The resistance difference is quite small of the order of $10^{-6} - 10^{-7}$, maximum 1 % difference may be measurable.

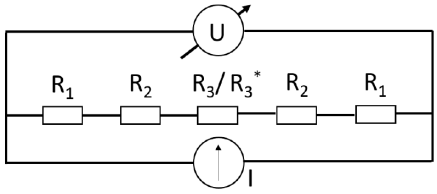

Figure 4. Four point electrical resistance measurement, equivalent electrical circuit of the specimens

Measurement and evaluation

Since the order of magnitude is so small that only the four point electrical resistance measurement is reliable for a this kind of measurements. In the BME laboratory a Keithley 2001 High Performance Multimeter was used. According to the datasheet the resolution was 1 μΩ and the accuracy is 52+7 ppm in this

mode of operation [2]. During the measurement even the contact resistance may give larger electrical resistance compared to the welded surface. The instrument lead through the specimen current in the range of 9.2 mA, where the resistance is 0.1 mΩ. So the voltage is in the range of 1 μV as well.

If we raise up the current than the voltage / potential difference will raise up also, and parallel the relativistic failure of the current generator will decrease too. In future measurements a Delta ES 015-10 current supply shall be used, which is able to produce 10 A. The Keithley 2001 High Performance Multimeter was used, where in this operation mode the current resolution was 10 nV and the accuracy 25+6 ppm according to the datasheet [2]. The measurement setup is visible on the Figure 5.

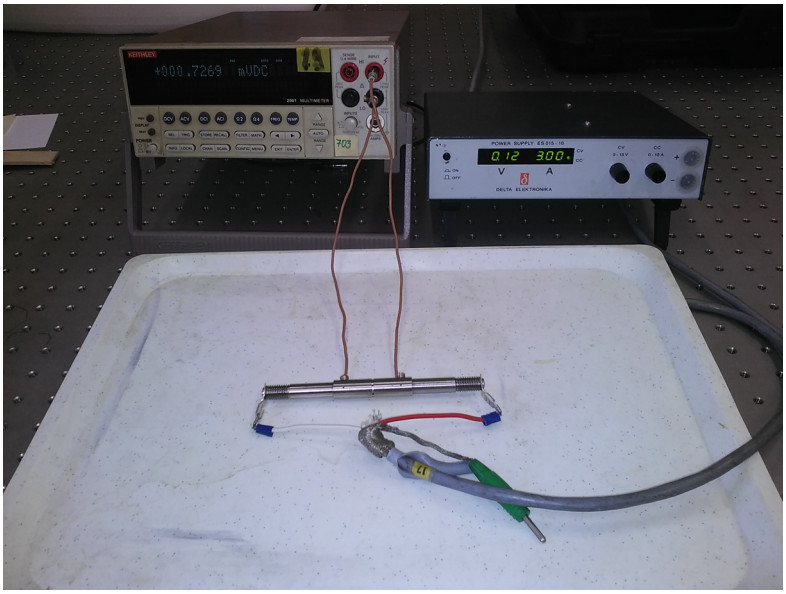

Figure 5. Four point electrical resistance setup

The greatest errors come definitely from the different fixing of the probes, electrodes. So 3-3 measurement series were performed to calculate an average voltage. The electrodes were unfixed and fixed. The current was raised up step by step with 1 A to eliminate the offset errors of multimeter. The results are shown on Figure 6, 7. The measured results are separable for the two specimens in both cases.

There are a 3 or 6 times difference between the calculated and measured electrical resistance, see Table 1. The reasons can be the following:

- Not perfect homogenous material
- The neglected holes, simplified geometry
- The overestimation of the middle section

– The manufacturing tolerances
– Contact resistance

Table 1. In the 2nd and 3rd rows the estimated electrical resistances on (1) and (2) specimens in the A and B probe positions; in 4th the difference is visible in % ; In the 5th and 6th rows the measured electrical resistances on (1) and (2) specimens in the A and B probe positions, in 4th the difference is visible in %

Pos.	$R^{(1)}$ (μΩ)	$R^{(2)}$ (μΩ)	ΔR(μΩ)	ΔR
A	109,06	109,72	0,66	0,60%
B	71,47	72,13	0,66	0,91%
Pos.	$R^{(1)}_{meas}$ (μΩ)	$R^{(2)}_{meas}$ (μΩ)	ΔR_{meas} (μΩ)	ΔR
A	723,35 ± 0,148	728,29 ± 0,103	4,94	0,68%
B	233.23 ± 0,039	240,25 ± 0,0523	7,02	2,92%

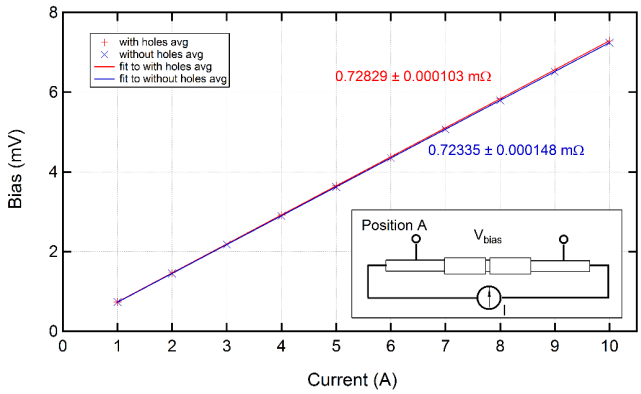

Figure 6. The two voltage / current curve probes at A points

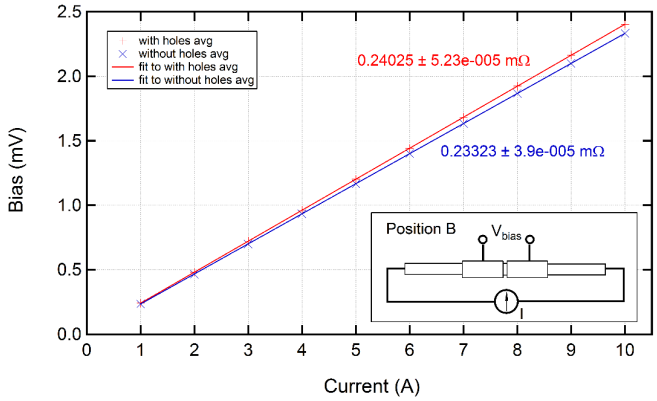

Figure 7. The two voltage / current curve probes at B points

In case one want to refine the electrical resistance calculation, the FEM is a viable solution to estimate the real electrical resistance.

Thermal conductance test

Similar to the electrical resistance tests several thermal conductance tests were performed on the above mentioned two prepared specimens for testing the sensitivity. The thermal test setup is made up of an induction heater, a ferromagnetic sample, the specimens, the two copper block for the better thermal conduction and a K type thermocouple system. The setup is visible on Figure 8.

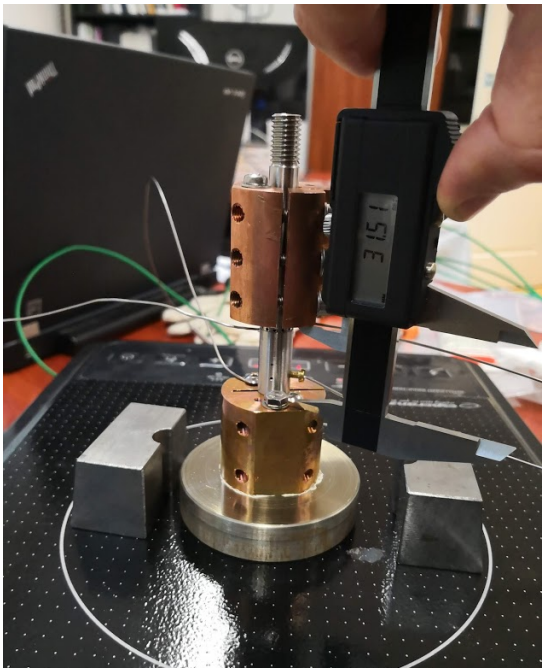

Figure 8. The heat conduction test of specimens (1),(2) at same conditions

The measured results are shown in Figure 9. During the measurements there are several uncertainty: as the convection flow around the measurement setup, the thermal contacts and the induction heater's precision. The induction heater is regulable to several temperature: 80 C, 100 C, 130, 160, but the precision of the control loop is not able to keep the temperature between 10 C degree. Furthermore the changing environment is like room temperature makes unstable the measured values. In this way the robustness of the measurement setup was a crucial point. Hereby two copper block (upper and lower) were installed to increase the temperature difference raising through the middle section, which would simulate a similar condition of a diffusion bonded specimen.

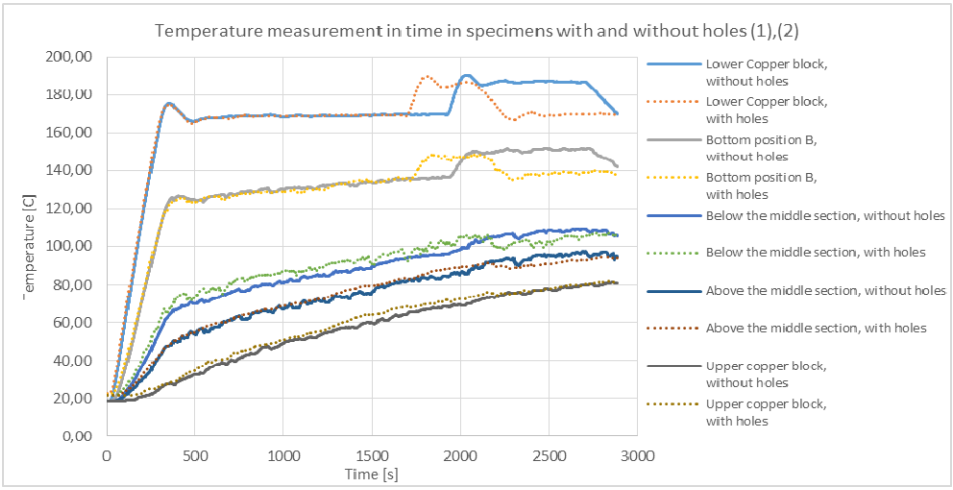

Figure 9. Temperature measurement (transient) with and without holes

Since the absolute temperature difference is not comparable the relative differences were investigated on the next Figure 10. The results clearly shown that the specimen with holes has larger difference via the full measurement.

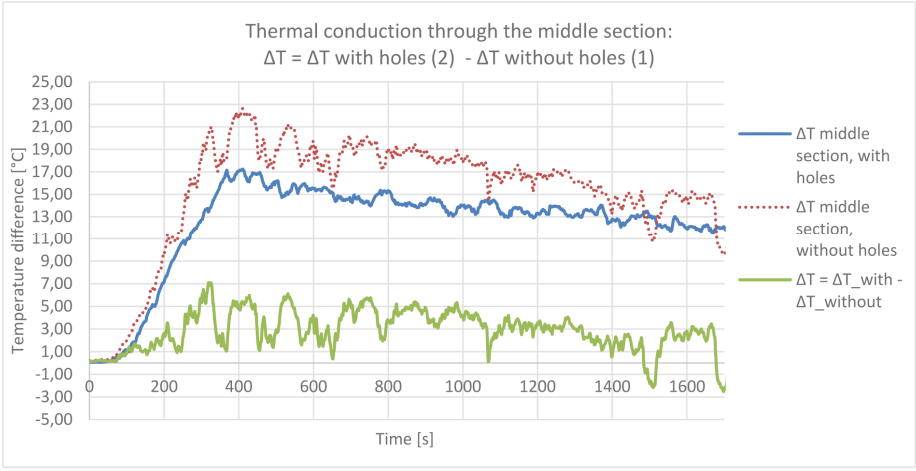

Figure 10. Temperature measurement (transient) with and without holes

The average of the thermal conduction difference (green) is at present case 2,9 C. For future work we have started to prepare a measurement setup under vacuum conditions to exclude the natural air convection around the measurements, however the vacuum condition may worsen the contact properties.

Conclusions

Electrical resistance

The measured values are close to the estimated ones in view of the percentage difference between the two specimens (specimen with holes and without holes). However the electrical resistance much larger compared to the expected, the tendencies of the two positions: A, B are similar at both specimens: (1), (2). The B position is more proper for the measurement, because of the relative difference at the two specimens. But the A position is similarly good for validation for the diffusion welded specimens, which is favourable for future technical setups.

Thermal conduction tests

The measurement was performed under room conditions, where the air cooling from convection has a significant influence on the measurement stability. In this way similar measurements are envisaged under vacuum conditions to make a more precise measurements. However the results indicated that the sensitivity is enough to detect much smaller holes between the two welded specimen.

Summary

The diffusion bonding with 1.4404 specimens were performed in a Gleeble 3800 GTC physical simulation. Probably the joined surface with different percent of bonded area has different thermal and electrical conductance that have to be measured by standard, but sensitive methods. Since the diffusion welding of 1.4404 are well known - development of non-destructive test methods are worthwhile to prepare first on a standard material, that can be extended to a material developed for a fusion reactors. The above introduced methods could demonstrate that under strict condition they are able to measure even much smaller defects of the mating surfaces.

In the future work: non-destructive test methods shall be able to verify the bonded percentage of the specimens.

References

AALCO, Stainless Steel - Austenitic - 1.4404 Bar and Section http://www.aalco.co.uk/datasheets/Stainless-Steel-14404-Bar-and-Section_39.ashx

Keithley 2001 datasheet http://www.testequipmenthq.com/datasheets/KEITHLEY-2001-Datasheet.pdf

Uniduna, Gleeble labor description, 2016, internet link: www.uniduna.hu/images/dokumentumok/Gleeble_labor.pdf

Tétény Baross, László Jánosi, Gábor Kalácska, Gábor Veres, Diffusion bonding of plasma facing components of fusion reactor (ITER), Mechanical

Engineering Letters, Szent István University, Volume 12 (2015), page 101-109, HU ISSN 2060-3789

T. Baross, L. Janosi and G. Veres, Analytical and numerical model of the temperature distribution of diffusion welding specimens on a Gleeble 3800 thermomechanical simulator, Mechanical Engineering Letters, Szent István University, Volume 15 (2017), page 16-26, HU ISSN 2060-3789S.

V. Barabash et al., Summary of Material Data For Structural Analysis of the ITER Vacuum Vessel and Ports, 2013

Abrasive wear of filled polymer composites: A brief review

József DOBOS, Róbert KERESZTES
Institute for Mechanical Engineering technology, Szent István University

Abstract

The main objectives of our brief review were to compare the tribological properties of composites and to investigate the effect of different additives and mechanical properties. Abrasion wear is one of the most common failure mechanisms of moving machine elements. Because of their mechanical and tribological ability, engineering polymer composites can be chosen to replace metal partsin certain applications (e.g. bearings). It was found among other things that the fillings (glass fibres, graphite, carbon fibres, molybdenum disulphide, slag, etc.) have a favourable effect on composites. The tests of compared articles were prepared using the pin on plane and ball on plane tribotesting system, tested on different load.

Keywords

composite, filling, abrasion, tribology.

1. Introduction

Engineering infrastructures have shown very rapid growth in recent years and this is probably due to the increasing population demands (Rajasekar et al., 2019). Abrasion wear is one of the most common failure mechanisms of moving machine elements. Because of their mechanical and tribological ability, engineering polymer composites can be chosen to replace metal parts in certain applications (e.g. bearings). In the present brief review three groups of polymer composites (PA 6, PEEK with different mechanical properties) and four composites with filled industrial slag, are experimentally investigated by abrasion tribotesting. The main objectives of this study were to compare the tribological properties of composites and to investigate the effect of different additives and mechanical properties. The different article tests were prepared using the pin on plane model system, tested on different loads (11.5 N and 23 N where the abrasion mating surface was emery cloth), and ball-on-disk tester under the loads of 10, 15 moreover 20 N. It was found among other things that the fillings have a favourable effect on composites. The short carbon fibres proved better for improving wear resistance as compared to short glass fibres. Recently, the industrial sector has grown rapidly, producing a large amount of

by-products, which have harmed the environmental balance and have become a major problem for disposal (Rajasekar et al., 2019; Singh et al., 2017). Slag has become a major problem for the sustainable development of the metal manufacturing industry (Cao et al., 2019). Slags are undesirable by-products float above the steel which consist of ionic solutions of molten metal oxides and fluorides. The slags have positive or negative effects on the metal production industry. Components such as SiO2, Al2O3 and sulphur are considered slag components that reduce the quality of the steel. The slag has a special role in steel production. The slag minimizes heat loss by staying on the liquid steel and protects the metal from oxidation, nitrogen and hydrogen absorption. In this work industrial slag used as a filling material to increase the mechanical behaviour of composites and save the industrial by-products. By-products and waste disposal can best be supported by recycling.

2. Experimental with filled slags

The epoxy resin was poured into beakers. Blast Furnace Slag (BFS), Converter Slag (COS), Ferrochromium Slag (FeCrS) and Al_2O_3 microparticles sized 61 mm were added into the resin.

In order to determine the friction and wear behaviour (dry condition) of the composites under various loads, the ball on disc type wear test and friction monitor were used.

Wear performance of the composites was examined under dry sliding conditions against a Al_2O_3 ball under 10, 15 and 20 N loads.

Wear tests were performed at room temperature with a sliding speed of 5.4 cm/s along a circular path of 5 mm in radius for a total of 300 m sliding distance. The Al_2O_3 ball had sphere geometry with a diameter of 6 mm and with 2000 Hv hardness. Samples were machined in 30 mm 7 mm x 6 mm geometries for wear tests.

Figure 1. Abrasion testing equipment

Table 1. The chemical compositions of Al_2O_3, BFS, FeCrS and COS powders.

Powders	Components (wt.%)								
	SiO_2	Al_2O_3	Fe_2O_3	CaO	MgO	Cr_2O_3	Mn_2O_3	Ignition loss	Others
Al_2O_3 (S1)	e	98.51	0.41	e	0.21	0.05	0.02	e	0.8
BFS (S2)	39.99	10.51	3.49	31.55	5.95	0,02	3.55	e	4,94
FeCrS (S3)	28.48	21.59	3.51	0.62	36.52	6.95	0.2	0.6	1,53
COS (S4)	17.62	4.03	23.81	30.39	4.56	0.13	3.04	12.99	3,43

At light loads, the temperature caused by the friction between the abrasive and the composite remains low. The low temperature prevents the softening of the epoxy matrix, which has a low melting temperature. Together with the increased load, volume losses of the samples are also increased. The increase of the load on the ball on disc device, the normal force value on the ball will increase. At high loads, adhesion between the abrasive ball and the asperities of the composite material as well as the immersion depth of the ball will increase. More material accumulates in front of the shear stress that forms a plastic flow, and when shear forces reach a critical level, it breaks off the material displacing it out of the system. Dry sliding wear behaviors of polymer-based composites should be considered as a function of load, velocity, distance, temperature and tribochemical reaction at elevated temperatures (Samyn and Zsidai, 2017; Megahed et al., 2018). The volume loss in composites under 10N load occurred in the following order: S1> S4> S3> S2 (Fig. 2.)

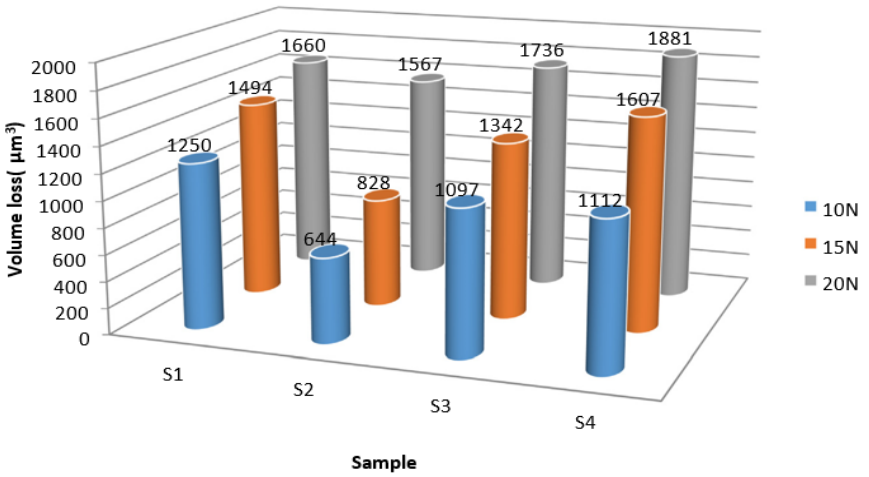

Figure 2. Volume loss as a function of varying load for composite samples.

The cylindrical specimens are in conformal connection with the abrasive (emery cloth). The components of composites are homogenously spread in the bulk of polymers.

3. Experimental with composites

Another Tests were conducted with normal load 11.5 N and 23 N and the running time 240 s (with emery cloths abrasive DEER XA 167 AA-100.) The selection of the tested seven polymers and composites were made by cutting an 8mm diameter and a 10-15 mm length. The materials can be divided into two main composites groups.

- The extruded type polyamide PA 6E were used as a reference material in the investigations. The product can be regarded as a polyamide type "for general use".
- The PA 6G ELS is the conductive version of magnesium catalysed cast polyamide 6.
- In comparison the PA 6MO (PA 6E+MoS2) with the PA 6E material, it has a higher degree of strength and rigidity due to the molybdenum disulphide (MoS2) content. Its heat and wear resistance is better, but its toughness and mechanical damping ability is worse. It can be readily machined with automatic cutting machines.
- PA 6 Glide is a hard-semi-crystalline cast thermoplastic with a lubricant addition. It has good sliding properties, wear resistance, better tensile strength and machinability than PA 6E. Typical applications are (e.g. gears, rollers, cable rollers, universal material) wherever there are no special requirements.
- Natural, unfilled PEEK (polyetheretherketone) is a semi-crystalline advanced material that exhibits a unique combination of high mechanical properties, temperature resistance, and an excellent chemical resistance. The main properties are a high service temperature (permanently around 250 °C, briefly to 310 °C can be used), high mechanical strength, stiffness, excellent chemical, hydrolysis, wear resistance and good dimensional stability.
- PEEK PVX is a real bearing grade. It is filled with carbon fibres (CF), PTFE and graphite.
- PEEK GF30 composite contains 30% glass fibre (GF) reinforced for greater dimensional stability and higher strength properties.

The effect of adhesion decreases with increasing load and increasing surface roughness. In our case the abrasion now becomes more important. The abrasion wear results of the tested polymers are shown in the Figure 3.

We can compare these results. It can be observed from the figure that the higher load increases proportionally (~1.6 times) in the wear of most of tested polymers. In this study, dry sliding wear behaviors of epoxy matrix composites reinforced with Al_2O_3, BFS, FeCrS and COS under different loads were investigated. S2 composite showed the best wear resistance under all loads. This was followed by S3, S4 and S1 composites under 10N load. Under 15N load, the ranking of the wear resistance was S2> S3> S1> S4, and under 20N the ranking was S2> S1> S3> S4. In the S1 and S2 composites, fatigue-based plastic deformation was observed while in the S3 and S4 composites, smoother surfaces, transverse cracks and removed reinforcing particles were observed.

The coefficient of thermal conduction of the composites was determined as S3> S1> S2> S4. No proportional correlation was found between the coefficient of thermal conduction and volume loss. Produced slag reinforced composites generally exhibited closer or better tribological properties than alumina reinforced composites. A new wear-resistant reinforcement opportunity for composites has emerged and composite costs have been reduced. It is important that industrial wastes have improved the wear resistance of composite materials. Using slag reinforcement in epoxy matrix provide advantageous both in terms of eliminating these wastes which are harmful to the environment and in terms of preserving natural reinforcement sources using in the composite materials productions. For practical use mention by their results, that the polyamide composites are suitable as machine elements in normal abrasive applications, as they resist again abrasion wear. However, if there are any extreme demands, for example: high mechanical properties, temperature resistance and excellent chemical resistance etc., we can use PEEK composites also, but it is important to know the character of the filling. It is clear that the glass fibre (GF) has a bad effect on the friction and the wear at abrasive surface.

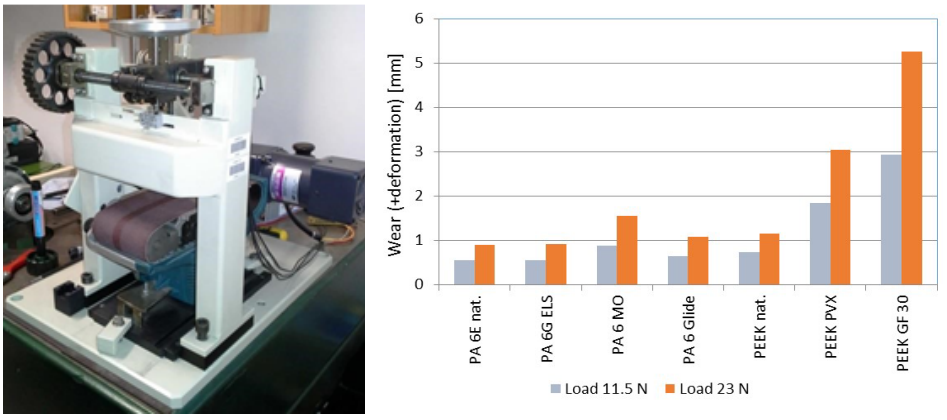

Figure 3. Abrasion testing equipment and the wear values for different materials in 11.5 N and 23 N load categories

The small-scale abrasion tests with PA and PEEK polymers and composites with abrasive surface provided new information about their tribological behaviours. These results extend our tribological knowledge about polymers and show new possibilities for practical application. (Zsidai et al., 2016)

Conslusion

The polyamides show a better wear result among tested polymers in both investigations, according to the low elasticity modulus of this polymer. The

flexibility of the polymer chains is enhanced for soft materials (reflected by a low elasticity modulus), a better more effective transfer can occur.

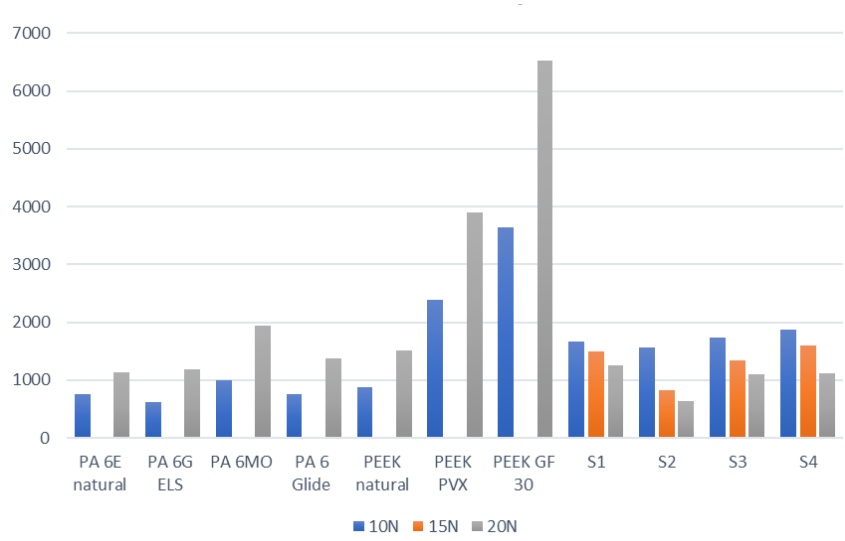

Fiure 4. Addition fillings and wear effects on the composites in different loads

Mostly, the slag fillers showed higher wear resistance than the Al_2O_3 reinforced composites. Among the slag fillers, the blast furnace exhibited superior tribological performance. While Al_2O_3 and blast furnace slag reinforced composites showed plastic deformation due to fatigue, transverse cracks and displaced reinforcement particles were observed in ferrochromium slag and converter slag reinforced composites. Increasing the applied load caused acceleration in wear rate. Thermal conductivity was increased by particle addition, which contributed to the improvement of the wear performance. This study once provided that industrial wastes can be used as reinforcement material in composites and thus a cleaner environment can be obtained. In the second hand the addition fillings have a different effect on the composites. While these fillings have a good effect for the friction coefficients of polyamides, in case of PEEK they have an unfavourable effect at both load categories. The former are true for the abrasion wear also where the PEEK composites suffer an essential higher abrasion in comparison with polyamide composites. Based on the results of experiments, the following conclusions can help and improve the further tribotesting of polymers, the selection of proper material and design. The abrasion investigations show that short carbon fibres proved better for improving wear resistance as compared to short glass fibres, in the given circumstances.

References

Zsidai L., Kátai L., 2016. Abrasive Wear and Abrasion Testing of PA 6 and PEEK Composites in Small-Scale Model System

Baptista, R., Menda~o, A., Rodrigues, F., Figueiredo-Pina, C.G., Guedes, M., MaratMendes, R., 2016. Effect of high graphite filler contents on the mechanical and tribological failure behavior of epoxy matrix composites. Theor. Appl. Fract. Mech. 85, 113e124.

Samyn, P., Zsidai, L., 2017. Temperature effects on friction and wear of thermoset polyester fabric composites. Polym. Plast. Technol. Eng. 56 (9), 1003e1016.

Sarkar, P., Modak, N., Sahoo, P., 2017. Effect of normal load and velocity on continuous sliding friction and wear behavior of woven glass fiber reinforced epoxy composite. Mater. Today: Proc. 4, 3082e3092.

Megahed, A.A., Agwa, M.A., Megahed, M., 2018.Improvement of hardness and wear resistance of glass fiber-reinforced epoxy composites by the incorporation of silica/carbon hybrid nanofillers. Polym. Plast. Technol. Eng. 57 (4), 251e259.

Bazrgari, D., Moztarzadeh, F., Sabbagh-Alvani, A.A., Rasoulianboroujeni, M., Tahriri, M., Tayebi, L., 2018. Mechanical properties and tribological performance of epoxy/Al_2O_3 nanocomposite. Ceram. Int. 44 (1), 1220e1224.

Rajasekar, A., Arunachalam, K., Kottaisamy, M., 2019. Assessment of strength and durability characteristics of copper slag incorporated ultra-high strength concrete. J. Clean. Prod. 208, 402e414.

Cao, L., Shen, W., Huang, J., Yang, Y., Zhang, D., Huang, X., Lv, Z., Ji, X., 2019. Process to utilize crushed steel slag in cement industry directly: multiphased clinker sintering technology. J. Clean. Prod. 217, 520e529.

Effect of sliding velocity and loads on friction coefficient and temperature in DLC and PA 6 contact in dry sliding conditions

Ádám SARANKÓ, Gábor KALÁCSKA, Róbert KERESZTES
Institute for Mechanical Engineering Technology,
Szent István University, Gödöllő, Hungary

Abstract

This study presents tribological tests of DLC (Diamond Like Carbon) against PA 6 (polyamide 6). Two kinds of measurement groups were done to get information about in a continuously sliding frictional contact without any lubrication. The effect of loads and the sliding velocities were investigated separately in this research. Three levels of loads and four different sliding velocity values were set. Static weight load was supplemented with continuously alternating vibration load for one of each pair of measurements. Coefficient of friction and temperature values were measured. After evaluating the results we got information about which parameter influences the results more.

Keywords

DLC, dry sliding friction, polyamide, temperature measurement

1. Introduction

Friction is a complex phenomenon in the nature. It occurs nearly everywhere in our lives even if we do not pay attention to it. This phenomenon also can be advantageous or undesired.

Friction is always accompanied by wear. In engineering usually wear is a drawback. In machining, in case of cutting tools, or tool inserts the friction, wear and the life of the tool is a crucial factor. With proper tool materials, the life of tool can be improving. However, there are some hard or special workpiece material which makes the tool unusable relatively fast. That is way the scientists and industrialists develop coatings and coating technologies (Tyagi et al., 2019). DLC is one of the most popular high-performance coating material which produced to improve the frictional properties of sliding contacts (Li et al., 2017)beside abrasive wear resistance [Bártfai et.al. 2011]. DLC coating is used widely because of its great properties, such as high hardness, low friction and excellent chemical stability (Lu et al., 2019). DLC has very similar properties to polycrystalline diamonds, which is a high-performance tool material (Erdemir, Martin, 2018). DLC coated tools shows smaller adhesion in the cutting edge (Yokota et al., 2013).

We can not find any data in the literature about DLC coated materials sliding against polymer surfaces in dry sliding contact. In this article, we studied the effect of different parameters using DLC coated steel against PA 6.

2. Method

Pin-on-disc tribological test method is frequently used because it is suitable for compare materials or the effect of different parameters in a continuously sliding system. Special shaped specimens were used as pins. Specimens were DLC coated AISI52100 ball bearing steel. The DLC coatings were produced by Oerlikon Balzers in Hungary. The height of the specimen was 5,3 mm; the contact surface was nearly a flat surface with diameter 21,5 mm, which is 363,05 mm^2. The surface roughness of the DLC coating was Ra 0,04.

Special holder for the specimen (Fig. 1.) was made in our workshop in Szent István University. The material of the holder was Polyvinyl Chloride (PVC). PVC is a common and cheap polymer material. Usually, polymers have good thermal insulation ability, so the holder was suitable for measuring temperature during the tests. The holder is compatible with our pin-on-disc type tribological test device.

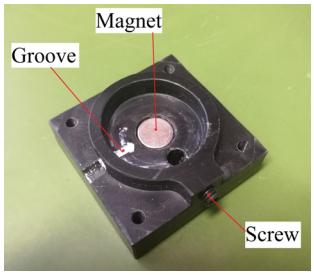

Figure 1. Specimen holder

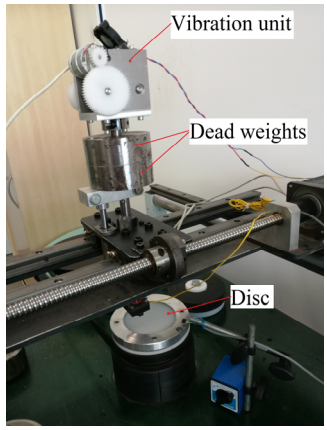

Figure 2. Pin-on-disc type tribological test device

There is a magnet in the bottom of the holder to keep the specimen on the place when fixing the holder to the testing device. After the holder was fixed to the device, we must adjust the screw to prevent any movement of the specimen during the measurements. We can also see a groove at the bottom of the holder. In this groove the temperature sensor takes place. We cannot measure the temperature directly in the contact zone. The temperature was measured on the opposite side from the contact zone of the specimen. Thermal conductive paste

was used for more precise results. This method is suitable to compare the different effects of parameters.

The material of the disc was Polyamide 6 (PA 6). It was 100 mm in diameter with 12 mm thickness. In this setup, the disc was the softer material. After every test, the sliding surface was damaged. To get better results, the damaged surface was removed after every test, using a conventional lathe machine. Therefore, the surface roughness of the disc was always different. In sliding systems, it is a significant factor. Surface roughness values were measured on a Mitutoyo SJ-201 device. Table 1. shows the average surface roughness (R_a) values for each test regarding the disc.

In Table 1. loads were calculated from the surface of the contact area and the perpendicular force which provided by dead weights (Fig. 2.). 20 N, 40 N, and 60 N forces were used for the first test group. In case of second group, 40 N force was used for each test, as a static weight. The vibration unit on Fig. 2. provided an additional continuously alternating load to the contact zone. 0 Hz frequency means the unit is switched off. When this unit switched on, it provides 28 Hz vibration load which means additional ±14,5 N alternating force. The load from this vibration also can be calculated using the contact surface of the specimen and the disc. This was ±0,04 MPa.

Table 1. Average surface roughness values of the disc

Loads	**1. Test group**		Sliding velocities	**2. Test group**	
	0 Hz	**28 Hz**		**0 Hz**	**28 Hz**
0,055 Mpa	0,75	0,76	**0,1 m/s**	0,95	0,8
0,11 Mpa	1,03	1,24	**0,2 m/s**	0,95	0,93
0,165 Mpa	0,92	0,83	**0,4 m/s**	0,88	0,87
			0,6 m/s	0,9	0,9

In the first test group three load levels were used with the above-mentioned vibration loads. The sliding velocity was 0,5 m/s in this group. In case of second group the static load was 0,11 MPa also with or without vibration. The diameter of the sliding path was 60 mm in all cases, and the 300 m sliding distance also was the same of all test to compare the effect of different loads and sliding velocities to coefficient of friction and temperature.

After every measurement the used surface of the disc was re-machined and cleaned with methylated spirit. Tests were done in dry sliding condition without any lubrication. Before commencing the test, we initialized parameters on the computer. The strain gauges found on the force measuring sensor and the type Spider 8 measuring amplifier are connected by wire converting the analog signals to digital, which are then transmitted to the computer. The chart-like

visualization of the digital signals was achieved with software called Catman. The measuring frequency was 5 Hz in all cases. During the tests, all data and the prepared diagrams were monitored and displayed on the screen in real time. After completing the test, all data were saved in the appropriate file for later processing, using a spreadsheet.

3. Results

During the entire tests, the computer registered the friction forces, the rotation speed of the disc, and the temperature of the specimens from the opposite side in the function of sliding distance. Diagrams were made in Microsoft Excel to illustrate the results. Each diagram contains two test results. One without vibration, the other with the same parameters without vibration. The constant parameters were mentioned before. The title of the diagrams shows the parameter what changed.

Fig. 3. shows the results of the first test pair of the first measurement group. Between coefficient of friction (Cof.) values there are not significant differences in the first 100 m. After this point Cof. values are lower, temperature values are also lower from the beginning of the test with the supplemented vibration load.

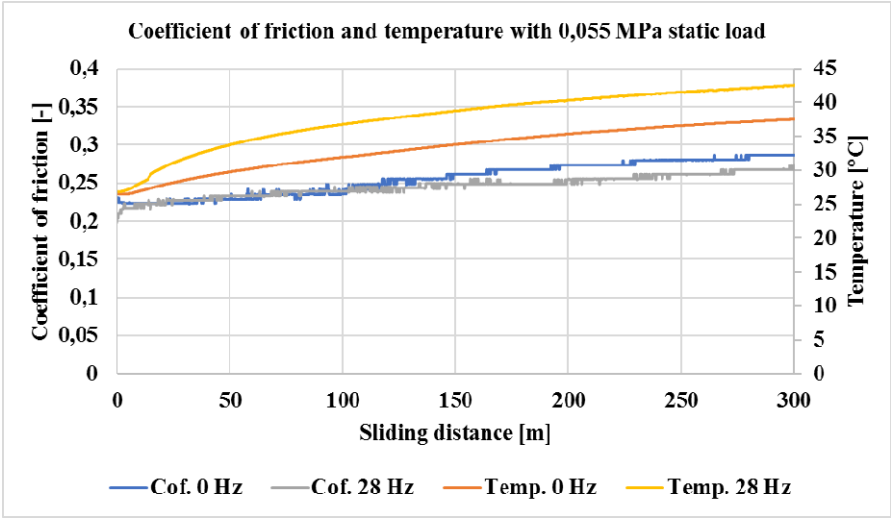

Figure 3. Results of first measurement group I.

In Fig. 4. the results of the second test pair can be seen. There are not significant differences between the temperature values. The Cof. curves are parallel to each other but reach higher values with vibration. Cof. values are lower, temperature values are higher compare to the previous results.

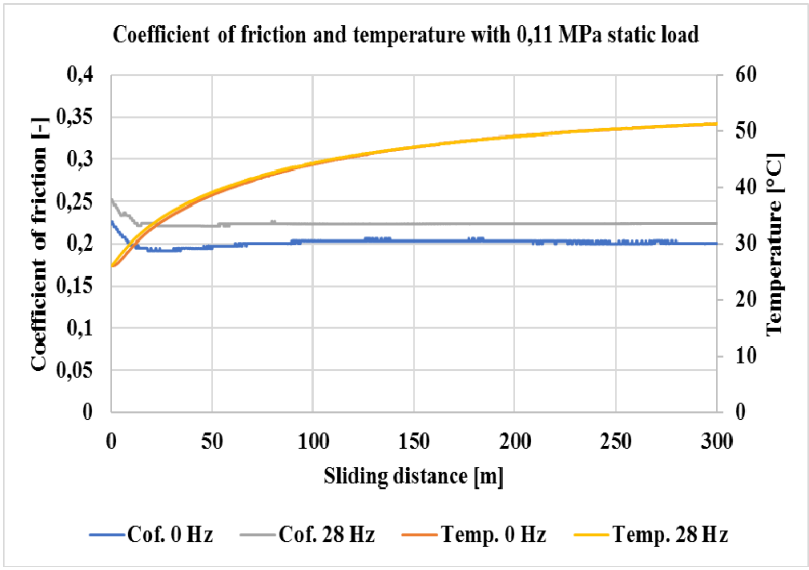

Figure 4. Results of first measurement group II.

In Fig. 5. we can see the last test pair of the first group. In the first 200 m the Cof. curves are parallel to each other. After this point the vibration load effected Cof. values negatively. The temperature values are also the same in the first 50 m. Vibration also has a negative effect to the temperature with these parameters. Temperature values were significantly higher compared to the previous two cases.

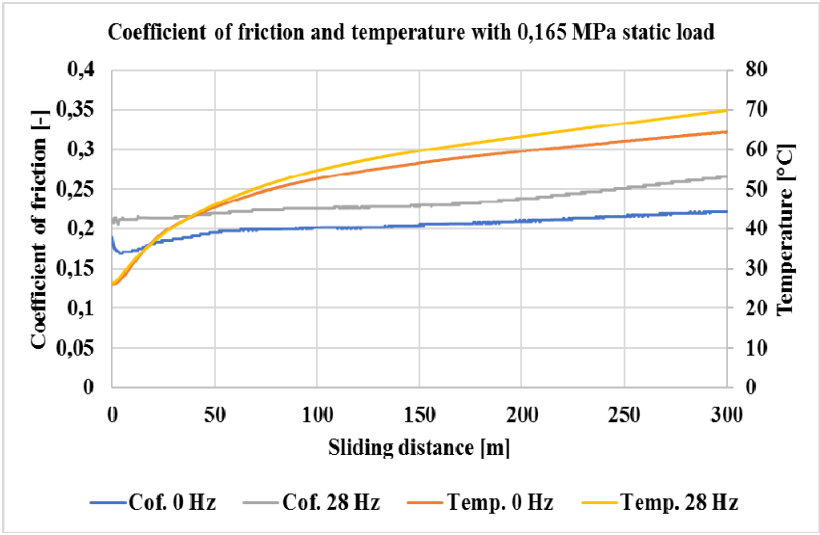

Figure 5. Results of first measurement group III.

In Fig. 6. we can see the results of the first measurements of the second group. The Cof. curves are rough. This is because 0,1 m/s is a relatively low sliding velocity. At low sliding velocities a common phenomenon, so called frictional instability, is appear frequently. The frictional instability effects the Cof. negatively. Cof. values are very high due to this phenomenon. Temperature values are nearly the same. Compared these temperature results to the results of the second tests of first group (same parameters except the sliding velocity) we can say that sliding velocity is an important factor in sliding contacts. Cof. values are higher with vibration.

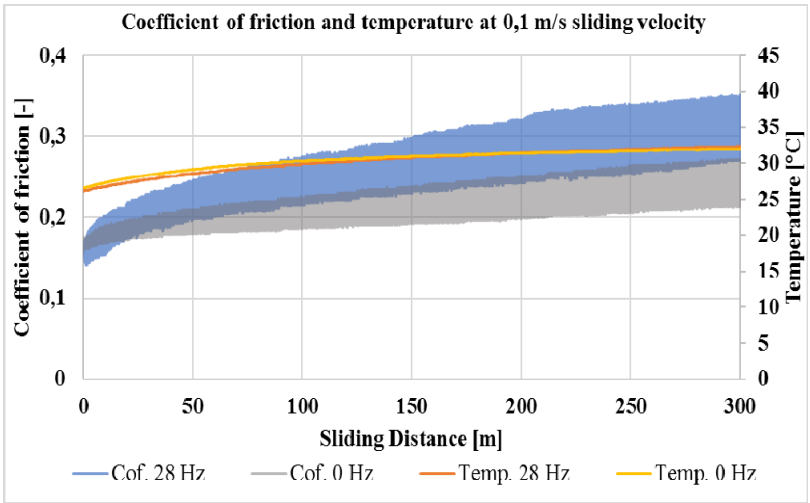

Figure 6. Results of second measurement group I.

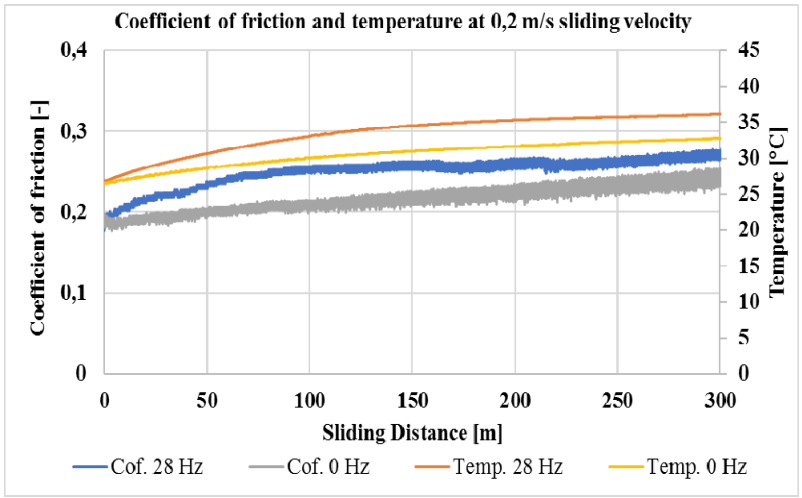

Figure 7. Results of second measurement group II.

In Fig. 7. 0,2 m/s sliding velocity was used. This value is also relatively slow. Sliding instability appears in this case too. However, the effect of this phenomenon is much lower, the Cof. curves are smoother. Both temperature and Cof. are higher with the supplemented vibration load.

Fig. 8. shows the results of the third tests of the second measure group. The Cof. curves are not rough in this case. The phenomenon of frictional instability is disappeared with the used sliding velocity. There are not significant differences between the measured temperature values. Cof. values are higher in the first 250 m with vibration. However, after this stage the vibration effect positively to the Cof.

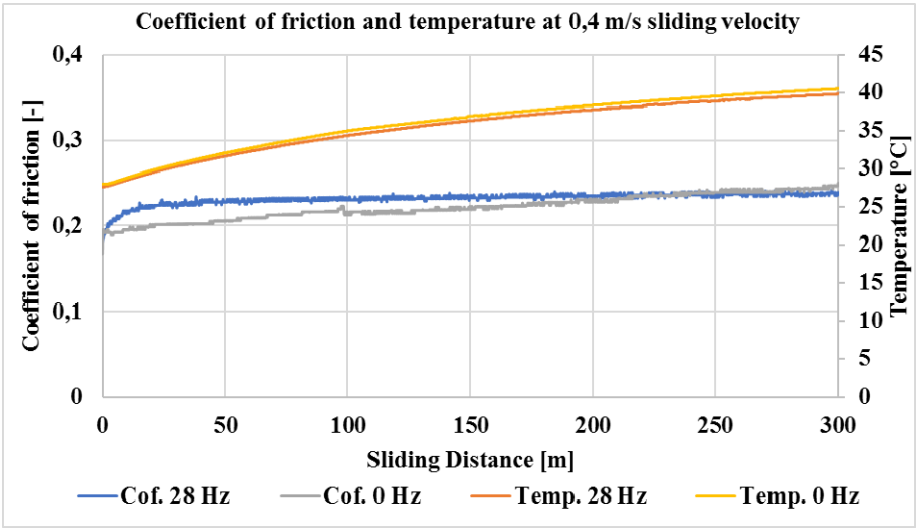

Figure 8. Results of second measurement group III.

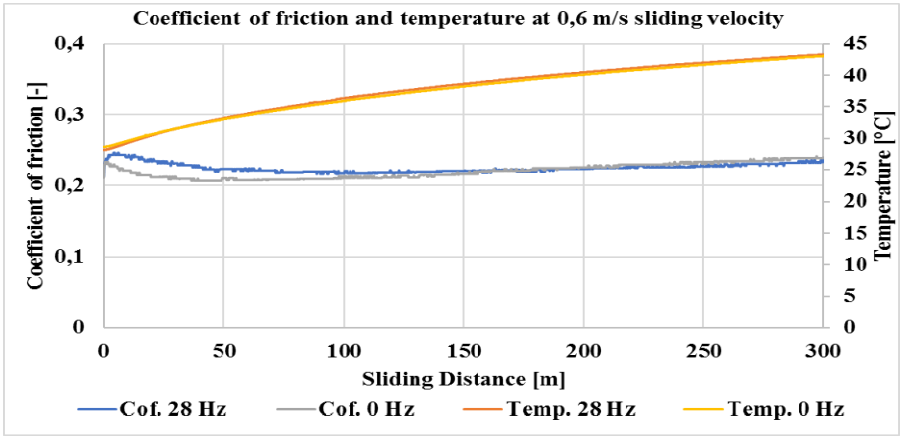

Figure 9. Results of second measurement group IV.

Fig. 9. shows the last tests of the second group. The temperature values are nearly the same. After the first 200 m Cof. values are lower with vibration. Using 0,6 m/s the Cof. values are the lowest.

Conclusions

After evaluating the results, we concluded that within the investigated range increasing the load, effected the temperature and the coefficient of friction negatively. While increasing the load, the temperature significantly increased. While changing the sliding velocity there were not significant differences between the temperature values. In case of vibration load the coefficient of friction was higher at the beginning of the measurements. However, in case of the two last tests of the second measurement group, after a while the coefficient of friction curves crossed each other in the diagrams where the test pairs were shown (same parameters, with and without vibration), and then the coefficient of friction values were lower with vibration.

Both the load and the sliding velocity are important factors in a continuously sliding dry contact. At low sliding velocities the phenomenon of sliding instability occurs and have significant, negative effect to the coefficient of friction. Increasing the load have more effect on temperature.

Acknowledgements

This article was supported by the ÚNKP-19-3-I New National Excellence Program of the Ministry for Innovation and Technology.

References

A. Erdemir, J.M. Martin, (2018). Superior wear resistance of diamond and DLC coatings. Current Opinion in Solid State & Materials Science, vol. 22, pp. 243-244.

A. Tyagi, R.S. Walia, Q. Murtaza, S. M. Pandey, P. K. Tyagi, B. Bajaj (2018), A critical review of diamond like carbon coating for wear resistance applications, Refractory Metals & Hard Materials, pp. 1-7.

Bártfai, Zoltán ; Blahunka, Zoltán ; Lefánti, Rajmund ; Nagy, Béla ; Szalkai, István: Abrasion test of different cultivator shares pp. 110-110. Paper: 41 .Synergy 2011.

T. Yokota, T. Sawa, M. Yokouchi, K. Tozawa, M. Anzai, T. Aizawa (2013), Frictional properties of diamond-like carbon coated tool in dry intermittent machining of aluminum alloy 5052, Precision Engineering, vol. 38, pp. 365-366.

Y. Lu, G. Huang, L. Xi, (2019). Tribological and mechanical properties of the multi-layer DLC film on the soft copper substrate, Diamond & Related Materials, vol. 94, p. 21.

Z. Li, X. Guan, Y. Wang, J. Li, X. Cheng, X. Lu, L. Wang, Q. Xue, (2017). Comparative study on the load carrying capacities of DLC, GLC and CrN coatings under sliding-friction condition in different environments. Surface & Coatings Technology, vol. 321, pp. 350-351.

Metal foam specimen production problems focusing mechanical tests

András GÁBORA[1], Tamás MANKOVITS[1], Gábor KALÁCSKA[2]
[1]Department of Mechanical Engineering, University of Debrecen
[2] Institue for Mechanical Engineering Technology, Szent István University

Abstract

Metal foams have a lightweight cellular structure with excellent mechanical and physical properties, which are favourable in many industrial and agricultural applications [Bártfai et. al 2018]. Although metal foams are popular, they are still not sufficiently characterized thanks to their extremely complex structure which is highly stochastic in nature. In laboratorial circumstances the production of closed-cell aluminium foams depends on several factors. In our present paper we are introducing and investigating the technological solution to create test specimens from closed-cell aluminium foams. The purpose is to define the applicable production technologies and the geometry of the specimens for general destructive mechanical tests.

Keywords

closed-cell metal foam, specimen production, mechanical test, tribological properties

1. Introduction

There are different types of metal foam structures, open and closed-cell metal foams, metal matrix syntactic foams and from different raw materials. ALUHAB is a new type of aluminium foam [Babcsán *et al*. 2014] with controlled, homogeneous cell sizes. This foams are manufactured from aluminium alloy containing ultrafine particles (below 3 μm). The unique loud-nozzle technology permits the injection of bubbles with optimal size which can vary between 0.5 mm and 5 mm. CT imaging, [Babcsán *et al*. 2014] different analytical techniques and mechanical tests were used to characterize the influence of the alloy composition and the cell structure on the compression properties. A micro-computed tomography (micro-CT) equipment is capable to image the three dimensional structure of these foams such as ALUHAB with a resolution in the range of 5-50 μm. The CT parameters for the optimal image quality were determined by varying the size of the sample, the applied projection number and also the X-ray source operating parameters. Rheological behaviour of liquid ALUHAB aluminium foams was investigated [Szamel *et al*. 2014]. Metal matrix

syntactic foams (MMSFs) can be produced by stir casting or pressure infiltration [Orbulov, Dobránszky 2008]. The metal matrix can be aluminium or magnesium and the hollow spheres material is usually some sort of ceramic (SiO_2 and/or Al_2O_3) or metallic (pure iron or steel). The effect of the infiltration parameters on the microstructure and mechanical properties of MMSFs were investigated by microscopy and compression test. Later [Orbulov, Ginsztler 2012] the compressive behaviour of MMSFs were investigated and presented. The engineering factors (chemical and physical) have significant effects on the compressive properties. The F3S.20S (AA 359/SiC/20p) aluminium based metal matrix composite (Duralcan) can be foamed directly by adding titanium hydride (TiH_2) to the MMC melt. This kind of experiments starts at our Department years ago [Gábora *at al* 2008]. The cellular structure of our foam is not enough homogeneous. We made the structural analysis and its statistical evaluation [Mankovits *et al* 2014] and computed tomography as well [Varga *et al* 2016]. The wear properties [Májlinger 2015] and tribological behavior of hybrid AMSFs were investigated by pin-on-disc method with low carbon steel disc [Májlinger *et al* 2016]. The test in lubricated condition showed significantly different properties than the dry test. The coefficient of friction, height loss of the specimens and specific wear showed good relation with mechanical parameters [Májlinger *et al* 2017].

For the future we are planning to evaluate a general mechanical test on closed-cells metal foams made by different processes. Characterization of cellular materials need particular attention on test specimens manufacturing process. Unprecise specimens result inadequate outcome. The aim is to define the standardized shape and dimensions of specimens and there manufacturing possibilities.

2. Materials and methods

The investigational metal foams are produced by different process-routes. The ALUHAB type (AFBFs and AFBFb) is made by bubble injection process, the other one was produced from Duralcan F3S.20S Metal Matrix Composite using direct foaming technique by adding blowing agent (AFDF). The produced closed-cell aluminium foams can be seen on Figure 1. The average cell size of the metal foams were measured and evaluated by statistical methods. The average cell size for AFBFs type is 1,5 mm, for AFBFb type is 4,5 mm and for AFDF 2,5 mm. The planned destructive tests are the following: uniaxial compression test, fatigue test for compression, Izod impact test and pin-on-disc dynamic tribological material investigation. All the test are regulated by standards.

For the compression test and for the fatigue test an INSTRON 8801 fatigue testing machine will be used at the University of Debrecen, while the pin-on-disc investigation will be handled by the machine developed at the Szent István University, see in Figure 2. The Izod impact test will be investigated as a service.

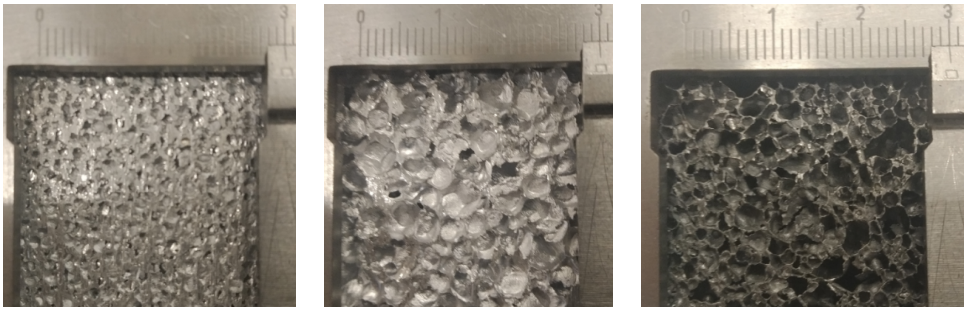

AFBFs AFBFb AFDF

Figure 1. Closed-cell aluminium foams

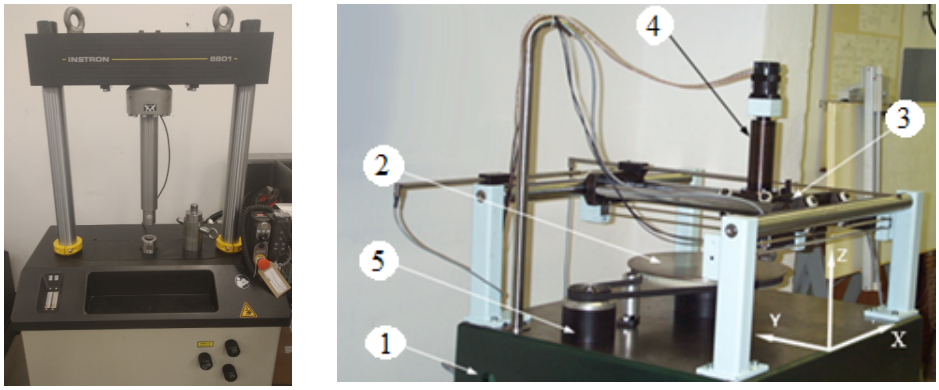

INSTRON 8801 fatigue testing machine

Pin-on-disc dynamic tribological material investigation system

Figure 2. Instrumental background

Figure 2 shows the main units of the pin-on-disc dynamic tribological material investigation test system: (1) table, (2) disc, (3) positioning system, (4) loading system, (5) electric motor with speed setting rotating the disc.

Table 1. Specimen information

	Uniaxial compression test	Fatigue test	Izod impact test	Pin-on-disc test
Specimen shape	cylindrical	cylindrical	prism (notched)	cylindrical
Size	d=30 mm h=30 mm	d=30 mm h=30 mm	a*a=10x10 mm^2 h=75mm	d=15 mm h=15 mm

For the uniaxial compression test and for the fatigue test the ISO 13314:2011 (Mechanical testing of metals – Ductility testing – Compression test for porous

and cellular metals) standard, for the Izod impact test the ISO 180:2000 (Determination of Izod impact strength), for the pin-on-disc dynamic tribological material investigation the ASTM G99 - 05 (Standard Test Method for Wear Testing with a Pin-on-Disc Apparatus) are applied. According to the standards Table 1 collects the most important information about the specimen geometry.

While cylindrical and prism type specimens will be used different manufacturing technologies are necessary to apply. For cylindrical specimens the abrasive water jet machining and the turning technology can be used. For prism specimens the milling and the cutting can be the advantageous technologies.

3. Results and discussion

Abrasive water jet machining is a machining technique used in many industrial applications. It is a non-conventional machining process where material is removed by impact erosion of high pressure, high velocity of water and entrained high velocity of grit abrasives on a work piece [Relekar *et al* 2015]. The machine for abrasive water jet machining can be seen in Figure 3. Turning, milling and cutting are traditional technologies which are not detailed here.

Figure 3. The TECHNI i510-G2 abrasive water jet cutting machine and the specimen (AFBFs)

The cutted specimen (AFBFs) was measured and conicity was observed. The value of the conicity is 3% which can have effect on mechanical properties.
The matrix material of the AFDF is Duralcan F3S.20S Metal Matrix Composite which contains SiC particle which makes the material resistant against machining. A turning experiment was done using two type of cutting tools for turning technology. One cutting tool was made from High Speed Steel (HSS), the other was made from carbide insert.

From Figure 4 it can be seen that the cutting tools were abraded even at low depth of cut. This phenomena complicates the production much more.

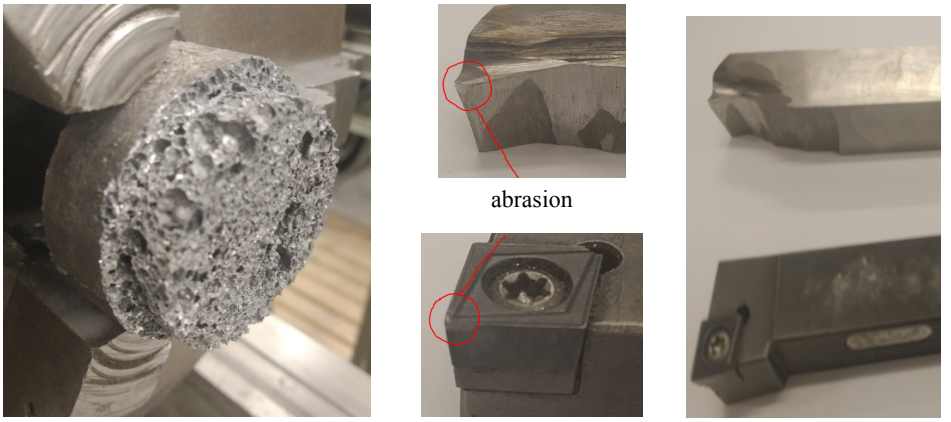

Figure 4. Turning of AFDF and the abraded cutting tools

During milling it is critical when bigger cell sized aluminium foams are manufactured because of smearing. From Figure 5 it can be seen that the aluminium foam was smeared even at high speed and small depth of cut.

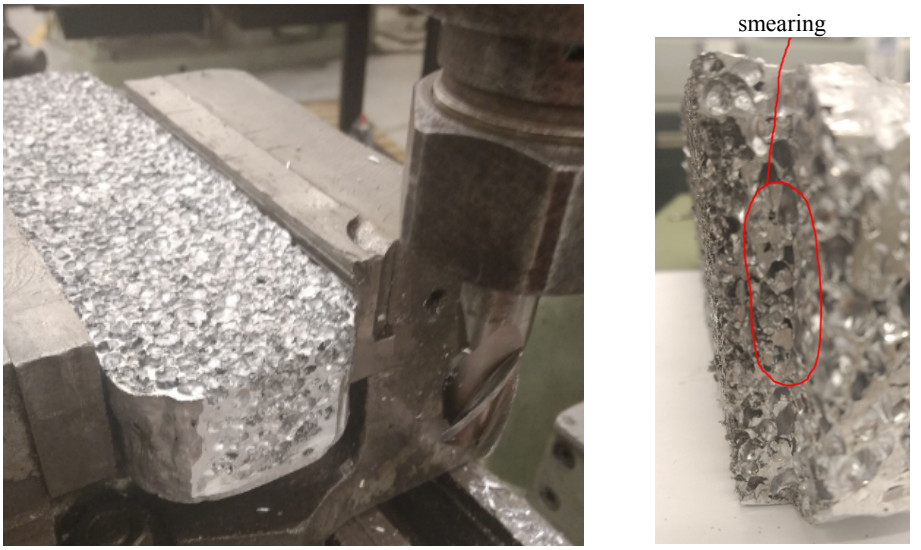

Figure 5. Milling of AFBFb and the smeared surface of the aluminium foam

Using Struers cutting machine cubic specimens were cut [Mankovits *et al* 2014]. The parallelism cannot be exactly encouraged so this type of machining is not the best solution to produce prismatic specimen.

Four type of manufacturing technologies were investigated on the critical aluminium foams and it can be seen that specimen production raises many unanswered questions. To be able to produce numerous and sufficiently accurate specimens further investigations are needed on technological point of view.

Conclusions

The paper dealt with the manufacturability of different type of aluminium foams to produce specimen for later destructive tests. For different type of material tests the governing standards were studied and the specimen sizes were determined according to the average cell sizes. Abrasive water jet machining, turning, milling and cutting were done to observe the utility of the different technologies. Further research (cutting force determination, parameter settings) is needed for developing the manufacturing technologies aiming to produce accurate specimens for characterizing the investigated aluminium foams.

Acknowledgement

The authors would like to thank for the manufacturing work to Zoltán Géresi.

References

Babcsan N., Beke S., Makk P., Szamel Gy., Kadar Cs.(2014): Pilot production and properties of ALUHAB aluminium foams, Procedia Materials Science 4, pp. 127-132.

Babcsan N., Beke S., Szamel Gy., Borzsonyi T., Szabo B., Mokso R., Kadar Cs., Kiss B. J.: Characterisations of ALUHAB aluminium foams with micro-CT, Procedia Materials Science 4, pp. 67-72.

Bartfai, Z. ; Blahunka, Z. ; Toth, L. ; Hartdegen, G.: Improving the Wearing Properties on Biogas Plantshredding MaChine. Hungarian Agricultural Engineering : 34 pp. 30-34. , 5 p. (2018)

Szamel Gy., Beke S., Babcsan N.(2014): Rheological behaviour of liquid ALUHAB aluminium foams, Procedia Materials Science 4, pp. 67-72.

Orbulov I. N., Dobranszky J.(2008): Producing metal matrix syntactic foams by pressure infiltration, Mechanical Engineering 52/1, pp. 35-42.

Orbulov I. N., Ginsztler J.(2012):Compressive characteristics of metal matrix syntactic foams, Composites: Part A 43, pp. 553-561.

Orbulov I. (2013): Metal matrix syntactic foams produced by pressure infiltration-The effect of infiltration parameters, Materials Science & Engineering A 583, pp. 11-19.

Gabora A., Toth L., Babcsan N.(2008): Mechanical Tests and Process Optimization of Aluminium Foams Made by the Melt Route. JUNIOR EUROMAT Conference.

Mankovits T., Budai I., Balogh G., Gabora A., Kozma I., Varga T.A., Mano S., Kocsis I.(2014): Structural analysis and its statistical evaluation of a closed-cell metal foam. International Review of Applied Sciences and Engineering, vol. 5, no. 2, pp. 135-143.

Varga T.A., Budai I., Gabora A., Kozma I., Mano S., Mankovits T.(2016): Structural Analysis of Metal Foams with Computed Tomography. Proceedings of the XXI-th. International Scientific Conference of Young Engineers, pp. 437-440.

Májlinger K.(2015): Wear properties of hybrid AlSi12 matrix syntactic foams. International Journal of Materials Research 106/ 11, pp. 1165-1173.

Májlinger K., Bozóki B., Kalácska G., Keresztes R., Zsidai L., (2016): Tribological properties of hybrid aluminum matrix syntactic foams. Tribology International 99, pp. 211-223.

Májlinger K., Kalácska G., Orbulov I. N., Zsidai L., Bozóki B., Keresztes R., (2016): .Global Approach of Tribomechanical Development of Hybrid Aluminum Matrix Syntactic Foams. Tribology Letters 65:1699.

Relekar K. M., Kalase A. B., Dubal S. P. (2015): Abrasive water jet machining, International Journal of Innovations in Engineering Research and Technology 2/10.

About the unconventional marine currents energy systems

Adriana COTEŢIU, Radu COTEŢIU,
Marius ALEXANDRESCU
Faculty of Engineering, Technical University of Cluj-Napoca

Abstract

This paper presents the preoccupations regarding consequences of the aggression of the transmission and pollutant agents on the environment and mundane atmosphere. These are externalized though the emergence of the global heating effect, that has major impact on mundane climate. A solution for decreasing the global heating effect is given by the unconventional energetic systems, which are efficient and influences the climate in better. They are many sources of regenerative energies. The no conventional converting marine currents energy systems are one of the most important of them. This paper presents some solutions of no conventional converting marine currents energy systems and also there tendency in the future.

Keywords

global heating effect, regenerative energies, turbine marine current.

1. Introduction

Coal and gas fuel, petroleum oil fuel represents the most used combustible of the world economy. Their exploitation constitutes a transformation and a destruction of those resources with catastrophic effects on the human bean and on the environment.

The new economy based on the inexhaustible energy of sun, wind, water, current marine, waves and biomass and it must be an ecological economy.

The second principle of the thermodynamics specifies that each transformation is accompanied by losses. So, if any raw material or energy that contains noxious substances, then the transformation process losses they are pollutants emission with majors implications on the mundane climate.

A solution way of the decreases global heating effect phenomena concerns in the revolution of the energy technology, using the regenerative or alternative energy. Theses will replace the mixture of the conventional resources witch are limited and pollutant.

In 2004 year the production of the electric energy was 17400TWh. Part of this production, 39%, was given by the heat energy, obtained on the coal burns, 20% obtained on the gas burns, 16% due of the nuclear energy and the difference was given by oil, wind, biomass and hydraulic energy.

It is known the fact that the gas, coal and petroleum burns increase the changes climate phenomena. Thus is very important that until 2020 year the global quantity of regenerative energy increase till 80%. [1], [2]

2. Energy regenerative sources. No conventional converting marine currents energy systems

Today the "fossil world economy" became an exhaustion under way model. The regenerative energy and the recovered charge are the alternative solutions like the pollutant fossil resources.

The regenerative energies involve sunlight energy, thermal sun energy, hydraulic energy, wind energy, current marine energy, wave's power, tide power and biomass.

The marine currents made by the ocean waves or by the difference of temperatures between tropical and polar water (Golf stream, Labrador stream etc) represents a considerable source of no pollutant alternative energy. The waves made by the wind can cover a long distance without meaningful losses. The kinetic energy produced by these currents is focused near the water surface and is very strong. So, is not necessary a very great number of hours and days to function comparative with solar and wind systems energy.

West part of Europe offer many places with a great marine current potential like: England, France, Portugal, Spain, Norway, Italy, Netherlander and many others. The world potential for this source of energy was estimated by 64000MW. It is remarkable that the marine current turbines works at the same price like wind turbine located in the ocean aria (5 eurocent /kWh). [2], [4]

The advantages of converting marine current turbines comparison with the wind turbine are:

- these can predict in ratio 100% the appearance of the marine currents;
- at the same power like that given by the wind turbine (0,75-1,5 MW), the rotor diameter is smaller (15-20m comparative with 60-80m);
- it is not necessary the control of the impeller blade pitch;

The disadvantages are:

- like an energy source it can work just 10 hours by day;
- efficiency increases with depth (more than 60m);
- corrosion problems;
- a great attention concerning their maintenance.

World's marine energy reserves are considerable. In addition to its role in the reduction of energy consumption levels, the development and application of such marine resources as ocean temperature differences, waves, currents, and tides is also in accordance with the increasingly prominent emphasis on environmental protection. Research on the development of marine power applications would lay the foundation for oceanographic technology as well as the integrative development of oceanographic resources on a international scale. The following is an update of current research on the various applications of marine power generation:

Ocean Temperature Difference Power

The working principles behind power generation based on ocean temperature differences are similar to those behind current applications for thermoelectricity and nuclear power. The vaporization of surface seawater working fluids (i.e. ammonia, propane, freon) with low evaporation temperatures is used to run turbine generators; the subsequent application of cold deep-level seawater coolant is then used to liquefy the working fluid vapors, enabling the entire process to be repeated. The precipitous bathymetry of the coasts of many countries allows areas not far from the coastline to reach water depths of as much as 800m and temperatures of around 5^{o}C, while water temperatures at the surface (through which the current happens to flow) remain as high as 25^{o}C. Such ideal topographic and temperature conditions hold enormous potential for the development of temperature difference power generation.

According to the results of a series of completed studies, the most formidable technological challenges facing the construction of a temperature difference power plant include large coldwater pipe design, manufacturing, and installation, large-scale coastal platform design and construction, and high performance sub bottom electric power transfer cables, none of which have been successfully developed. Even accounting for the economic value of aquatic breeding by-products, the cost of temperature difference power generation is still significantly greater than that of such traditional power supplies as coal, fuel, and nuclear energy.

Wave Power

Wave power generation converts the kinetic energy of waves into electricity. With an operating system designed to effectively absorb the vertical vibration of waves, a wave power generator is a fixed mechanism used to collect and convert the kinetic energy of waves into electricity. With offshore regions subject to strong monsoon winds and surrounding oceans abounding with turbulent breakers, the many regions rich supply of wave energy would provide a considerable source of marine power.

Determining the most effective application of wave energy for power generation is currently the main objective of marine engineering researchers. Though wave power generation neither produces pollutants nor consumes fuel, the instability of wave action and the installment of fixed generating equipment in the seabed induce such problems as seawater corrosion, tidal intrusion and destruction, inadequate efficiency, and excessively high construction and maintenance costs. The resulting limitations of technological developments in the field have significantly retarded the further advancement of wave power generation systems research.

Tidal Power

Gravitational effects on seawater produce variations in water level elevation known as tides. Tidal power generation makes use of this natural phenomenon to produce electrical energy via conversion. Frequently constructed around bays or estuaries, reservoirs are equipped with a controllable floodgate placed in a suitable location within the enclosing embankment to provide a conduit for seawater circulation. Installed on this floodgate is a water turbine generator

propelled by the inflow and outflow of seawater into and out of the reservoir during tidal flow and ebb. Marine power generators based on bi-directional flow currently make up the principal application system of tidal power generation.

With the existing technological development of low and high quality tidal range turbines, a tidal range of only 1 meter and topography open to the construction of surrounding tidal pools are the only prerequisites for development.

Ocean Current Power

Ocean current power generation involves the use of a water turbine generator to convert the power of ocean current flow into electricity. Most systems require what is known as a stop-flow culvert caisson containing a water turbine generator, to be installed in the path of ocean current flow. Numerous such packages are necessary to generate power though they must be positioned at appropriate intervals in order to prevent turbulent flow interference.

Because marine current power generation is low-energy, low-density, and based on a unique environmental phenomenon, the general scope and economic incentives of its future development remain a topic for further evaluation and discussion.

3. Technology

Marine current energy is in the early stage of development, with only a small number of prototypes and demonstration units having been tested to date. There are no commercial grid-connected turbines currently operating.

The most common types of tidal current capture devices are variants of horizontal axis or vertical axis turbine. There are a variety of marine current energy capture devices that are also being investigated, however this project will only consider the following three types of technology in there generic form:

- Horizontal axis turbine (axial flow turbine fig.1);
- Vertical axis turbines (cross flow turbine fig.2);
- Oscillating Hydrofoil (fig.3).

Horizontal axis turbine

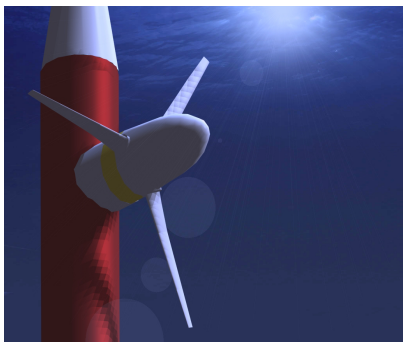

Figure 1. Horizontal axis turbine [7]

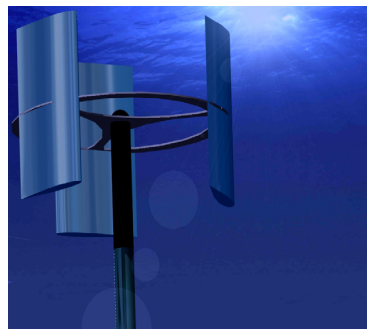

Figure 2. Vertical axis turbine [7]

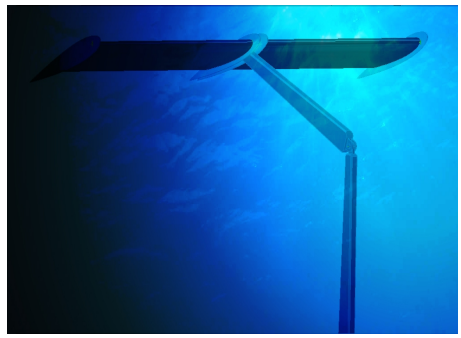

Figure 3. Oscillating Hydrofoil [7]

This is design is similar in concept to the widespread horizontal axis wind turbine and is the most common turbine concept. The blades turn in the tidal stream and the higher density of water means that although the blades are smaller and turn more slowly, they still deliver a significant amount of power. Axial flow rotors are used to drive a generator via a gearbox similar to a hydro-electric or wind turbine. The power units of each system are mounted on hydrofoils either side of the tubular steel monopile. To increase the flow and power output from the turbine, concentrators (or shrouds) may be used around the blades to streamline and concentrate the flow towards the rotors.

Vertical axis turbines

Vertical axis turbine that operate in marine currents are based on the same principles as the land based Darrieus machines, named after the French engineer Georges Darrieus who patented the design in 1931. A Standard darrieus is characterized by its troposkein (eggbeater) shaped blades. These are tradionally incorporated in wind darrieus devices to alleviate centrifugal forces encountered at high rotational speeds. Underwater rotational speeds are likely to be lower and hence our darrieus is a straight bladed H type darrieus.

Oscillating Hydrofoil

Stingray uses a hydrofoil, similar to an airplane's wing but in water, to collect energy from the tide. In this design, hydrofoils have their angle relative to the water stream altered. Lift and drag forces cause the arm to oscillate, and a hydraulic cylinder attached to the main arm subsequently extends and retracts pumping high pressure oil to a generator. This oil passes through a hydraulic turbine which drives a generator to produce electricity. Stingray is a seabed mounted machine, designed for use in water up to a depth of 100m.

The technology developed by Marine Current Turbines Ltd works much like submerged windmills, but driven by flowing water rather than air. They can be installed in the sea at places with high tidal current velocities, or in places with fast enough continuous ocean currents, to take out copious quantities of energy from these huge volumes of flowing water.

The technology being deployed by MCT, known as "Seagen" consists of twin axial flow rotors of 15m to 20m in diameter (the size depending on local site conditions), each driving a generator via a gearbox much like a hydro-electric turbine or a wind turbine. These turbines have a patented feature by which the rotor blades can be pitched through 180^{o} in order to allow them to operate in bi-direction flows – that is on both the ebb and the flood tides. The twin power units of each system are mounted on wing-like extensions either side of a tubular steel monopile some 3m in diameter and the complete wing with its power units can be raised above sea level to permit safe and reliable maintenance.

Figure 4. SeaGen in Strangford Lough [6]

Figure 5. Completely submerged multi-rotor system patented by MCT for deep water [6]

4. Displacements

Marine Current Turbines Ltd propose to use for ***shallower water*** the displacement show in figure 5.

Marine Current Turbines Ltd has also been developing technology for use in ***deep water***. These designs are being constantly refined thanks to real data and experience from the manufacture, installation and commissioning of the existing machines.

The most accessible and therefore the first tidal energy resources to be tapped are in relatively shallow water (around 30m). This is partly because flows tend to be faster in shallower water, and partly because grid connection is easier. At these depths it makes economic sense to have access to the equipment above the surface for maintenance.

However, the available energy resource at this depth is finite, and MCT's deep water technology is well advanced and has all the same technical advantages of the SeaGen device but can be scaled to be larger and more cost-effective and it can also operate entirely submerged but with the capability of being surfaced for maintenance, repairs or replacement.

Conclusions

- The installed capacity until 2005 year was modest, about 300MW. The entire world installed capacity, until 2020 year, could be 6TW and regenerative energy, like a no pollutant source, will constitute a great part of this.
- The ocean energy is a great no exploring source but with a big potential. Because of the great pollutant rate, the bigger cost of the limited conventional sources of energy, it is necessary to replaces them with alternative and regenerative sources of energy.
- It is likely that water turbines will initially be deployed in island or coastal communities with strong marine currents and which are isolated from national grid systems, where they are most likely to offer a cost-effective alternative. However, marine currents have the potential to supply significant quantities of energy into the grid systems of many countries. As interest grows, marine current energy is likely to play an increasing role in complementing other energy technologies and contributing to the future global energy supply mix.

References

Coteţiu, A. Consecinţele efectului de seră şi soluţii energetice moderne de rezolvare a crizei climatice, Conferinţa Ştiinţifică cu participare internaţională, Baia Mare, mai 2003.

Miheţ-Popa, L., Nicoară, D. Sisteme neconvenţionale de conversie a energiei. Dezvoltare-tendinţe actuale, Buletinul AGIR, Editura AGIR, 2007
http:/energy.sourceguides.com, Practical Ocean Energy ManagementSystems
www.enerdata.fr/enerdatauk/,
World Energy Statistics Databases Forecasts and Analyses
www.energy.soton.ac.uk
www.marineturbines.com
www.esru.strath.ac.uk

The modelling of the lubricant expulsion effect (squeeze) in the case of the narrow sliding radial bearing

Ioan Marius ALEXANDRESCU , Radu Iacob COTEȚIU ,
Adriana Gabriela COTEȚIU
Technical University of Cluj-Napoca, Romania

Abstract

We present the determining relationship of carriage in non-dimensional form for narrow radial bearings (L/D ≤ 0,6) exposed to shocks and vibrations, as well as the determining relationships of the lubricant minimum thickness in relation to the dynamic loading. We consider only the approaching motion between spindle/axle and bushing on the direction of the center line, without the rotation of the spindle/axle (the case of the non-rotating bearing), so that the effect of the lubricant expulsion be prevalent in the achieving of the self-carrying film.

Keywords

impulse loading, squeeze film, narrow radial bearing.

1 introduction

We consider the closing motion between spindle and bushing on the direction of the center line, without the rotation of the spindle (the case of the non-rotating bearing), so that the lubricant expulsion effect be prevalent in the achieving of the squeeze film.

Nomenclature

L- length of bearing (m); η- viscosity of lubricant (Ns/m^2); h-fluid film thickness (m); G- static loading (N); p-pressure (Pa); F-dynamically loading (N); D-journal diameter (m); Fs_ad-instantaneous squeeze force.

The modelling of the lubricant expulsion effect (squeeze) starts from Reynold's equation, in which we have to consider the terms that contain the closing speed of the two surfaces ($V = -\partial h / \partial t$). Analytically expressed, the Reynolds equation corresponding to this study, within an isothermal approach is

$$\frac{\partial}{\partial x}\left(h^3\frac{\partial p}{\partial x}\right)+\frac{\partial}{\partial z}\left(h^3\frac{\partial p}{\partial z}\right)=12\eta\frac{\partial h}{\partial t}. \tag{1.1}$$

The scheme of a narrow hydrodynamic radial bearing with circular bushing exposed to shocks, modelled in 4 areas, is presented in fig. 1.

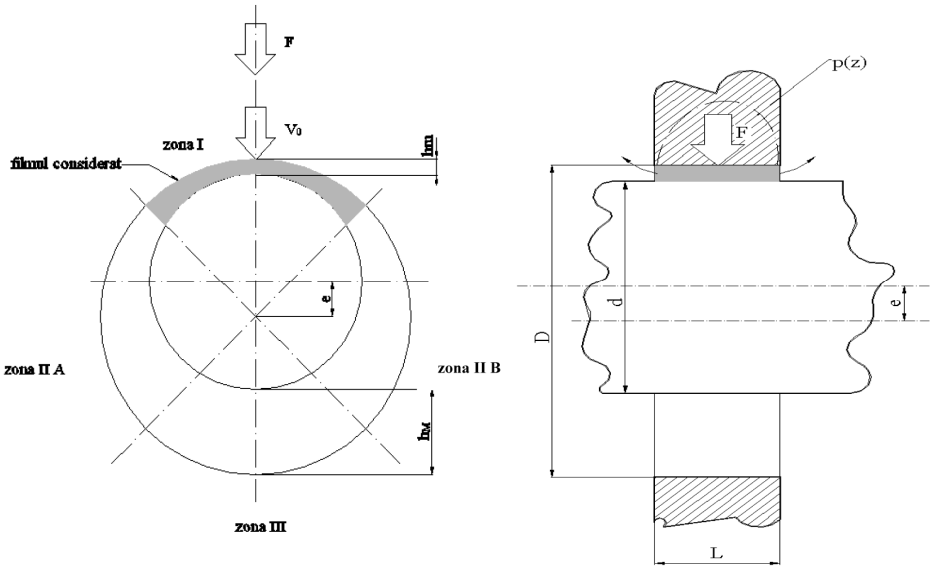

Figure 1. The effect of lubricant expulsion under shock for narrow radial bearing

The simplified modelling of the lubricant film thickness and carriage under the conditions of a closing motion of the spindle/axle and bushing surfaces for the narrow radial bearing exposed to shocks (figure 1) has as starting point the following hypotheses:

- in area III the motion is of separating surfaces, pressure decreases, it can be practically considered constant under the conditions of cavity occurrence;
- in area II A and II B the section remains "approximately" constant and thus the pressure remains constant;
- area I represents the only area that really opposes the closing motion: the geometry of the lubricant film will be approximated with a constant thickness surface, equal to the minimum thickness of the lubricant film under the condition of static loading, on the basis of the rectangular model of infinite length.

We can write

$$h_m = \frac{1}{\sqrt{\frac{1}{h_{m0}^2} + \frac{8F\sqrt{2gH}}{\eta\pi DL^3 g}}}, \tag{2}$$

where h_{m0} represents the minimum thickness of lubricant under static regime, and h_m represents the minimum lubricant thickness in the dynamic regime.

The instantaneous squeeze force has the following expression

$$\overline{F}_s = \frac{1}{A}\left[\overline{H}_s^{\,3}(1+A) - \overline{H}_s^{\,5}\right], \tag{3}$$

where $A = 4\overline{F}\Pi$, $\overline{H}_s = \frac{h_{m0}}{h_m} = H_{s-ad}$ and the parameters of lubricant film expulsion Π have the expression $\Pi = \frac{H}{h_{m0}}$ (H being the height from which the weight dynamically loading the bearing is launched).

2. Teoretical results

The minimum variation of lubricant thickness of the bearing in a dynamic running regime, for three rotations of spindle n= 370 rot/min, n= 600 rot/min and n= 960 rot/min, loading pressures ranging from 0,5 bar to 10 bar, and two static loadings, G=2250 N respectively G=4500 N, are presented in figures 2 – 4.

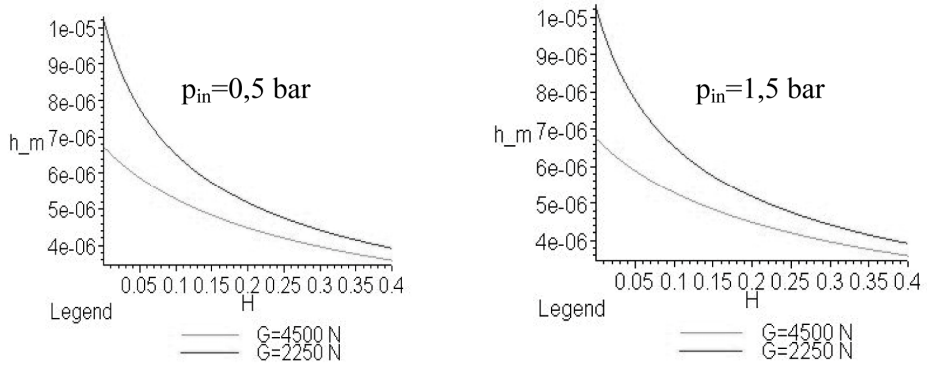

Figure 2. The minimum variation of the lubricant film thickness within a dynamic regime in relation to the weight launching height, H in [m](n=370 rot/min)

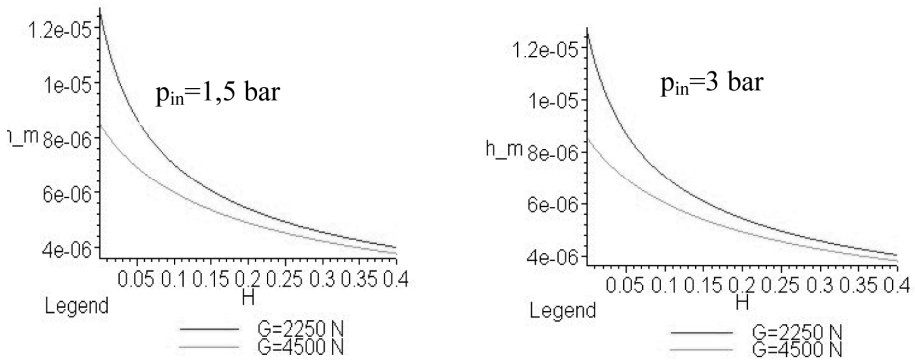

Figure 3. The variation of the minimum lubricant film thickness in a dynamic regime in relation to the weight launching height, H in [m](n=600 rot/min)

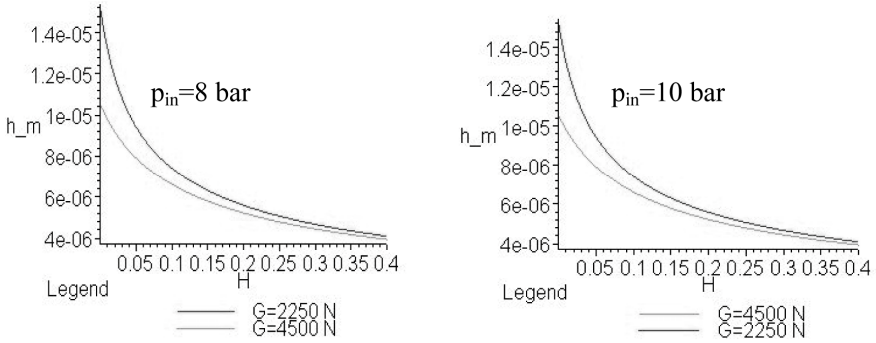

Figre 4. The variation of the lubricant film minimum thickness in dynamic regime in relation to the weight launching height, H in [m] (n=960 rot/min)

The variations of the instantaneous carrying force, in relation to the non-dimensional thickness of the lubricant film for the three weight launching heights H are presented in figures 5-7.

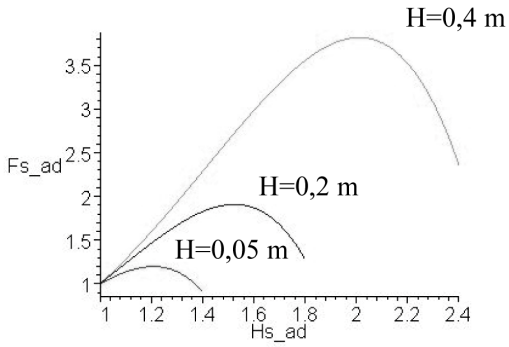

Figre 5. The instantaneous carrying force in relation to the non-dimensional thickness of the lubricant film (G=2250 N, n=370 rot/min, p_{in}=0,5 bar)

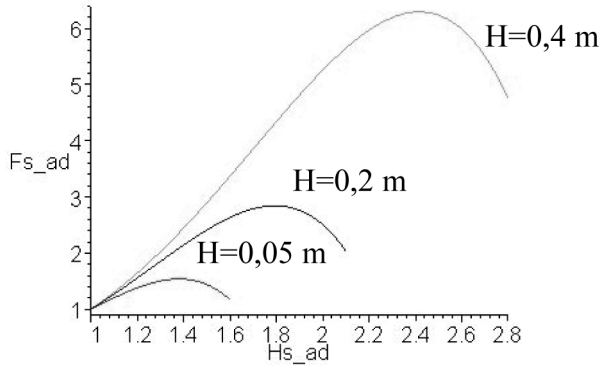

Figre 6. The instantaneous carrying force in relation to the non-dimensional thickness of the lubricant film (G=2250 N, n=600 rot/min, p_{in}=1,5 bar)

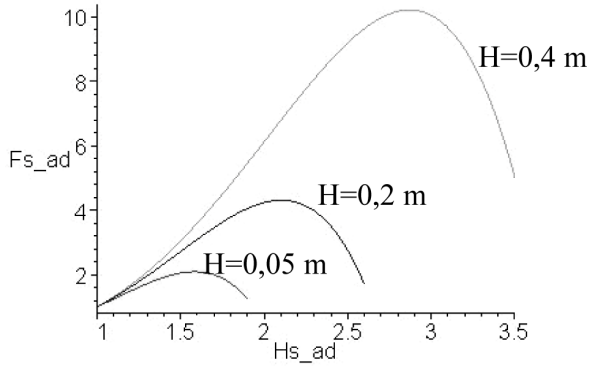

Figure 7. The instantaneous carrying force in relation to the non-dimensional thickness of the lubricant film (G=2250 N, n=960 rot/min, p_{in}=8 bar)

Conclusions

From the analysis of the theoretical results, the following observations can be stated:

- the drastic decrease of the lubricant film minimum thickness along with the increase of dynamic loading (decrease ranging between 50% for the rotation of 370 rot/min, 75% respectively for the rotation of 960 rot/min);
- the decrease of the lubricant film minimum thickness along with the increase of static loading;
- the insignificant influence of the feeding pressure on the minimum thickness of the lubricant for the same rotation of the spindle;
- the decrease, for high dynamic loading (over 2350 N) of the lubricant film thickness under the admissible acceptable value on the basis of

rugosity of spindle surfaces, of the bushing respectively ($h_{min,a} \geq 5$ μm);
- the ratio of film thickness Hs_ad sensitively influences carriage: once the area of maximum is outrun, the carriage rapidly decreases;
- the existence of an optimum point from the viewpoint of carriage: any change in the functional parameters of the bearing leads to straying from the optimum value from the viewpoint of carriage.

References

Alexandrescu, I.M., Coteţiu, R.I., Haragâş, S., Research on the load bearing force in narrow sliding radial bearings (L < 0,7 D) operating in shock conditions. Acta Technica Napocensis, Technical University of Cluj-Napoca, Series Applied Mathematics, Mechanics, and Engineering Vol. 62, Issue II, June, 2019 ISSN 1221-5872, pag. 299-308

Alexandrescu, I. M., Coteţiu R., Darabă, D 2017, Correlations of the instantaneous carrying force and pressure distribution in the case of the narrow sliding radial bearing under hard shocks. Published under licence by IOP Publishing Ltd. IOP Conference Series: Materials Science and Engineering, Volume 174, conference 1 DOI: 10.1088/1757-899X/174/1/012054, WOS: 000399753500054, ISSN print 1757-8981, 2017 (ISI Thomson-ISIWEBOFKNOWLEDGE)

Alexandrescu M., Cotetiu A., Daraba D. (2017), Experimental results regarding the lubricant film thickness to the radial HD working bearing under hard shocks. Scientific Bulletin Series C : Fascicle Mechanics, Tribology, Machine Manufacturing Technology; Baia Mare Vol. 31, pag: 7-12

Alexandrescu M., Cotetiu A., Daraba D. (2016), Correlations Regarding Lubricant Film Thickness to the Narrow Sliding Radial Bearing Working under Hard Shocks. Scientific Bulletin Series C : Fascicle Mechanics, Tribology, Machine Manufacturing Technology; Baia Mare Vol. 30, pag: 2-5

Overload test for machine cut and 3D printed polymer spur gears

Miklós ODROBINA, Róbert KERESZTES, Gábor KALÁCSKA
Department of Maintenance of Machinery
Institute for Mechanical Engineering Technology
Szent István University, Gödöllő, Hungary

Abstract

Spur gears are the simplest and widely used in many applications. In recent years metal gears have been replaced by plastic gears because of their advantageous properties. Despite their many benefits, the load-carrying capacity of plastic is limited. The teeth of gear generally fail when load is exceeded a defined limit. For this reason, it is required to explore substitute materials and manufacturing technology for the gears. Along the traditional plastic technologies additive manufacturing technology have been emerged and they provide a rapid production and reduction of costs. In addition, its materials assure adequate strength. In this work plastic gears have been manufactured by machine cut and additive manufacturing technology. This paper presents the limit of load carrying capacity of acetal and ABS plus gears with low speed and high load without wear.

Keywords

polymer gear, spur gear, 3D printed gear, overload test

1. Introduction

In the last decade, the role of plastic gears has grown in industrial applications. The reason is that in many cases their properties are much more advantageous than metal gears. These gears are mostly made by injection molding or machine cutting, but additive technologies have increasing importance in many areas of the production. These technologies may already be suitable for the production of high-quality gears [Gupta, 2018]. To prove this, more researches are working on mapping of the properties and usability of 3D printed parts. It is still questionable whether gears made by additive technology currently have adequate strength parameters. Geometries can be created by 3D printing technology that are not possible with conventional manufacturing [Chen et al., 2016]. Additive technology deserves special attention as it can reduce manufacturing waste to a minimum compared to conventional technology and can therefore be a good alternative in many applications. Further, internal

passages or stiffeners can be formed by this process which would also make them suitable for special applications [Rodríguez et al., 2003].

2. Experimental

Gear materials and details

Polyoxymethylene copolymer (POM C) and Acrylonitrile butadiene styrene plus (ABS^+) gears were mated against a steel (S355JR) gear. The POM C gears were made from commercially available copolymer (DOCACETAL C) rods by machine cut. The ABS^+ gears were printed from ABS plus filament by rapid prototyping technology. More studies have reported that ABS plus has higher strength and flexibility than normal ABS, therefore, ABS plus filament was choosed for gear material [Lee et al., 2013]. Spur gears with an involute geometry were selected because of its common use. The specifications of the gears are summarized in Table 1.

Table 1. Tested gears specification

	Driving steel gear/pinion	Driven POM C gear/wheel	Driven ABS plus gear/wheel
Module (mm)	1,25	1,25	1,25
Tooth number	47	47	47
Face width (mm)	12	12	12
Pressure angle (°)	20	20	20
Contact ratio	1,61	1,61	1,61

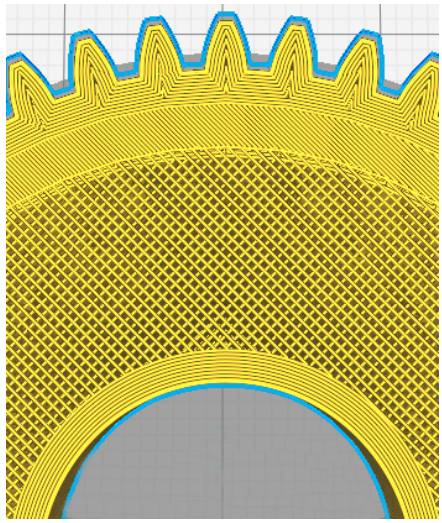

Figure 1. 3D printed strategy for gear

The strength of 3D printed parts depends on the layer orientation [Es-Said et al., 2000]. Therefore, a special printing strategy was used which is advantageous for load-carrying capacity of gear teeth, as shown in Fig. 1. The ABS plus gears were manufactured by Wanhao Duplicator 6 3D printer.

Gear test rig

There are four frequently occurring modes of failure in polymer gears, such as cracking at root, cracking at pitch circle, wear and pitting. For investigation of these failures, a back to back test rig configuration are usually used where the gears are loaded by predefined torque and speed.

However, a back to back test rig is not capable of investigating such an extreme case like sudden tooth fracture. On this basis, a unique test rig was designed and manufactured at Szent István University to be able to investigate load-carrying capacity of polymer gears and to continuously measure the torque and angular displacements of gears under dry load conditions without wear. The designed test rig, as shown in Fig. 2, is used for one extreme case of failure to investigate the overload resulting from a combination of high load and low speed, where torque is continuously increased until fracture. The test rig simulates the situation when a gear gets stuck.

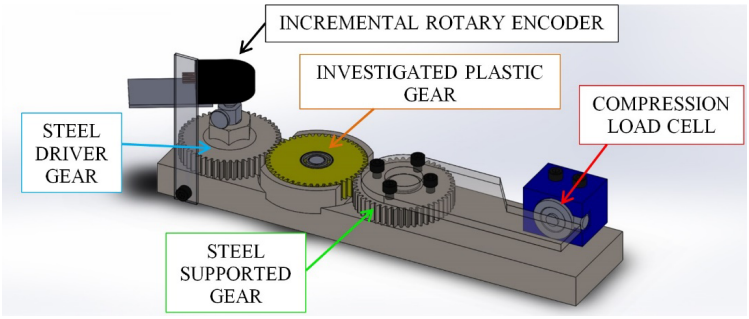

Figure 2. Test rig

The test rig consists of three identical geometry gears and two sensors. Two of three gears, which are made from steel, are responsible for transmission of load because of its higher strength. The plastic gear, which aligns between the steel gears, are investigated. Force and deformation are continuously measured by a load cell and an incremental rotary encoder, respectively. For recording of values a HBM Spider8 amplifier was used.

3. Results and discussion

The torque and angular displacement of the POM C and ABS plus gears running against a steel gear as a function of time at the room temperature is shown in

Fig. 3. At a torque of 99,7 Nm the POM C gear failed after 6 degree whereas 3D printed ABS plus gear already failed at a torque of 39,3 Nm but the angular displacement was the same, 6 degree. Brittle behaviour was indicated at the fracture of teeth by both gears. However, POM C gears bore approximately 2x load at the same deformation like ABS plus gears. To prove this fact, more studies are needed.

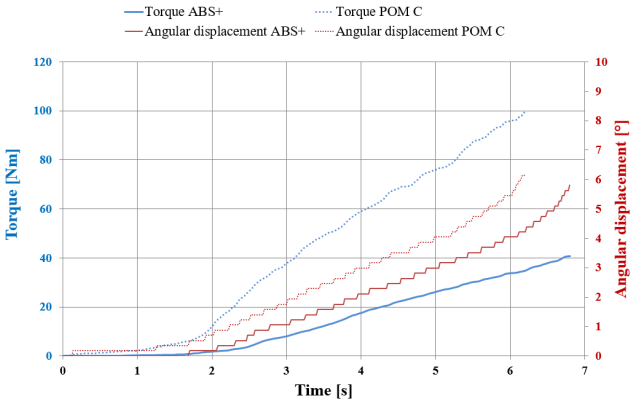

Figure 3. Overload test diagram of POM C and ABS plus gear

The average values of torque and angular displacement in respect of materials are collected in Fig. 4. The results of POM C and ABS plus gears show the fractures of teeth occurred at torque of 98 ± 4,1 Nm, 35,2 ± 4,3 Nm and at degree of 6,5 ± 0,4 °, 6,2 ± 0,2 °, respectively.

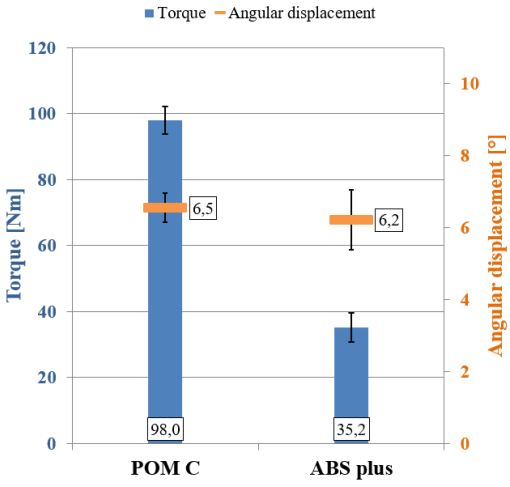

Figure 4. Average torque and angular displacement values as a function of gear materials

In all cases of ABS plus gears test, the loaded teeth and their underlying layer separated from the body of gear. There are more reasons for this, one being that on the bondings are weaker between the layers which reduced the strength of 3D printed part [Ahn et al., 2016]. Another reason for lower load-carrying capacity is the print error which is shown in Fig. 5. The Wanhao 3D printer made a clearance at the bottom side of teeth, as was not able to fill in available area.

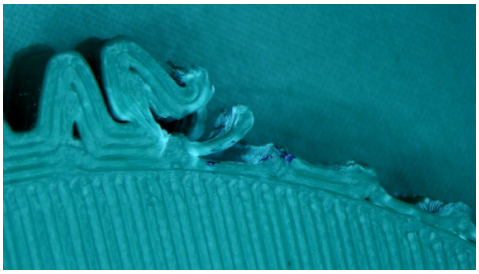

Figure 5. Fractured teeth of ABS plus gear

Conclusion

Overall, this study shows that gears made by additive manufacturing technology fall behind the load-carrying capacity of the conventional plastic gears, like POM C. However, the applications of 3D printed gears have their own field but with their limit of load-carrying capacity that must be taken under consideration.

Acknowledgement

SUPPORTED BY THE ÚNKP-19-3-I NEW NATIONAL EXCELLENCE PROGRAM OF THE MINISTRY FOR INNOVATION AND TECHNOLOGY.

Új Nemzeti Kiválóság Program

NATIONAL RESEARCH, DEVELOPMENT AND INNOVATION OFFICE HUNGARY

References

Ahn, S., Montero, M., Odell, D., Roundy, S., Wright, P. K. (2002): Anisotropic material properties of fused deposition modeling ABS. Rapid Prototyping Journal, Vol. 8, No. 4., pp. 248–257.

Chen L., He Y., Yang Y., Niu S., Ren H. (2016): The research status and development trend of additive manufacturing technology. The International Journal of Advanced Manufacturing Technology, Vol. 89., pp. 3651-3660.

Es-Said, O.S., Foyos J., Noorani R., Mendelson M., Marloth R., Pregger B.A. (2000): Effect of Layer Orientation on Mechanical Properties of Rapid Prototyped Samples. Materials and Manufacturing Processes, Vol. 15, Issue 1., pp. 107–122.

Gupta K. (2018): Recent Developments in Additive Manufacturing of Gears: A Review. Advances in Manufacturing Technology XXXII P. Thorvald and K. Case, IOS Press, pp. 131-136.

Lee J., Huang A. (2013): Fatigue analysis of FDM materials. Rapid Prototyping Journal, Vol. 19 No. 4, pp. 291-299.

Rodríguez J.F., Thomas J.P., Renaud J.E. (2003): Design of Fused-Deposition ABS Components for Stiffness and Strength. Journal of Mechanical Design, Vol. 125., pp. 545-551.

Safety functions of proportional pneumatic linear drives

Eszter SARKÖZI, László FÖLDI
Department of Mechatronics
Institute for Mechanical Engineering Technology
Szent István University, Gödöllő, Hungary

Abstract

In this paper three safety functions of servopneumatic systems are examined and evaluated through simulation tests. These functions are the following safety-related stop functions initiated by safeguard: switching off pneumatic power, pneumatic stopping and movement reversing. The evaluated parameters are: overrun, overshoot, reaction time and minimum required safety distance.

Keywords

servopneumatics, pneumatic positioning, proportional pneumatic, safety function, performance level, diagnostic coverage

1. Introduction

Safety functions are critical points of any machines. The goal of the safety functions are to prevent any type of physical damage. Beyond the EC Machinery Directive there are several related standards (eg. EN ISO 12100, EN ISO 13849-1), which describe the risk assessment process. In the following a risk analysis and evaluation of a servopneumatic system is performed with three different safety functions according to the related standards.

2. Safety functions used in pneumatic systems

The safety functions of pneumatic systems are shown in Figure 1. The most commonly used safety function (SF) is the safety-related stop function initiated by safeguard.

This safety function can be realized by exhausting the cylinder chambers. This allows us to achieve an energy-free state. The safe state in this case is that when the chamber pressures drop to near zero and the motion stops. (SF1)

Safety-related stop function can be achieved by closing the working fluid in the cylinder chambers so the piston's motion is stopped. With this solution the chambers remain under pressure. The safe state in this case is that when the hazardous movement stops. (SF2)

The third option is to immediately reverse the direction of the motion. The piston is then controlled towards the safe initial position. The safe state in this case is that when the motion stops in the piston's initial position. (SF3)

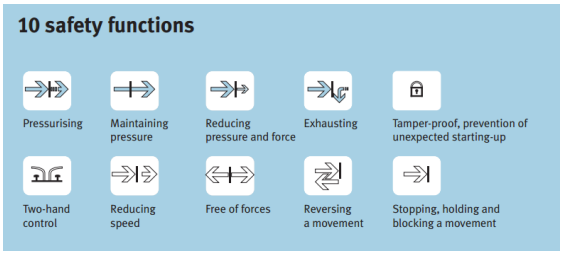

Figure 1. Technical safety functions [www.festo.com]

3. Tested servo pneumatic system

The circuit diagram of the servopneumatic system assembled in the simulation software is shown in Figure 2. During the tests the piston is controlled from its initial position to the end position by opening the proportional way valve at 40%. Mass moved by the cylinder is 5 kg. In each case, the safety function is triggered at half the stroke at the position of 225 mm. The safety function is always implemented by means of valves SV1 and SV2.

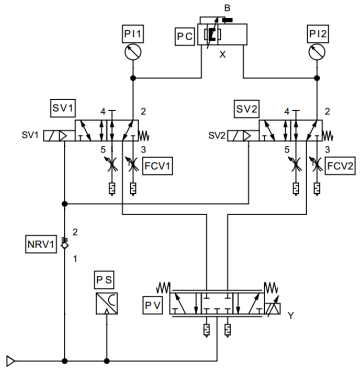

Figure 2. Tested servopneumatic system

The used devices: rodless linear drive with displacement encoder: DGPL-25-400-PPV-A-B-KF-GK-SH (with the symbol PC on the circuit diagram), proportional valve: VPWP-6-L-5-Q8-10-E-G (Qn = 700 L/min) (PV), 5/2 single solenoid switching valves with spring return: VSVA-B-M52-MZH-A1-1R5L (Qn = 1100 L/min) (SV1, SV2), non-return valves: H-QS-8 (Qn = 681 L/min). (NRV), flow control valve: GRU-1/4-B (Qn = 1500 L/min) (FCV), pressure switch: SDE5-D10-

FP-Q6E-P-M8 (PS). The tests were performed in FluidSim 4.2 simulation environment.

4. Behavior of safety functions

In the following, an analysis of the behavior of the three described safety functions is presented through simulation experiments. In every case the valves SV1 and SV2 in operated state allow the compressed air to flow in the direction of 3→2 ports towards the cylinder. When the safety function is triggered, the valves are resetted into initial position by the mechanical springs.

Switching off power (SF1)
In the circuit shown in Figure 3 it can be seen, that when the safety function is triggered, the proportional valve's outlet ports are then closed and the cylinder chambers are exhausted through the 2→1 connections of the SV1 and SV2 valves and the FCV throttle valves.

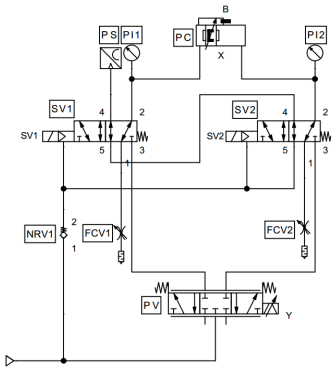

Figure 3. Implementation of switching off power in servopneumatic system

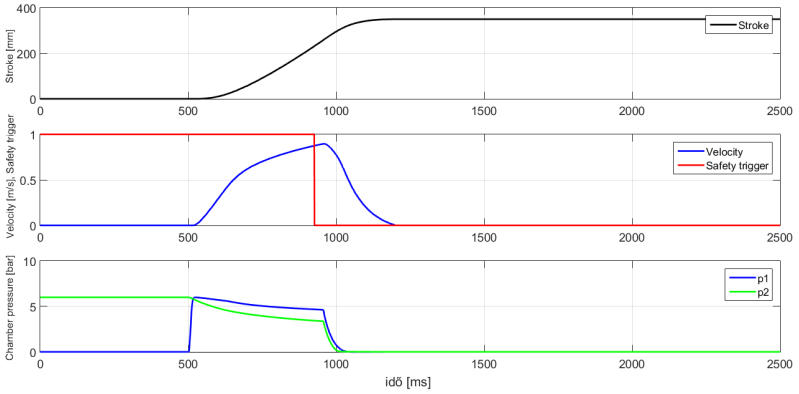

Figure 4. Simulation results (Safety Function: exhausting)

Figure 4 shows the simulation results. It can be clearly seen that the stop triggered at the position of 225 mm only stops the piston at 350.1 mm. Overrun is 125 mm due to inertia of the moving mass. The stop reaction time is 269 ms. The safety distance to be applied in this case is 430.4 mm calculated at a moving speed of 1.6 m / s according to EN ISO 13855.

Pneumatic stopping (SF2)

In the circuit shown in Figure 5 it can be seen, that when the safety function is triggered, the proportional valve's outlet ports are closed and the cylinder chambers are closed as well by the NRV2 and NRV3 check valves through the SV1 and SV2 valves.

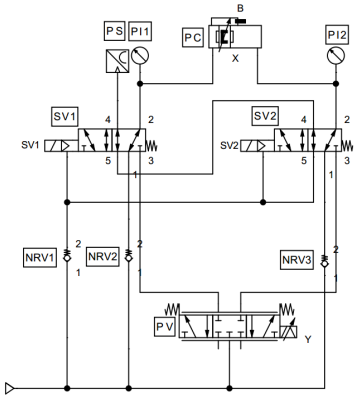

Figure 5. Implementation of pneumatic stopping in servopneumatic system

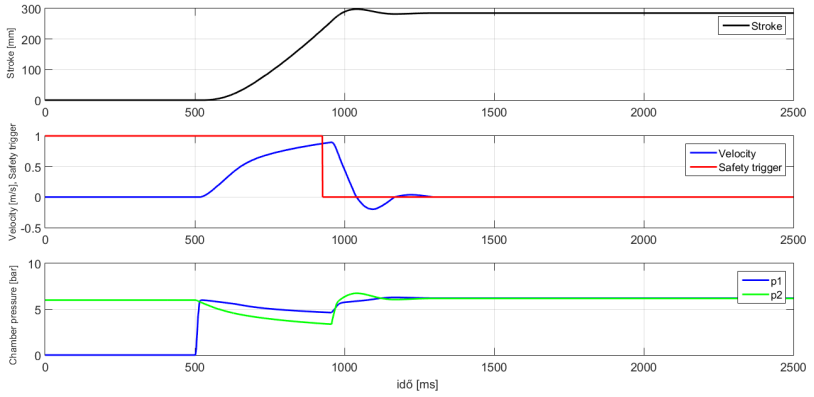

Figure 6. Simulation results (Safety Function: stopping, holding and blocking movement)

Figure 6 shows the simulation results. It can be clearly seen that stopping at a stroke of 225 mm stops the piston with significantly less overrun in this case

than in the previous case. Overrun is 60 mm due to the inertia of the moving mass. Here, however, due to the elasticity of the air, there is an overshoot of 13 mm compared to the steady state. The combined value of the overrun and overshoot is 73 mm. The stop reaction time is 235 ms. The safety distance to be used in this case is 376 mm calculated at a movement speed of 1,6 m/s in accordance with EN ISO 13855.

Pneumatic reversing (SF3)

In the circuit shown in Figure 7 it can be seen, that when the safety function is triggered, the proportional valve's outlet ports are closed. The cylinder's left chamber is exhausted and the right chamber is filled by SV1 and SV2 valves, so the direction of the movement is reversed.

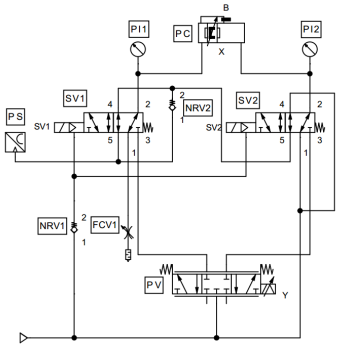

Figure 7. Implementation of reserving a movement in servopneumatic system

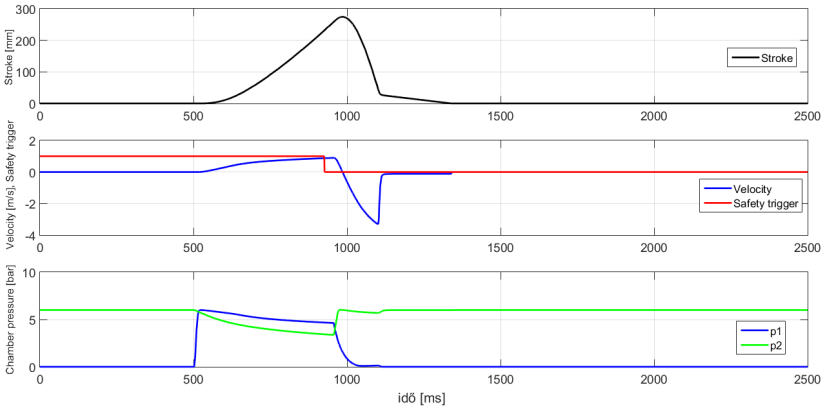

Figure 8. Simulation results (Safety Function: reserving a movement)

Figure 8 shows the simulation results. In the case the overshoot is 49.5 mm, which is also due to the inertia of a moving mass. The stop reaction time is 198

ms. This short stopping reaction time is due the high negative speed. The calculated safety distance is 316 mm at moving speed of 1.6 m/s, according to EN ISO 13855.

Conclusion

Table 1. summarizes the results. The evaluated categories: overrun, overshot, reaction time and the minimum required safety distance.

Table 1. Properties of safety functions

	Exhausting (SF1)	Stopping (SF2)	Reversing (SF3)
Overshoot in mm	-	60	49,5
Overrun in mm	125	13	-
Reaction time in ms	269	235	198
Minimum safety distance in mm	430,4	376	316

Characteristics of the solutions used for all three tested security functions according to MSZ EN ISO 13849-1 are: control category is 2, diagnostic coverage (DCavg) is medium. Indirect monitoring is accomplished by pressure switch (PS). The number of channels is 1, mean time to dangerous failure (MTTFd) is high. The maximum available performance level (PL) is d.

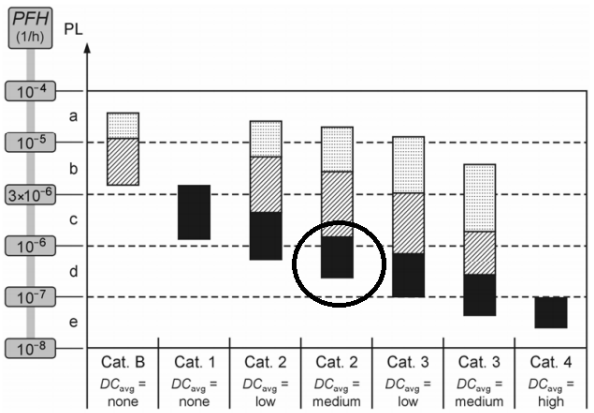

Figure 9. Maximum Performance Level of solutions (SF1-SF2-SF3)

References

EN ISO 13849-1: Safety of machinery - Safety-related parts of control systems - Part 1: General principles for design (2011)

EN ISO 12100: Safety of machinery. General principles for design. Risk assessment and risk reduction (2015)
ISO 13855: Safety of machinery — Positioning of safeguards with respect to the approach speeds of parts of the human body (2010)
BGIA Report 2/2008e (2009) Functoinal safety of machine controls-Application of EN ISO 13849. ISBN: 978-3-88383-793-2. ISSN: 1869-3491
IFA Report 2/2017e (2019) Functional safety of machine controls – Application of EN ISO 13849. ISBN: 978-3-86423-232-9. ISSN: 2190-7994
Safety engineering guidelines. Pneumatic and electric solutions. https://www.festo.com/PDF_Flip/safety/en/files/assets/downloads/Safety%20engineering%20guidelines.%20Pneumatic%20and%20electric%20solutions.pdf

Surface texture optimization of a sliding line contact

Klára BARTHA[1,2], Patrick DE BAETS[1,3], Dieter FAUCONNIER[1,2]
[1]Soete Laboratory, Dept. of Electrical Energy, Metals,
Mechanical Constructions & Systems, Ghent University
[2]Flanders Make@UGent – EEDT- Motion Products
[3]Flanders Make@UGent – EEDT- Decision and Control

Abstract

Applying micro-texture on the surface of mechanical components in lubricated contacts has been proven an effective way to improve their tribological performance in terms of load carrying capacity and friction reduction. Since extensive experimental testing of potentially beneficiary parametric textures in lubricated contacts in order to find the optimal texture is prohibitive, numerical studies gained interest in recent years providing an efficient and flexible solution for investigating various types of textures. In present article, a sliding line-contact with partial texturing in the form of grooves is investigated and the optimal groove parameters are determined. Thereto, the Reynolds equation is solved and coupled to a gradient-based optimization algorithm with the aim of achieving maximal load capacity by varying the depth-to-width ratio and the texture density.

Keywords

Surface texturing, hydrodynamic lubrication, optimization

1. Introduction

In the last decades, applying micro-textures in lubricated contacts has gained the attention of many researchers, since it has been proven that surface texturing can increase the load carrying capacity of the lubricant film [1], while maintaining or reducing the friction. However, in order to obtain these advantageous effects, it is indispensable to find the correct positioning, density and geometrical properties of the textures, such as shape, positioning and dimensions [2], [3], [4]. Many studies focus on finding the optimal value of these crucial texturing parameters in the case of dynamic seals, parallel slider bearings, wedge-shaped thrust bearings and journal bearings [5], [6]. Although experimental studies have been performed in the field, e.g. [7], extensive testing of potentially beneficiary textures e.g. micro-dimples or grooves, characterized by multiple parameters of interest, like, depth, width, positioning, density… is prohibitive because of the high costs and time constrains. Hence, the majority of studies are carried out by means of numerical simulation. Many of these numerical investigations are

limited to parametric studies of textures of interest, in which the thin lubricant film is modelled by Reynolds equation [8]. Such approach involves exploring the entire design space, involving multiple texture parameters, with sufficient resolution, in order to find optimal textures. Hence, it is clear that this process is computationally expensive and not very efficient. Therefore, the use of numerical optimization methods, which target the optimum in design space, without fully exploring it has gained interest [9], [10], [11].

In present article, a grooved sliding line contact is investigated and the optimal depth-to-width ratio and the texture density are determined in order to maximize the load carrying capacity. Thereto, the Reynolds equation, describing the hydrodynamic lubricant film, is coupled to a *Broyden–Fletcher–Goldfarb–Shanno* (BFGS) optimization algorithm to find the optimal design parameters. The BFGS method is a specific realization of the quasi-Newton method for solving unconstrained nonlinear optimization problems.

2. Model

Geometry

The non-conformal parabolic line-contact geometry under investigation represents a long parabolic body, sliding with velocity U over a flat plate. The parabolic surface is textured by equally spaced rectangular grooves which are positioned symmetrically with respect to the centreline of the contact. This is represented in Figure 1

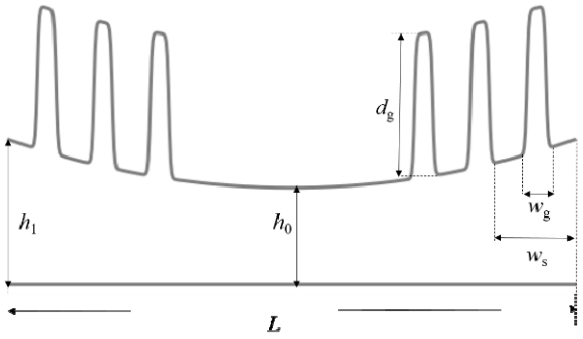

Figure 1. Contact Geometry & Parameters

The lubricant film thickness function along the sliding direction $x \in [0,L]$ can be obtained by the superimposing the texture profile to the parabolic shape

$$h(x) = h_0 + h_c(x) + h_{gi}(x) + h_{go}(x)$$

Here, h_0 represents the minimum film thickness in the contact, whereas the parabolic surface is given by the expression

$$h_c(x) = \frac{4}{L^2}\,(h_1 - h_0)\,\left(\frac{L}{2} - x\right)^2 \tag{1}$$

in which L denotes the length of the contact and h_1 denotes the inlet film thickness

The rectangular groove-texture in the convergent inlet zone is prescribed as

$$h_{gi}(x) = \frac{1}{2} d_g \sum_{i=1}^{n_g} \left[\tanh\left(\gamma\left(x - \left(\left(i - \frac{1}{2}\right) w_s - \frac{w_g}{2}\right)\right)\right) - \tanh\left(\gamma\left(x - \left(\left(i - \frac{1}{2}\right) w_s + \frac{w_g}{2}\right)\right)\right)\right] \tag{2}$$

where n_g is the number of grooves on each side of the main geometry, w_s is the width of the cell containing the groove, and d_g and w_g are the depth and width of the groove, respectively. The scaling factor γ is introduced to adjust the slope of the hyperbolic tangent function. Similarly, the groove-texture at the diverging outlet is prescribed as follows

$$h_{go}(x) = \frac{1}{2} d_g \sum_{i=1}^{n_g} \left[\tanh\left(\gamma\left(x - \left(L - \left(\left(i - \frac{1}{2}\right) w_s + \frac{w_g}{2}\right)\right)\right)\right) - \tanh\left(\gamma\left(x - \left(L - \left(\left(i - \frac{1}{2}\right) w_s - \frac{w_g}{2}\right)\right)\right)\right)\right]. \tag{3}$$

For the numerical analysis in this work, values of sliding velocity, :

Length	L[mm]	L
Minimal height	h_0[mm]	0.01
Maximal height	H_1[mm]	0.02
Sliding velocity	U[mm]	100

Governing equation

The lubricant flow is described by the one dimensional steady-state Reynolds equation in the following form

$$\frac{\partial}{\partial x}\left(\frac{\rho h^3}{12\,\mu}\frac{\partial p}{\partial x}\right) = \frac{U}{2}\,\frac{\partial \rho h}{\partial x}$$

Dirichlet boundary conditions are applied by imposing constant atmospheric pressure at the inlet and the outlet

$$p(0) = p_{atm},$$
$$p(L) = p_{atm}. \tag{5}$$

Reynolds equation are discretized using a 2nd order central finite difference method, and the resulting linear system of equations is solved by means of a Gauss-Seidel method. The characteristic pressure profile is shown in Figure 2.

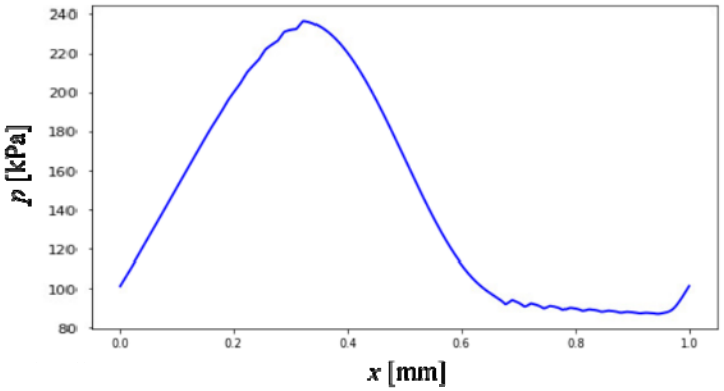

Figure 2. Pressure distribution in the contact

In order to account for the effects of cavitation, the lubricant is modelled as a homogeneous mixture of the liquid and gaseous/vaporous phases. Therefore, the vapour volume fraction α is introduced, defined as follows

$$\alpha(p) = \frac{1}{2}\left(1 + \tanh(A(p - B))\right). \tag{7}$$

The parameters A and B are obtained by imposing the vapour volume fraction at the saturation pressure p_{sat} and the vapour pressure p_{vap} of the lubricant as

$$\alpha(p_{sat}) = 1\%,$$
$$\alpha(p_{vap}) = 99\% \tag{8}$$

The viscosity and the density of the homogeneous mixture are obtained by following linear relationship with the vapour volume fraction.

$$\mu = \mu_L(1 - \alpha) + \mu_V\alpha \tag{9}$$

$$\rho = \rho_L(1 - \alpha) + \rho_V\alpha \tag{10}$$

Following parameters are used throughout the simulations

Table 1. Parameters used in the simulation

Atmospheric pressure	P_{atm} **[Pa]**	**101325**
Saturation pressure	p_{sat} [Pa]	96258
Vapour pressure	p_{vap} [Pa]	19060
Liquid dynamic viscosity	μ_L [Pa s]	0.3
Vapour dynamic viscosity	μ_v [Pa s]	0.359e-3
Liquid density	ρ_L [kg/m^3]	838.393
Vapour density	ρ_v[kg/m^3]	0.896

3. Optimization

In order to obtain the rectangular groove texture which corresponds to the maximal load carrying capacity, an optimization process is performed using the PyGMO toolkit of Python [13]. The optimization is carried out by using the *Broyden–Fletcher–Goldfarb–Shanno* (BFGS) algorithm, which is a quasi-Newton method relying on gradient information. After computing the gradients, a line search is applied to control the step size. The main advantages of the BFGS method, as well as other gradient-based techniques, are that it is computationally efficient and ensures rapid convergence.

The objective function to be maximized is the load capacity which can be derived from the pressure distribution by integration

$$Maximize: W = \int_0^L p(x)\,dx$$

$$Subject\ to: \frac{\partial}{\partial x}\left(\frac{\rho h^3}{12\,\mu}\frac{\partial p}{\partial x}\right) = \frac{U}{2}\frac{\partial \rho h}{\partial x}$$

$$p(0) = p_{atm} = p(L),$$

The integration is performed by applying the Simpson formula. Note that the optimization of the load W, and thus the corresponding pressure profile, has to satisfy the Reynolds equation subject to the boundary conditions, which become the constraints of the optimization problem.

The texture to be optimized consists of a fixed number of grooves, symmetrically positioned around the centre-line of the contact, with a predefined area in which texturing can occur. Two ratios are chosen as the design

parameters, the depth-to-width ratio ε, and the texture density δ defined by the following formulae

$$\varepsilon = \frac{d_g}{w_g}, \tag{12}$$

$$\delta = \frac{w_g}{w_s}. \tag{13}$$

Since the width of the groove cannot be greater than the width of the containing cell, the latter parameter also leads to a bound constraint.

As in the PyGMO software package all problems are treated as minimization, the optimization task has to be reformulated. Most commonly this is solved by minimizing the negative of the original objective function. Therefore the new goal function will read as

$$\min_{\varepsilon,\delta}\left(-\widetilde{W}(\varepsilon,\delta)\right), \tag{14}$$

where $\widetilde{W}$ is the modified form of the load capacity with the constraints added in the form of Lagrange multipliers.

At each iteration step of the BFGS algorithm, the load capacity is calculated for the current value of the design parameters, then their values are changed based on the gradient information and the step size.

4. Results

The contact has been textured with 5 equally spaced grooves on both sides of the centreline, which are restricted to a $x \in [-\frac{L}{3}..\frac{L}{3}]$. Hence, the pitch between to grooves is given as $w_s = 66.67\mu m$, while the width and depth of the grooves result from the optimal value of the design parameters yielding the highest load capacity.

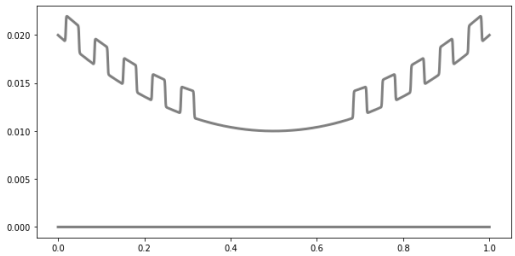

Figure 3. Texture profile with maximal load capacity

After convergence, the BFGS algorithm yielded $\varepsilon = 0.091$ and $\delta = 0.45$ for the optimal values for the depth-to-width ratio and the texture density, respectively. That is, in the optimal texture profile the grooves have a width of $w_g = 30.67\mu m$ and a depth of $d_g = 2.79\mu m$ providing a 2.27% gain in terms of load carrying capacity compared to the untextured case.

Conclusion

In this study, the geometric parameters of the grooves on a partially textured sliding line contact were optimized with the objective of reaching maximal load carrying capacity. The optimization was performed by solving numerically the one-dimensional Reynolds equation then, the load capacity was computed from the resulting pressure distribution. This was given as the objective function of the BFGS algorithm, and the parameters varied were the depth-to-width ratio and texture density of the grooves. The texture profile yielding the optimal groove depth and width was shown, which ensures maximal load capacity for fixed textured area and number of grooves.

Acknowledgement

Klára Bartha is an SB PhD fellow at FWO Research Foundation – Flanders, project number 1S62718N.

References

I. Etsion, L. Burstein, "A Model for Mechanical Seals with Regular Microsurface Structure," Tribology Transactions. 39 (1996) 677–683. doi:10.1080/10402009608983582.

Dobrica, M. B., et al. "Optimizing surface texture for hydrodynamic lubricated contacts using a mass-conserving numerical approach." Proceedings of the Institution of Mechanical Engineers, Part J: Journal of Engineering Tribology 224.8 (2010): 737-750. doi:10.1243/13506501JET673

Etsion, Izhak. "Modeling of surface texturing in hydrodynamic lubrication."Friction 1.3 (2013): 195-209. doi:10.1007/s40544-013-0018-y

Tala-Ighil, Nacer, Michel Fillon, and Patrick Maspeyrot. "Effect of textured area on the performances of a hydrodynamic journal bearing." Tribology International 44.3 (2011): 211-219.

Guzek, A., Podsiadlo, P., & Stachowiak, G. W. (2010). "A unified computational approach to the optimization of surface textures: one dimensional hydrodynamic bearings. " Tribology Online, 5(3), 150-160.

Usman, Ali, and Cheol Woo Park. "Optimizing the tribological performance of textured piston ring–liner contact for reduced frictional losses in SI engine: Warm operating conditions." Tribology International 99 (2016): 224-236.

Křupka, I., and M. Hartl. "The effect of surface texturing on thin EHD lubrication films." Tribology International 40.7 (2007): 1100-1110.
Gropper, Daniel, Ling Wang, and Terry J. Harvey. "Hydrodynamic lubrication of textured surfaces: A review of modeling techniques and key findings."Tribology International 94 (2016): 509-529.
R. Rahmani, A. Shirvani, and H. Shirvani, Tribology International 42, 666 (2009).
R. Rahmani, I. Mirzaee, A. Shirvani, and H. Shirvani, Tribology International 43, 1551 (2010).
C. Shen and M.M. Khonsari, Tribology International 82, 1 (2015).
PyGMO doi:10.5281/zenodo.3464510

ASTM G132 testing for evaluating abrasion resistance of WC-Co hardmetal

Naveenkumar RAJENDHRAN[1], Patrick DE BAETS[1], Shuigen HUANG[2], Jozef VLEUGELS[2], Jacob SUKUMARAN[1]

[1]Laboratory Soete, Department of Electrical Energy, Metals, Mechanical Construction and Systems, Ghent University, Belgium

[2]Department of Materials Engineering, Katholieke Universiteit Leuven, Belgium

Abstract

The current test method experimentally simulates two-body abrasive wear of WC-6wt% Co hardmetal using modified pin abrasion tester configuration (ASTM G132). Silicon carbide (SiC) and alumina (Al_2O_3) with different sizes ranging from 22µm to 200 µm were used as abrasives in this test. Experiments were performed for different normal force from 4 to 16 N with constant sliding speed of 150 mm/s for 30 m sliding distance. Worn surface morphology and topography were characterized through SEM and white light interferometry. The obtained results clearly highlights the potential of pin abrasion tester for characterizing two body abrasion of hardmetals.

Keywords

Pin abrasion tester, cemented carbide, abrasion resistance, ASTM G132

1. Introduction

Hardmetals and cermets are composites materials composed of hard carbide ceramic particles (WC, TiC, TaC and NbC).bonded together by a metallic binder (Ni, Co, Mo, etc.) (Antonov et al., 2010; Huang et al., 2017; Jianxin et al., 2012; Pirso et al., 2011). These materials are widely used in cutting tools and wear parts applications due to its outstanding properties of hardness, toughness and wear resistance (Bonny et al., 2009; Bonny et al., 2010). Earlier research on cutting tool suggests that abrasion is the dominating tribological mechanism in the cutting tool (Astakhov, 2004; Wright et al., 1981), the phenomenon involved in the material removal process may differ significantly (Barrow, 1972). Different mechanism such as oxidation, diffusion and adhesion wear during machining process affect the lifetime of the cutting tool were explored earlier (Astakhov, 2004; Opitz et al., 1968). From materials perspective, tungsten carbide (WC) and cobalt (Co) are the suitable hard and binder phase to achieve better mechanical and abrasion properties (Geoffrey, 1995; Ortner et al., 2014). Grain size and binder ratio are two major controlling factors which affects the mechanical and tribological properties(Zuñega et al., 2012). Generally, the size

of the WC grain ranges from 0.3 to 40 μm and the Co ratio varies from 3 to 30 wt%. The coarse WC (10-40 μm) are mainly used in mining applications (O'Quigley et al., 1997). For metal cutting application, the size of grain typically from1-3 μm and 6 wt% of cobalt are mostly preferred (Jianxin et al., 2012). From the view point of wear prevention, fine grain has greater wear reduction when compared to the coarse microstructure of WC-Co (Saito et al., 2006). There has been considerable interest over a number of years in developing a test rig to simulate and analyze the abrasive wear in laboratory scale.

Several methods has been developed to characterize the abrasion resistance of WC/Co in laboratory scale including single and multiple asperity contact (Gant et al., 2006; Gant et al., 2005; Gee, 2001; Thakare et al., 2012). A scratch tester is mainly explored to check the accumulation of plastic deformation during abrasive wear and damage wear mechanisms of cemented carbide (WC-Co) in single asperity contact (Gee et al., 2011; Zuñega et al., 2012). Multiple asperities pertains to two and three body abrasion by containing hard counterface/asperity/particles is rubbed/trapped against the testing material. This is often used to check the abrasion resistance of materials by controlling the experimental factors such as load, speed, abrasion rate, etc (Gant et al., 2006; Gee et al., 2007). Dry/wet sand rubber wheel based on ASTM G65 standard is common method to produce the three body abrasive wear by passing the abrasives such as silica (SiO_2) and alumina (Al_2O_3) between rubber and sample contact (ASTM, 1991). The major advantage of this test is the fresh abrasive passes through each time during this operation. However, this system suffers with different problems, mainly in controlling the abrasive feed rate (Gant et al., 2006) and it produces only low stress abrasion (ASTM, 2013a). Another abrasion test that has been specifically standardized to check the high stress abrasion resistance of cemented carbide is the ASTM B611 steel wheel slurry abrasion test (ASTM, 2013a). Most of the literatures and ASTM B611 standard suggested that the average particle size of the abrasives/slurry which is used in the test is larger than 500 μm (Gant et al., 2006; Gee et al., 2007). Thus, the standard is only applicable for abrasive size larger than 500 μm. Research has been attested that decrease in the abrasive size remarkably influences the wear mechanism of WC/Co (Krakhmalev, 2008). Moreover, both the standards (G65 and B611) does not clearly represents the contact condition of the cutting tool (Budinski et al., 2017; Krakhmalev et al., 2007). Considering the different contact kinematics, the hardmetals used in the cutting tool application, also needs to be characterised by experiments pertaining to two body abrasion (Larsen-Basse, 1997). A standard test system for two body abrasion is the ASTM G132 (ASTM, 2013b), however this standard is seldom used due to the fact that material removal rate is insufficient to determine the abrasion resistance of hardmetal. Although, a few literatures has been attested that the flat/edge abrasive wear of cemented carbide using pin on abrasive paper under two body dry abrasion conditions (Krakhmalev, 2008; Krakhmalev, 2007; Larsen-Basse, 1997).

The current method improvises the test protocol beyond the standard and compares the abrasive wear of cemented carbide (WC-6%Co) from pin abrasion tester with most widely available literatures data from ASTM G65 and ASTM

B611. The prepared composition of WC-6%Co has similar microstructure and mechanical properties comparable to commercial cemented carbide. The present wear study and the corresponding microstructure correlations also helpful to understand the importance of contact conditions by the influence of different abrasives of cemented carbide under two body abrasion.

2. Material and experimental procedure

Pin abrasion tester (G132)

In this present study, a pin abrasion tester (ASTM G132 standard, see Fig. 1) was selected to experimentally simulate the two body abrasion occurring in a dry-sliding. In the abrasion test, the disc containing abrasive paper rotates whereas the pin mounted on the loading arm moves in the horizontal direction. This simultaneously combined motion results in a spiral sliding path and ensures that the specimen is continuously in contact with fresh abrasives. The required normal load on the pin is applied by means of calibrated weights. The vertical displacement of the sample and the tangential load are monitored to measure the wear and friction coefficient, respectively.

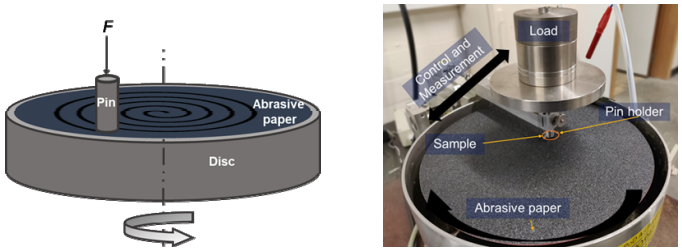

Figure 1. Schematics and photograph of pin abrasion tribotester

Materials and properties

The as sintered WC-6Co (94 vol% WC-6 vol% CO) supplied from MTM KU-Leuven were used as a test material. The hardness of WC-Co is 1383 ±18 Kg/mm^2 measured by Vickers hardness tester with a scale standard of HV_{30}. The calculated density and fracture toughness (K_{IC}) of the WC-Co is 14.765 g/cm^3 and 10.94±0.58 Mpa. $m^{1/2}$. The as-received material was in cylindrical form of 5 mm length and 4 mm diameter and the contact surfaces were machined by EDM. The microstructure of WC-6Co sample were characterized using SEM (FEG JEOL JSM-7600F) (see Fig. 2).

In the microstructure, the dark interconnected structures are the binder content and bright contrast and form of skeleton grains belongs to the carbide phase. The contact surfaces were characterized through 3D roughness investigation and the measurement of roughness data were carried out with a Taylor Hobson type Talysurf CCI white light interferometer. The average surface roughness of the

samples was 0.1±0.05 μm Ra. The specimens were thoroughly cleaned using ultrasonic cleaning in acetone for 15 min. The samples were weighed using an electronic balance with an accuracy of ± 0.0001 gm.

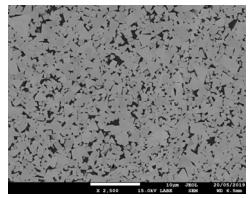

Figure 2. SEM morphology of the WC-6%Co sample

Experimental testing

The testing specimen was linearly loaded starting from 4 to 16 N by means of calibrated weights. Additionally, a load of 2N from the specimen holder is corrected has been used in all the calculations. Two types of abrasive papers namely SiC and Al_2O_3 of different grit sizes such as P800, P180, P120 and P80 were used in the current test matrix. A sliding distance of 30 m (with 3 m intermediate pause for paper change)at a sliding speed of 150 mm/s was used for abrasion testing. To accomplish the 30 m sliding distance the sample holder arm was reinitialized to its starting position at the end of paper change over. The tests were carried out at room temperature, that was measured to be between 24±5°C and relative humidity 40±5 % during all the experiments. The testing conditions were operated based on the test matrix from DOE and each test was repeated three times for repeatability check.

3. Results and discussion

Wear test results

Fig. 3a represents the relationship between volume loss and load for WC-Co with the presence of different size of SiC abrasives (ranging from 22 to 200 μm). The results show that the wear in terms of volume loss increases with increasing load. This probably due to the increment of load should increases the asperity contact between specimen and abrasive paper which further leads to the major material removal from the surface, resulting higher amount of volume loss. On the other hand, the effect of abrasive size on the wear of WC-Co shows that at a certain particle size (critical particle size) the rate of change in wear decreases (Fig. 3b). The volume loss increases significantly with the increase of particle size until the critical particle size of 82 μm is reached, after which the volume loss follows a lower increment rate. The test was repeated three times and the calculated variation shows the test is moderately significant in case SiC particle ($p=0.01$-0.34, 5% significance level)

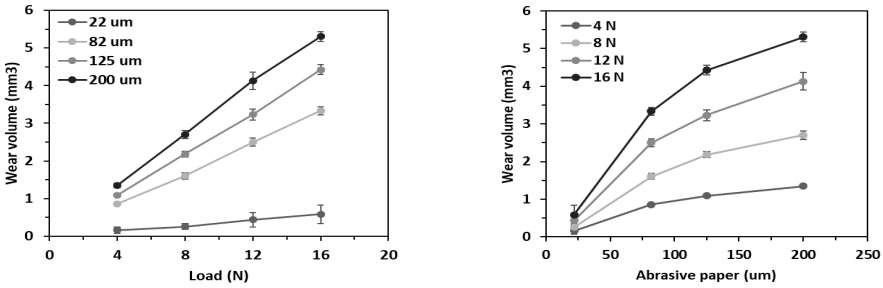

a) b)

Figure 3. Rate of wear volume loss as a function of a) load b) abrasive particle size (SiC)

The relationship between volume loss and load for WC-Co with presence of different size of alumina (Al_2O_3) abrasives (between 22 to 200 µm) is shown in Fig. 4. Similar wear trend were found for WC-Co when tested against alumina and SiC abrasives. The results show that the volume loss of WC-Co using alumina abrasives is lower than SiC abrasives. This is probably due to the hardness of abrasives which plays a major role in material removal.

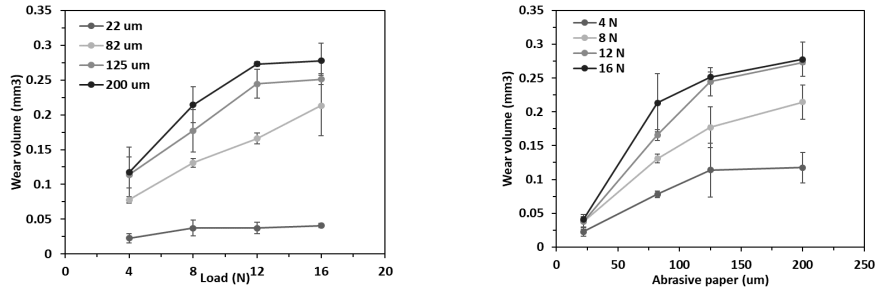

a) b)

Figure 4. Rate of wear volume loss as a function of a) load b) abrasive particle size (Al_2O_3)

Existing literature studies, the severity of contact between the abrasive particle and specimen surface in case of alumina particle is significantly lower compared to SiC particle (Gant et al., 2006; Jia et al., 1996; Thakare et al., 2012). Hence, the removal of material from surface in case of alumina abrasives is low. The calculated statistical variation shows that the is not relatively significant in case of Al_2O_3 abrasives (p=0.17 to 0.38, 5% significance).

Worn surface analysis

The worn surface characteristic was examined in SEM to elucidate the factors influencing the wear and to determine the predominant wear mechanisms (see Fig. 5). The worn surface of different loads with different abrasive sizes illustrates that both plastic deformation of binder, binder removal, grain pull out

and fracture can occur simultaneously (Gant et al., 2006; Krakhmalev, 2008). In case of smaller abrasives (22 μm), the severity of abrasion increased when load increases from 4 to 16 N (groove depth of WC-Co increased from 2±0.5 to 8±1 μm). During initial sliding at lower load, a compressive stresses exerted by the hard SiC abrasive particles results in binder extrusion and removal of binder phase on the WC-Co surface, which leads to loss in mechanical strength and subsequent decrease in the support to carbide hard phase. The removal of binder phase around the carbide grains appears to be caused by plastic grooving which would also result in subsequent ejection of carbide grains (Vashishtha et al., 2017). However, the cracking of carbides due to abrasion using lower abrasives (22 and 82 μm) is relatively low, resulting mild wear. Further, a noticeable increment in the groove width on the WC-Co surface were observed when the size of abrasive increases (Vashishtha et al., 2019). The wear mechanism of WC-Co against larger abrasives (125 and 200 μm) displays combination of extensive cracking of the carbide grains and binder phase extrusion. These extensive carbide cracking further leads to the undermining and ejection of unsupported carbide fragments, resulting in severe wear. The present results are good agreement with the earlier literature based on ASTM G65 standard (Thakare et al., 2012). Additional literatures from ASTM G65 and B611 shows, the overall wear appears to be due to the loss of binder a carbide grains has pulled out from surface as well as the extensively deformed/fragmented carbide grains (Gant et al., 2006; Gant et al., 2005). On the other hand, an alumina abrasive shows higher binder removal in case lower abrasive size (22 and 82 μm) and the trend varies to plastic deformation/plastic grooving when the size of abrasives increased (125 and 200 μm). At 16 N load, an alumina abrasives shows material binder removal and increased plastic deformation along with smaller pullout of grains. The hardness difference between the abrasives plays major role to describe the wear mechanism of WC-Co (Axén et al., 1994; Gant *et al.*, 2006; Jia *et al.*, 1996).

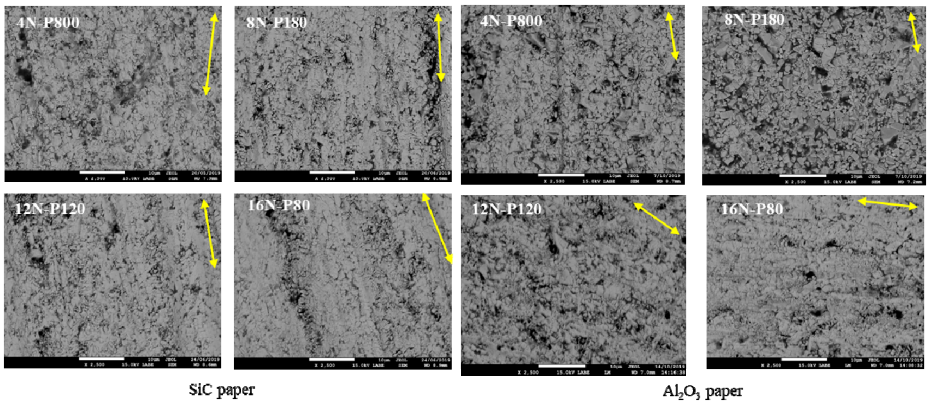

Figure 5. Worn surface morphology of WC-Co after different abrading conditions

Topography analysis

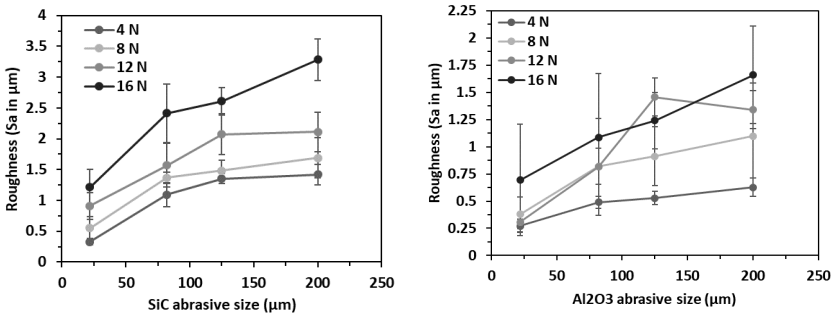

Figure 7. 3D surface roughness of WC-Co worn surface against different abrasives

Fig. 7 illustrates the topographical result of WC-Co under different abrading conditions. The results confirm that the 3D surface roughness of WC-Co increases highly under SiC abrading condition compared to Al_2O_3 abrasives. The effect of particle size also influences the roughness of the WC-Co surface. The fine abrasive (22 µm) shows smooth surface comparatively to the other coarse abrasives. This could be due to the increasing load in case of the fine abrasives leads to the preferential removal of binder (Krakhmalev, 2007). The coarse grade abrasive (200 µm) illustrates high arithmetic mean deviation in both abrasive types. This may be due to the extensive grooving and pull out grain exerted by binder removal as observed from SEM observation.

Comparison with literature data

From wide range of literatures followed by ASTM G65 and ASTM B611 for WC-6%Co (similar microstructure and mechanical properties) (Gant et al., 2006; O'Quigley et al., 1997; Pirso et al., 2011; Roebuck et al., 2007; Thakare et al., 2012), the calculated volume loss has been extracted and compared with the present experimental results, which is graphically represented in Fig. 6. The graph clearly represents the wear in terms of volume loss increases logarithmically when changing the experimental factors such as load, abrasive size, abrasive type, sliding distance, etc. ASTM G65 results specifies the lower volume loss especially when the load (0.2 N) and abrasive size of the particle (4.5 µm) reduced for both SiC, SiO_2 abrasives, which is comparatively lower than the present experimental results. In the case of high load (20 N) and larger SiC abrasive particle (180 µm) at 942 m sliding distance the ASTM G65 result shows the obtained volume loss was 15.07 mm^3. The present study shows the volume loss of WC-Co against 200 µm SiC abrasive at 16 N with a sliding distance of 30 m is 5.3 mm^3. The comparative study clearly confirms the volume loss of the cemented carbide in terms of load and abrasive particle influences more in case of two body contact configuration than three body. ASTM B611 always shows higher amount of material volume due to the fixed experimental

conditions. Generally, the load (200 N) and abrasive particle (600 μm) used in this operation is always higher than the other two standards.

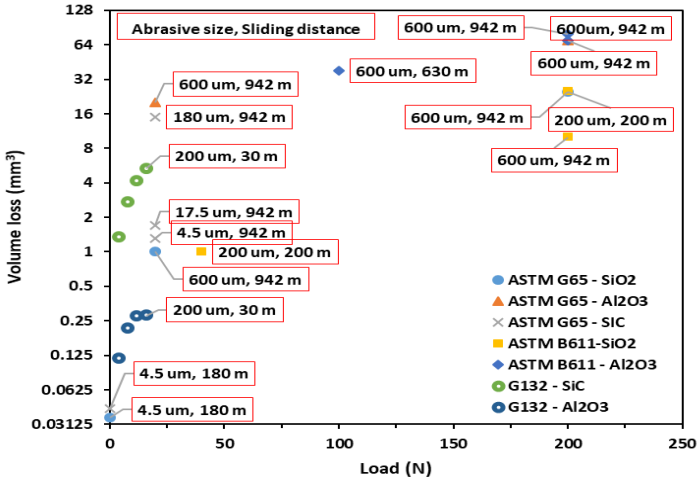

Figure 6. Literature data comparison with the present experimental

Conclusions

The present experimental study concludes the importance of pin abrasion tester in hardmetal testing especially for different abrasive contact using ASTM G132. The test results showed that the effect of abrasive particle size influences highly on the wear in terms of volume loss of WC-Co matrix comparative to the applied load. An influence of different abrasives also shows the effect of wear loss related to the abrasive particle hardness. The wear mechanism concludes the effect of load and particle size of both SiC and Al_2O_3 abrasives leads to the failure mainly fracture of grain, pull out of grain followed by binder extrusion. The experimental results also compared with the widely available literatures and summarized that the pin abrasion tester most effective two body abrasive method to test the hardmetal in lab scale.

Acknowledgements

The work was supported by the Flemish Institute for the promotion of Scientific and Technological research (grant no. FWO. OPR. 2016006101).

References

Antonov, M. and I.J.T.I. Hussainova. (2010), Cermets surface transformation under erosive and abrasive wear, Vol. 43, pp. 1566-1575.

Astakhov, V.P. (2004), The assessment of cutting tool wear, International Journal of Machine Tools and Manufacture, Vol. 44, pp. 637-647.

ASTM. (1991). Standard test method for measuring abrasion using the dry sand/rubber wheel apparatus,*ASTM G65-91* (pp. 231-243).

ASTM. (2013a). Standard Test Method for Determining the High Stress Abrasion Resistance of Hard Materials,*ASTM B611 – 13*. West Conshohocken, PA, USA: ASTM.

ASTM. (2013b). Standard test method for pin abrasion testing,*ASTM G132*. West conshohocken, PA: ASTM.

Axén, N., S. Jacobson and S. Hogmark. (1994), Influence of hardness of the counterbody in three-body abrasive wear – an overlooked hardness effect, Tribology International, Vol. 27, pp. 233-241.

Barrow, G. (1972), Wear of cutting tools, Tribology, Vol. 5, pp. 22-30.

Bonny, K., P. De Baets, W. Ost, S. Huang, J. Vleugels, W. Liuet al. (2009), Influence of electrical discharge machining on the reciprocating sliding friction and wear response of WC–Co cemented carbides, International Journal of Refractory Metals and Hard Materials, Vol. 27, pp. 350-359.

Bonny, K., P. De Baets, J. Van Wittenberghe, Y. Perez Delgado, J. Vleugels, O. Van der Biestet al. (2010), Influence of electrical discharge machining on sliding friction and wear of WC–Ni cemented carbide, Tribology International, Vol. 43, pp. 2333-2344.

Budinski, K.G. and S.T. Budinski. (2017), On replacing three-body abrasion testing with two-body abrasion testing, Wear, Vol. 376-377, pp. 1859-1865.

Gant, A., M.J.I.J.o.R.M. Gee and H. Materials. (2006), Abrasion of tungsten carbide hardmetals using hard counterfaces, Vol. 24, pp. 189-198.

Gant, A.J., M.G. Gee and B. Roebuck. (2005), Rotating wheel abrasion of WC/Co hardmetals, Wear, Vol. 258, pp. 178-188.

Gee, M., A. Gant and B.J.W. Roebuck. (2007), Wear mechanisms in abrasion and erosion of WC/Co and related hardmetals, Vol. 263, pp. 137-148.

Gee, M.G. and L. Nimishakavi. (2011), Model single point abrasion experiments on WC/Co hardmetals, International Journal of Refractory Metals and Hard Materials, Vol. 29, pp. 1-9.

Gee, M.J.W. (2001), Low load multiple scratch tests of ceramics and hard metals, Vol. 250, pp. 264-281.

Geoffrey, E.J.I.J.R.M.H.M. (1995), Spriggs. A. History of fine grained hardmetal, Vol. 13, pp. 241-255.

Huang, S.G., J. Vleugels, H. Mohrbacher and M. Woydt. (2017), Microstructure and tribological performance of NbC-Ni cermets modified by VC and Mo2C, International Journal of Refractory Metals and Hard Materials, Vol. 66, pp. 188-197.

Jia, K. and T.J.W. Fischer. (1996), Abrasion resistance of nanostructured and conventional cemented carbides, Vol. 200, pp. 206-214.

Jianxin, D., Z. Hui, W. Ze, L. Yunsong, Z.J.I.J.o.R.M. Jun and H. Materials. (2012), Friction and wear behaviors of WC/Co cemented carbide tool

materials with different WC grain sizes at temperatures up to 600 C, Vol. 31, pp. 196-204.

Krakhmalev, P.J.T.L. (2008), On the abrasion of ultrafine WC-Co hardmetals by small SiC abrasive, Vol. 30, pp. 35-39.

Krakhmalev, P.V. (2007), Abrasion of ultrafine WC-Co by fine abrasive particles, Transactions of Nonferrous Metals Society of China, Vol. 17, pp. 1287-1293.

Krakhmalev, P.V., J. Sukumaran and A. Gåård. (2007), How hardmetals react to wear: Nano is not always the best, Metal Powder Report, Vol. 62, pp. 30-35.

Larsen-Basse, J. (1997), Friction in two-body abrasive wear of a WC-Co composite by SiC, Wear, Vol. 205, pp. 231-235.

O'Quigley, D.G.F., S. Luyckx and M.N. James. (1997), An empirical ranking of a wide range of WC-Co grades in terms of their abrasion resistance measured by the ASTM standard B 611-85 test, International Journal of Refractory Metals and Hard Materials, Vol. 15, pp. 73-79.

Opitz, H. and W. KÖNig. (1968). ON THE WEAR OF CUTTING TOOLS. In S. A. Tobias & F. Koenigsberger (Eds.), *Advances in Machine Tool Design and Research 1967* (pp. 173-190): Pergamon.

Ortner, H.M., P. Ettmayer and H. Kolaska. (2014), The history of the technological progress of hardmetals, International Journal of Refractory Metals and Hard Materials, Vol. 44, pp. 148-159.

Pirso, J., M. Viljus, S. Letunovitš, K. Juhani and R.J.W. Joost. (2011), Three-body abrasive wear of cermets, Vol. 271, pp. 2868-2878.

Roebuck, B., A.J. Gant and M.G. Gee. (2007), Abrasion and toughness property maps for WC/Co hardmetals, Powder Metallurgy, Vol. 50, pp. 111-114.

Saito, H., A. Iwabuchi and T.J.W. Shimizu. (2006), Effects of Co content and WC grain size on wear of WC cemented carbide, Vol. 261, pp. 126-132.

Thakare, M., J. Wharton, R. Wood and C.J.W. Menger. (2012), Effect of abrasive particle size and the influence of microstructure on the wear mechanisms in wear-resistant materials, Vol. 276, pp. 16-28.

Vashishtha, N., R.K. Khatirkar and S.G. Sapate. (2017), Tribological behaviour of HVOF sprayed WC-12Co, WC-10Co-4Cr and Cr3C2−25NiCr coatings, Tribology International, Vol. 105, pp. 55-68.

Vashishtha, N. and S. Sapate. (2019), Effect of Experimental Parameters on Wear Response of Thermally Sprayed Carbide Based Coatings %J Materials Research, Vol. 22, pp.

Wright, P.K. and A. Bagchi. (1981), Wear mechanisms that dominate tool-life in machining, Journal of Applied Metalworking, Vol. 1, pp. 15.

Zuñega, J.C.P., M.G. Gee, R.J.K. Wood and J. Walker. (2012), Scratch testing of WC/Co hardmetals, Tribology International, Vol. 54, pp. 77-86.

CNC laser engraver quality testing

Tamás ORBÁN, Mátyás ANDÓ
Faculty of Informatics, Savaria Institute of Technology,
Eötvös Loránd University,

Abstract

This paper gives results of the experimental research referring to marking with low power lasers on different materials, with simultaneous 3 axis CNC milling machine. Laser movement is controlled by conventional G-Code, which was partly modified. During test runs the effect of feedrate on line width, the positioning accuracy on different feedrate, line width with different laser power output were observed. In the case of interpolation, the width of the markings increases considerably due to the momentary stoppage of the CNC machine; it has been found that the width of the mark is primarily determined by the feedrate, but is also influenced by the material's reflectivity and thermal conductivity.

Keywords

CNC laser, laser engraving, G-Code, feedrate, laser quality

1. Introduction

Laser technology is relatively a new technology which has not even reached an age of 50 years [13]. Laser machining is one of the most industrial applications. Material processing could be performed in impulse or in continuous mode. Among the techniques are: cutting, welding, engraving, etching, surface hardening [14]. Laser engraving is used primarily for marking parts during the production, for example: serial number, date of production. Laser as the basis of this machining technologies can be produced in several ways. It can be CO_2 [12], Nd:YAG [11] , disk laser, semiconductor. These have differences in power, quality or efficiency. According to these factors every technology has its own advantages and disadvantages. The differences between laser marking, laser engraving, and laser etching largely must do with what each process does to the marking surface, including how deep the laser goes and how it changes the overall appearance.

2. Materials

Equipment
The basic setup consists a computer, a monitor and the CNC machine. The CNC machine is a DEGEM TP-MI simultaneous 3 axis milling machine. Working

area is 100, 100, 40 mm on the XYZ directions. In this case, just the XY plane which will be in use, Z axis used to set the focal point of the laser beam. The motion along the X, Y, Z axis is moved by a HY200 2220 0210 BY08 motor. These motors have about 1,8 degree / step resolution [1] and with the 1,5-mm pitch of the mechanism the calculated precision is 0,075 mm/step. As the machine has no absolute position sensor after every restart or emergency stop must be sent to zero position. In each direction, there are two micro switches which stops the correlated stepper motor thus the movement.

Figure 1. TP-MI milling machine

The controlling of the axes and the tool is made with conventional G-Code. The machine has its own program which can handle the code and sends the signal through a RS-232 serial port to the CNC machine. Through the program the user can directly move along the axes, set the feedrate, or switch on or off the motor – in this case the laser source.

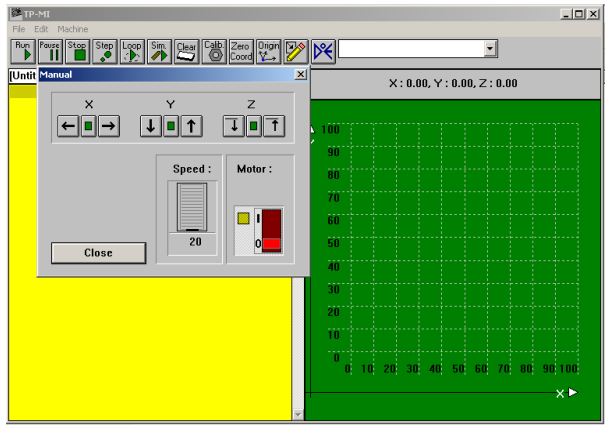

Figure 2. TP-MI-program

In case of the shape is too difficult to write G-Code by hand, an additional software is necessary. Inkscape [3] is an open source drawing program which can generate: single characters, words or even a photo, is not in the suitable format for the G-Code generator. Laser GRBL [2] which is also an open source program, handles PNG, JPG, BMP or SVG as image input file format. After opening the file, several parameters can be set. Such as: the working area, the offset from the sides, the feedrate of the laser motion, the resolution of marking and the codes for switching on or off the laser, even the strength can be set between 0-255 with S-Code, but the test machine does not capable of handling this code. We used M -Code for switch on or off the laser.

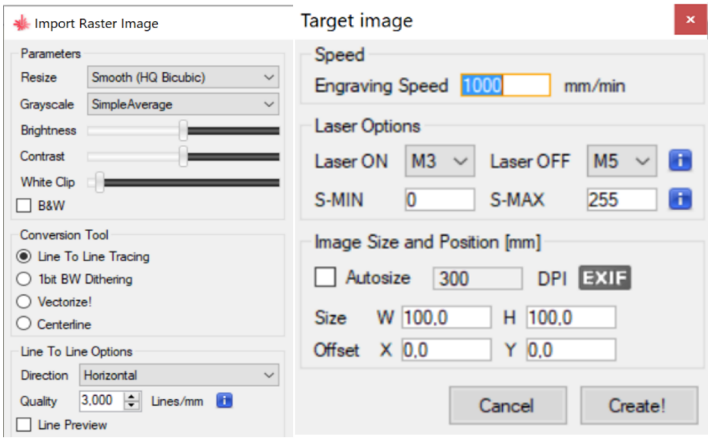

Figure 3. LaserGRBL settings windows

Environment

As the laser beam heats up the material it starts to burn or evaporate. During this process, toxic gases can get released in the air which are harmful for the user. [10] The experiments took place in a good ventilated room and weatherproof outdoor area. The laser itself as a concentrated energy directly or even a reflection could cause sight damage therefore we used safety goggles and darkened polycarbonate and metal shielding to protect the surrounding people in the workshop area.

Laser source

Producing laser for machining, a 2-5-watt power is enough to work with cardboard, wood, plastic or even anodized aluminum. [6] During testing we have used a 500mW semiconductor laser source with 445 nm wavelength unit and a 2.5 W with the same wavelength. These equipment were ordered online, easy to access. The energy supply of the unit come directly from the milling motor cables. Although the voltage is 230 volts with a suitable adapter it can be transformed to a needed level, in this case to 12 volts. This semiconductor based laser diode which

has a TTL control connector but it needs an extra circuit board to handle this. In our case, it is easier to switch on or off the power of the laser. It can be interpreted as M03 and M05 in G-code as giving signal to start the spindle or stopping it.

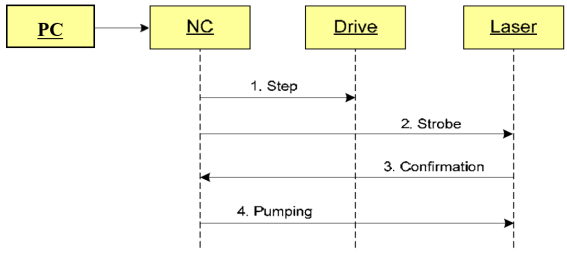

Figure 4. Signal delivery sequence diagram of control and pilot signals during point processing [5]

The Fig.4. above shows the sequence of the process of the motion and laser. As the laser needs time to pump up to emit photons in pulsed mode, it would need a certain delay for reaching the energy level. But as the machining is continuous and the motors also cannot be moved that fast, it has no effect.

3. Method

First, we need to use Inkscape to turn the object to useable format. During importing the picture, the working area needs to be set. Then in the Path Menu „Object to Path" and „Trace Bitmap" should be done. Saving the object to PNG is the next step. The previous step only necessary if the object is not in supported format. In the Laser GRBL program, during opening the type of engraving can be set.

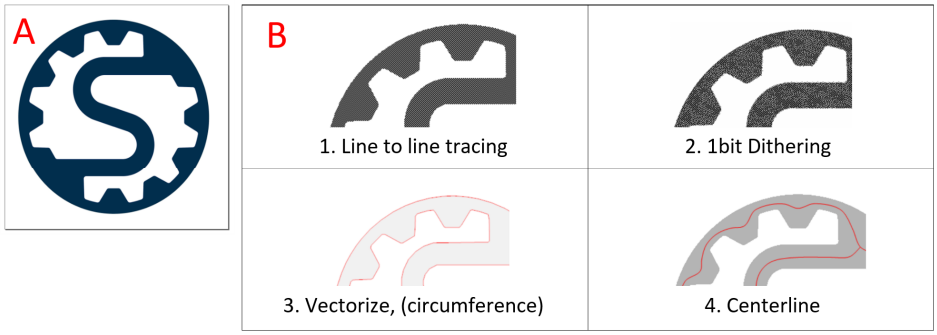

Figure 5. Original logo of Savaria Institute of Technology(A), Different path of engraving (B)

Generated G-code

After the path is generated it can be directly sent to the laser engraver or in that case just save it. The file extension is in .NC. It can be easily opened with Notepad. The generated code is not totally suitable for the controlling program so it needs a bit of work. For example, the M-codes need an extra zero. M03 instead of M3 so we choose MS WORD for changing and adding characters to the generated code with a small macro program and after the correction with another macro it can be saved in .MIT format what the controlling program can open directly.

G0	G00
G1	G01
S0	M05
S255	M03
M5	M05
M3	M03

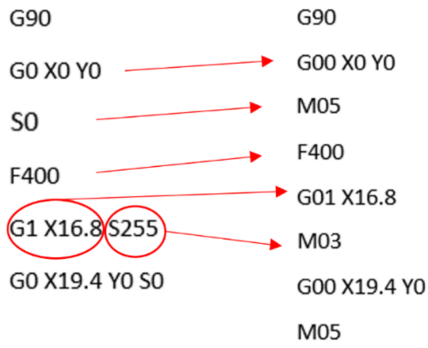

Figure 6. Change table, before-after code change

4. Results

Based on test runs the G01 feedrate could be set faster than the G00 is itself due to some insider software error. G00 feedrate is about 240 mm/min. G01 feedrate worked up to 500 mm/min but on constant work 400 is the highest stable speed, otherwise the stepper motor skips the steps and would not move. Fig. 7.

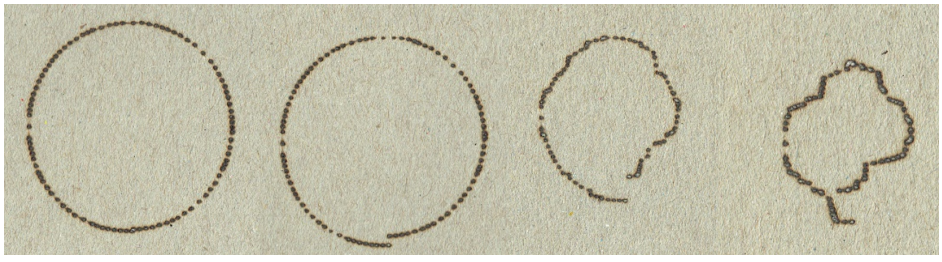

Figure 7. Negative effect of increasing the feedrate: 400, 420,450,500 mm/min

On the scanned probes, we measured the width of the lines in 20 places and calculated an average. The Fig 9. shows the results. It has a suspected linear

characteristic between the feedrate and the width [15]. If the laser goes slower it has more time to burn the target, so it has a bigger mark. As on the Fig. 9., in the second probe with the slowest speed the measured width fell a bit farther from the characteristic line, caused by the spontaneous ignition of the cardboard.

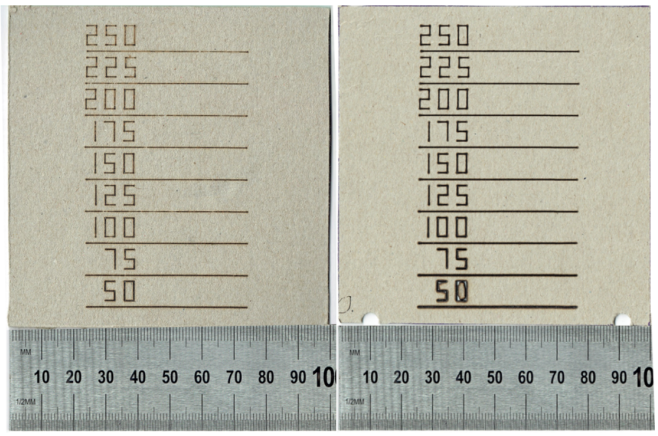

Figure 8. Speed test on cardboard (0.5W left, 2.5W right), numbers mm/min feedrate

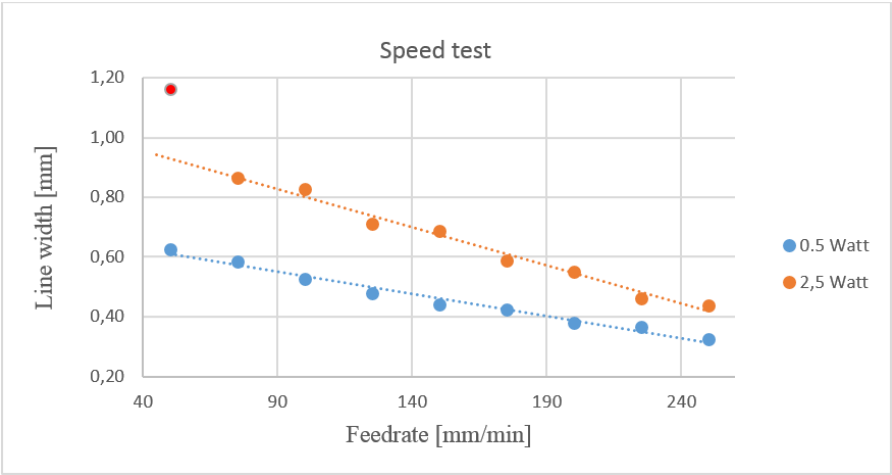

Figure 9. Measured line width

Fig.10. presents, even the radiuses are made of small lines. Therefore, when the machine changes the direction towards the next point it stops for a moment and it is enough time to burn a deeper groove on the cardboard. The stops are caused by the TP-MI program itself. Even without a single character in the code line it took 0,6 seconds in average to read the next code line.

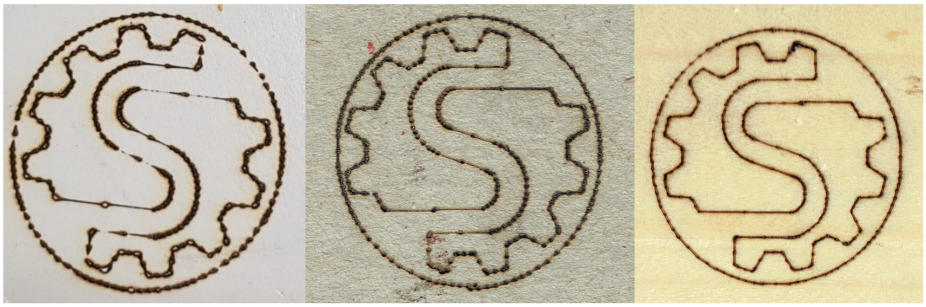

Figure 10. Circumference of the Institute logo (laminated MDF, cardboard, wood plate)

On other materials with better heat conductivity, which absorbs better the heat of the laser and do not reach the temperature above that it changes its color, or with a more reflective surface, the higher the reflectivity, the less percentage of the laser light utilized, is harder to reach the same results. Engraving them, either it needs a stronger laser source, lower feedrate or a denser line structure. Therefore, our 2,5 watt laser was also too weak to make any evaluable results.

Figure 11. Different line density in filled laser marking on cardboard
(3 lines/mm left, 6 lines/mm right)

The density of the lines has big influence in the machining time and it is about linear, so double the density, double the time needed. With the same speed, it took 18 minutes and 9 minutes to engrave these rectangles on the cardboard which are about 20 x 10 mm.

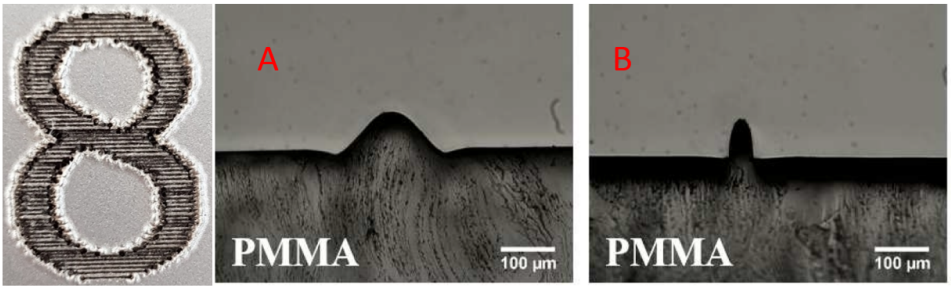

Figure 12. Grey painted black PMMA plastic [8] (5 lines/mm) left, sacrificial layer coated sample: with (A), without coating (B) [12]

The original purpose of trying this material was, making redesigned name plates in the institute. As this material is design for this kind of processing, but the result does not show it, most likely the settings of the machine does not capable to satisfy the expectations. At the starting and ending points of the lines where is the highest energy intake the plastic starts to melt and deforms. This burn down effect appeared during the whole test series. The effect could be excluded with a sacrificial layer which absorbs the

Conclusions

Different materials behave differently even in same circumstances as it is expected. Cardboard burns through, MDF has almost just dots on its surface and plastic partly melts with the same settings.

To reach an acceptable look and quality of engraving a stronger laser source needed, and further experiment with anodized aluminum can be taken with it. Even with higher engraving resolution the machining time could be maintained with higher feedrate. The best solution could be to mount the laser source on to a real size CNC machine on a tool holder. The speed could be tenfold higher, nonetheless resolution or working area. Laser signal would be gained from an empty slot on the machine's PLC. Arduino [9] could be also helpful with the regulation in the power output. As our laser modules have TTL control point, their strength could be changed with PWM. Other solution could be a new type of laser source with higher output and experimenting with it on metal sheets. [6]

References

Servo Control Technology, Hybrid Stepping Motors HY/HS/HN Series datasheet, SCT70010-52/99A, http://www.denfordata.com/bb/download/file.php?id=2707

Laser GRBL Software, http://lasergrbl.com/en/

Inkscape open source vector graphic software, https://www.microsoft.com/en-us/p/inkscape/9pd9bhglfc7h?activetab=pivot:overviewtab

Inkscape Unicorn G-code extension , https://github.com/martymcguire/inkscape-unicorn

Georgi M. Martinov, Alexandr I. Obuhov, Lilija I. Martinova, Anton S. Grigoriev: An Approach to Building a Specialized CNC Systems for Laser Engraving Machining, https://doi.org/10.1016/j.procir.2015.08.103

Laser Engraving Anodized Aluminum, https://jtechphotonics.com/?p=2687

Logo of Savaria Institute of Technology, http://www.szombathelyigepesz.hu/

Rawmark: https://www.rowmark.com/downloads/colorcast-acrylics-reflexions-swatch-page-Űrevised-march-2019

https://www.arduino.cc/
https://www.rowmark.com/techdocs/prop65

M. H. Rahimi, M. Shayganmaneshm R. Noorossanam F. Pazhuheian: Modelling and optimization of laser engraving qualitative characteristics of Al-SiC composite using response surface methodology and artificial neural networks https://doi.org/10.1016/j.optlastec.2018.10.058

Lonjun Gu, Goudong Yu, Cheuk-Wing Li: A fast and low-cost microfabrication approach for six types of thermoplastic substrates with reduced feature size and minimized bulges using sacrificial layer assisted laser engraving https://doi.org/10.1016/j.aca.2017.10.030

Gould, R. Gordon (1959) "The LASER, Light Amplification by Stimulated Emission of Radiation" In franken, P.A.; Sands R.H (eds.). The Ann Arbor Conference on Optical Pumping, the University of Michigan, 15-18 June 1959. p. 128 OCLA 02460155

Ali Khorram, Akbar Davoodi Jamaloei: Nd:YAG laser surface hardening of AISI 431 stainless steel; mechanical and metallurgical investigation https://doi.org/10.1016/j.optlastec.2019.105617

C. Leone, V Lopresto, I De Iorio: Wood engraving by Q-switched diode pumped frequency doubled ND:YAG green laser https://doi.org/10.1016/j.optlaseng.2008.06.019

Theoretical analyze of abrasive wear of cylindrical gear

Nicolae UNGUREANU, Miorita UNGUREANU, Mihai BANICA
Technical University of Cluj Napoca, North University Center of Baia Mare

Abstract

The paper present the result of research regarding the theoretical analyze of abrasive wear of cylindrical gear. For theoretical analyze was use MathCAD software. Are presented the results of the mathematical model and a series of graphical analyzes for abrasive wear of the cylindrical gear.

Keywords

abrasive wear, mathCAD

1. Introduction

Wear is a normal phenomenon that occurs during the operation of machines and equipment. Abrasive wear occurs when two surfaces have a relative motion. Is possible to be surfaces with similar properties, surfaces with different properties or surfaces between which to be another particles. The particles can have different sources of origin, from diferent part of machines and equipment, implicitly different type of materials or they can come from outside (example: dust).

Abrasive wear can be divided into two groups: abrasive wear with two bodies and three bodies [1]. In three-body abrasion, particles formed during operation or coming from outside the system cause abrasive wear, while in two bodies, one of the materials plays the role of abrasive.

Abrasive wear has three different forms: micro-cutting, wedge forming and plowing [2]. During the operation of a system, switching from one mode to another can occur and the modes can operate simultaneously [3]. The shape of the abrasive particle, the hardness, the load and the shear resistance at the contact interface determine the state of the abrasive wear [2]. Thus, the abrasive mode is mainly a severe type of wear.

Taking into account the aspects mentioned before, the phenomenon have a particular importance for the gears, which in turn are indispensable components of any machine or equipment.

2. Theoretical calculation of abrasive wear

The theoretical calculation of abrasive wear is based on mathematical model presented by Tudor A. and others [4]. According to this mathematical model, initially is determined the abrasive wear intensity using the relation:

$$I_{uh} = 3{,}5 \cdot 10^{-10} \frac{A \cdot K}{M} \tag{1}$$

The meaning of the terms in the relation is the following:

– A - parameter which characterizes the abrasive particles and which depends on the concentration of the abrasive particles [%], on their average radius [mm] and on the resistance to breaking [MPa]:

$$A = \varepsilon_a^{2/3} \cdot r_a^{0,5} \cdot \sigma_a^{2,5} \tag{2}$$

– M - parameter that characterizes the materials in contact, which depends on the relative deformations to the breaking [%], an exponent specific to each material [4] and the Brinell hardnesses for each surface [daN/mm^2]:

$$M_1 = \varepsilon_1^t \cdot HB_1^{1,5} \cdot HB_2 \tag{3}$$

$$M_2 = \varepsilon_2^t \cdot HB_2^{1,5} \cdot HB_1 \tag{4}$$

– K - parameter that depends on the kinematic factors of the coupling: the radius of reduced curvature in the contact area [mm], the number of request cycles [cycles/h], the tangential velocities at the contact point [mm/s] and the average probabilities of fixing the abrasive particle on the two surfaces:

$$K_1 = \sqrt{\rho_R} \cdot n_{\omega 1} / (\alpha \cdot v_1 + \beta \cdot v_2) \tag{5}$$

$$K_2 = \sqrt{\rho_R} \cdot n_{\omega 2} / (\alpha \cdot v_1 + \beta \cdot v_2) \tag{6}$$

where:

$$\alpha = \frac{HB_2}{HB_1 + HB_2} \tag{7}$$

$$\beta = \frac{HB_1}{HB_1 + HB_2} \tag{8}$$

If the theoretical values necessary for the calculation of the parameters are not known, there is a need for experiments that highlight the abrasive wear intensity.

3. Modeling the abrasive wear process of gears using mathcad

Starting from this mathematical model, modeling was performed using MathCAD. A series of simplifying hypotheses have been made: the values of all the factors necessary for the calculation of the parameters are known, the gear is considered cylindrical type, the tilt angle of the gear teeth is β=0.

The following graphic representations were obtained:

– Dependency between the abrasive wear rate and concentration of the abrasive particles [%], figure 1.

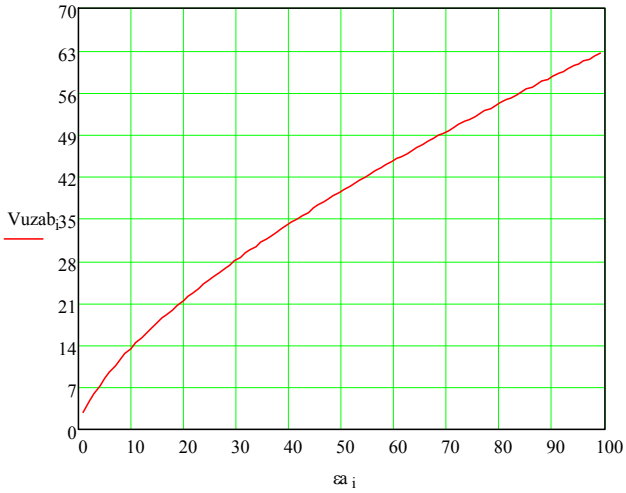

Figure 1.

– Dependency between the abrasive wear rate and Brinell hardnesses for each surface [daN/mm^2], figure 2.

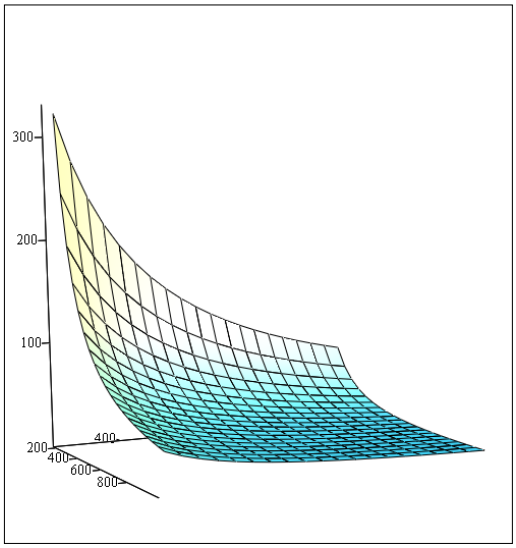

Figure 2.

– Dependency between the abrasive wear rate and the hardnesses of abrasive particle, figure 3.

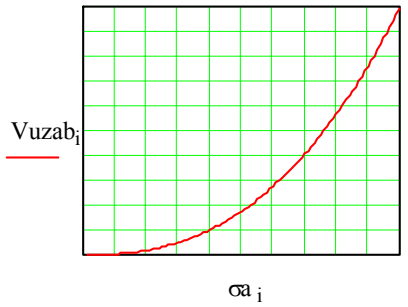

Figure 3.

– Dependency between the abrasive wear rate and the and the number of teeth, figure 4

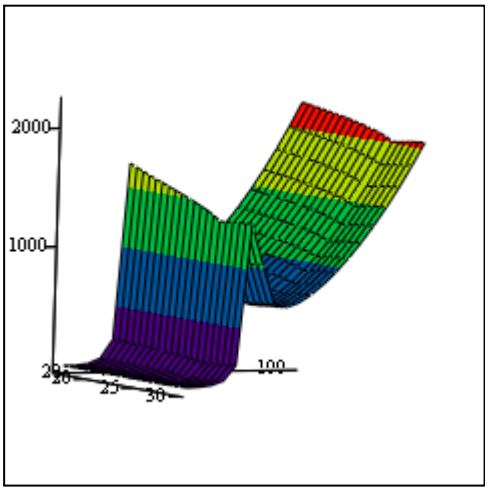

Figure 4.

Conclusion

The calculation of abrasive wear is particularly important due to the implications it has in the durability and reliability calculations of machines and equipment.

Theoretical analysis of the abrasive wear of the gears confirms a number of logical aspects:

- the abrasive wear of the gears increases with the hardness of the abrasive particle and with the increase of the concentration of abrasive particles on the sides of the teeth
- the abrasive wear of the gears decreases with increasing hardness of the teeth

Regarding the relation between the abrasive wear rate and the number of teeth the graphical representation shows a rapid increase of the intensity of abrasive wear followed by a decrease as fast after which there is a continuous increase with the increase in the number of teeth. This conclusion can serve to design the gears so that the number of teeths of the gears to leads to a minimum abrasive wear.

References

Moore MA. A Review of Two-Body Abrasive Wear. 1974;27.

Hokkirigawa K, Kato, K. An Experimental and Theoretical Investigation of Ploughing. Cutting and Wedge formation During Abasive Wear. 1988;21.

Kitsunai H, Kato, K. The Transition Between Microscopic Wea Modes During Repeated Sliding Friction Observed by a Scanning Electron Microscope Tribosystem. 1990;135.

Tudor A., Prodan Ghe., Muntean C., Motoiu R., Durabilitatea si fiabilitatea transmisiilor mecanice, Editura Tehnica , Bucuresti 1988

Novel experimental approaches for the tribological characterization of vegetal lubricants

Alessandro RUGGIERO[1], Nicolae UNGUREANU[2]
[1]Department of Industrial Engineering, University of Salerno, Fisciano, Italy
[2]Faculty of Engineering, North University Center of Baia Mare,
Technical University of Cluj Napoca, Maramures, Romania

Abstract

The environmental and toxicity issues of conventional lubricants as well as their rising cost related to a global shortage and their poor biodegradability led to renewed interest in the development of environmentally friendly lubricants. Environmental legislation by Occupational Safety and Health Administration (OSHA) and other international regulation authorities discourage the use of mineral oil-based lubricant and environmental-harmful additives. This gives increasing demand for green lubricants and lubricant additives in recent years. Products currently available from vegetal based oils include for example tractor transmission hydraulic fluid, industrial hydraulic fluids for process and machinery, metal working oils and coolants, but, in any case, it is necessary a deep rheological and tribological characterization of the vegetal base stocks used for formulate the specific lubricant. The aim of this perspective paper is to illustrate a novel experimental approach for the characterization both the tribological properties and the wear protection ability of investigated vegetal base stocks. With this in mind, even if no experimental results were reported in this paper, a novel and promising design of experiments approach was descripted based on reciprocating tribometer for the tribological oils characterization and on the pin on disk followed by the optical wear debris analysis for the wear protection ability assessment of the investigated base stokes.

Keywords

Vegetal Lubricants; Experimental; Lubrication; Tribometers; Wear protection.

1. Introduction

It is well known [1] that a lubricant means a substance or mixture capable of reducing friction, adhesion, heat, wear and corrosion when introduced between two solid surfaces in relative movement and capable to transmit power. The most common constituent substances are base fluids and additives. 'Base fluid' means a lubricating fluid whose flow, ageing, lubricity and anti-wear properties,

as well as its properties regarding contaminant suspension, have not been improved by the inclusion of additive(s); 'substance' means a chemical element and its compounds in the natural state or obtained by any production process, including any additive necessary to preserve the stability of the products and any impurity deriving from the process used, but excluding any solvent which may be separated without affecting the stability of the substance or changing its composition; 'additive' means a substance or mixture whose primary functions are the improvement of the flow, ageing, lubricity, anti-wear properties or of contaminant suspension.

Lubricants are being utilized in many fields of everyday life and in a variety of industrial applications for lubricating machines components and as metal working fluid during machining. Reports [2] indicate that more than 40 million tons of lubricants for year were used globally in last ten years, with a projected increase over the time [3]. Approximately 85% of lubricants being used around the world are petroleum-based oils [4].

It is a common knowledge that the very great use of petroleum-based oils created many negative effects on environment and about 40-50% of the approximately $5x10^6$ tons of lubricants used in Europe each year contribute to the pollution of the environment, due to principally to about 40% of lubricants that are not properly disposed of.

Moreover, with particular reference to metal working fluids, which contribute to increase productivity and the quality of manufacturing operations by cooling and lubricating during metal forming and cutting processes, it is reported that about 80% of all occupational diseases of operators were due to skin contact with cutting fluids.

Investigations report that only in USA about 700,000 to one million workers are exposed to metal working fluids [5] which may be irritant and allergic.

Although petroleum products could be bio-degraded by natural microorganisms they are not sufficient in quantity of lubricants to be degraded.

For these reasons, the use of environmentally friendly fluids and substances will play in next years an increasingly important role in all the world as well as in Europe in which the revision of the existing EU Ecolabel criteria for lubricants was recently published with the purpose to better define the quality of lubricants in term of impact on environment. The trend in the near future will be to use biodegradable and nontoxic bio-lubricants to prevent accidental pollution and to reduce dependence on mineral oil, especially regarding the total loss of lubricants in machinery that has a high probability of polluting the environment or lubricants that are in contact with food. To solve these issues, environmentally friendly lubricants are under development and investigation using especially vegetable oils as base stock oils, formulated with non-toxic and biodegradable additives [6].

In the framework of an active research project still running, the idea was to select appropriate vegetal base stocks to be investigated, which will be analysed comparing their rheological and tribological properties. For doing that, tribo-

tests will be carried out using tribometers for several characteristic operating conditions (i.e. several lubrication mechanisms) with purpose to obtain the "global" performances of lubricants in term of friction coefficients and wear protection ability. In particular, is possible to investigate this issue by using topographical analysis of worn surface of the lubricated pairs in correspondence of the type of used vegetal oil. Furthermore, the proposed investigation foresees a new activity based on the optical detection and neural network classification of wear debris inside oils used in the tribo-tests.

2. The Novel Experimental Investigation on Vegetal Lubricants

The experimental activities will be developed in cooperation between the laboratories of the Faculty of Engineering, North University Center of Baia Mare, Technical University of Cluj Napoca, Maramures, Romania, the "Department of Industrial Engineering" (DIIn) of the University of Salerno (Italy), the "Departamento de Ingeniería Mecánica, Química y Diseño Industrial" (ETSIDI) of the Universidad Politécnica de Madrid (UPM), Spain, and at the "Czech University of Life Sciences Prague" (CLUS), Faculty of Engineering, "Department of Material Science and Manufacturing Technology", Prague, Czechia.

After selected the appropriate vegetal base stocks to be investigated on the basis of their low oil toxicity level, biodegradability, non-edibility and the large availability of the species from which oils are extracted, the preparation of the oil samples will be performed by the cooperation of CLUS in Prague. In particular, the crude oils will be extracted by the seeds by using a LaborTech MP Test 5.050 machine with an imposed force of 5 KN and a deformation speed of 10 mm min^{-1} in controlled conditions.

Moreover, in order to investigate the effect of a common used procedure of hydrotreating to increase the stability and the lubricity of the raw plant oil [7], the hydrotreated vegetable Rapeseed oil (HVO) will be investigated. The HVO will be obtained by consecutive steps of hydrodeoxygenation, decarboxylation, and decarbonylation [7], obtaining in this way mixture of paraffinic hydrocarbons and is free of sulfur and aromatics. The saturation of the double bonds and removal of oxygen (decarboxylation, decarbonylation, dehydration) conducts toward hydrocarbons.

Physicochemical Properties Measurements Design

The physicochemical characterizations of lubricants base stocks is a preliminary and necessary task for the tribological characterization of a such a kind of lubricant [8]. The physicochemical properties measurements were designed in cooperation with the ETSIDI, UPM in Madrid, Spain, and they will take in to account the density, the kinematic and the dynamic viscosity, the flash point and total acid number (TAN).

In particular for the density measurement a pycnometer of 10 ml will be used in a controlled temperature room at 15 °C. It will be used a distilled water as working liquid with well-known density following the steps of a common and well-known experimental procedure [9].

The viscosity will be determined following the procedure suggested by the ASTM D445-65 Standard [10] by using an "Afora Cannon-Fenske viscometer (Series 300)".

Moreover, with the aim to investigate the Newtonian, pseudoplastic or dilatant fluid behaviour of the selected basestocks a rotational type dynamic viscosity Brookfield (Viscometer RV) will be also used. The measuring principle is based on the detection of the resistant torque acting on a rotor when it rotates in a viscous fluid at different velocities. The cone on plate viscometer (Figure 1) is made by a cone on a flat surface. Either surfaces are in rotation. The fluid to test is interposed in the gap; the semi angular opening of the cone allows the possibility to obtain a constant shear factor acting on the surfaces. The advantage of this apparatus is that a small sample volume of fluid is required. In many of these instruments the fluid temperature is controlled and measured during the tests with pre-heating or cooling external fluid.

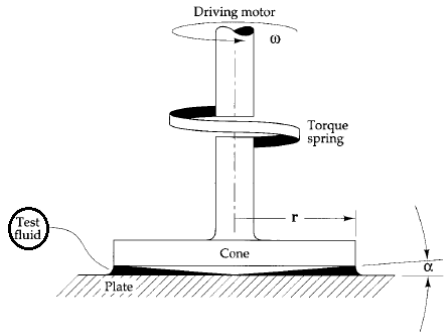

Figure 1. Schematic of a cone on plate viscometer

Acid number will be measured following the ASTM D664 [11] while the base stokes Flash Point (FP) will be measured in the framework of Pensky-Martens ASTN D93 IP 34, by using a Flash Point tester Semi-Automatic DIN 51758.

Tribological Experiments Design

Tribological tests on the selected base stocks aim to characterize both their lubricating performances and their wear protection abilities when used in metal on metal kinematical pairs.

It is well known [1] in a lubricated tribo-system three main lubrication mechanisms should take place depending on the kinematics of the couple, the load conditions, the contact geometry and the rheology of the lubricant.

The lubrication mechanisms are classified as boundary lubrication, mixed lubrication and hydrodynamic/elasto-hydrodynamic lubrication. For the different lubrication modes the coefficient of friction can vary according to the "Stribeck curve" and allows to define the type of lubrication in a tribo-system in correspondence of a certain Gumbel number (Gu = speed x viscosity/load) [8].

Usually, from experimental point of view, the tribological properties of a selected lubricant were usually investigated by others scientists by using several type of tribometers (Pin on Disc, Four Ball Tester, Ball on Disc, Fretting Tester, Four Ball Tester, Reciprocating Sliding Friction) in fixed lubrication conditions (i.e. in a single point of the Stribeck curve). The main novelty of the proposed investigation is the idea to use a reciprocating tribometer (variable velocity during the stroke, Figure 2) to characterize, in each reciprocating stroke, the tested base stock for all the three lubrication types, allowing to plot a very accurate Stribeck curve for each tested vegetal oil.

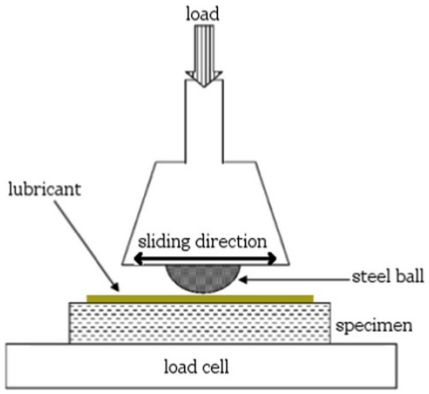

Figure 2. Scheme of the Reciprocating Tribometer @ DIIn -UNISA-

In our experiments, an AISI E52100 steel sphere with the dimension of 10 mm of diameter, is put in contact against a X210Cr12 steel flat specimen with a closure imposed normal load [12]. On the contact surfaces between these two elements the tested base-stocks will be provided. During the reciprocating motion the sliding friction force will be measured by using a load cell applied on the flat body (Figure 2).

In order to achieve all the lubrication type for the three tested oils (different viscosity) loads and reciprocating motion frequencies will be varied in order to achieve different Gumbel numbers during the stroke. In particular the applied loads N will be 10 N and 19 N, while the frequencies of the reciprocating motion will be set at 10 Hz and 20 Hz with a stroke of 8 mm. The reciprocating tests will be executed in conditions of controlled relative humidity H =55 ± 5 % and at ambient temperature of 20°C. Before each test the specimens will be cleaned by using ultrasonic apparatus and alcohol.

The contact ball on flat contact pressure is evaluated by adopting the Hertz theory [8] in details:
The radius r of the circular contact area is:

$$r = 0,908 \cdot \sqrt[3]{\frac{N}{E^*}\frac{1}{D}}$$

$$\frac{1}{E^*} = \frac{1-\nu_1^2}{E_1} - \frac{1-\nu_2^2}{E_2}$$

$$D = \frac{1}{2}\left(\frac{1}{R_1} + \frac{1}{R_1'} + \frac{1}{R_2} + \frac{1}{R_2'}\right)$$

Where, E and ν are respectively the Young modulus and the Poisson ratio of the contact materials, R and R' are the principal curvature radii of the contact surfaces. The calculated value of the mean contact pressure by using N =10N and N= 19 N were respectively 660 MPa and 818 MPa.
The condition which guarantees the establishment of an EHD lubrication mechanism between the surfaces in relative motion corresponds to values of the ratio [8].

$$\Sigma = \frac{h_{min}}{R_a} \geq 1,4$$

The minimum thickness h_{min} [13] of the lubricating film in an elasto-hydrodynamic contact will be computed by the Hamrock (1994) [14] model after measured the viscosity of the oils.

Wear Protection Ability Experiments Design
With the aim to deeply investigate on the wear protection ability and on the type of wear characteristic of each different lubricated tribo-system, a novel investigation was designed based on the optical analysis of used oils and on the detection and the classification of the wear debris suspended in each oil after working in controlled and definite tribological conditions.

In particular the experiments will be conducted at the Laboratory of Applied Mechanics of the Department of Industrial Engineering of the University of Salerno and they will be executed as follow: in order to have the possibility to immerse completely the tested tribo pairs in a defined quantity of oil, a ball on disk tribometer was used. The used apparatus was a WAZAU tribometer TRM100.

The apparatus allows to apply different test parameters: the normal force should be chosen in the range of 0–100 N, while the shaft angular velocity, imposed by a brushless electric motor, could be variable up to 3000 rpm. The

average lubricant temperature is controlled through a NiCr-Ni thermocouple in the oil reservoir and by an electric resistance. The tribo-pair will be constituted on a disk of diameter of 105 mm made by AISI D3 X210Cr12 alloy steel with a Young modulus of 210 GPa, hardness 60 HRC. The pin will be constituted of a AISI 52100 steel sphere of 8 mm in diameter. The tribo-pair (sphere/disc) will be lubricated by immersing it in a reservoir filled with the tested oil -220 ml lubricant bath- (Figure 3).

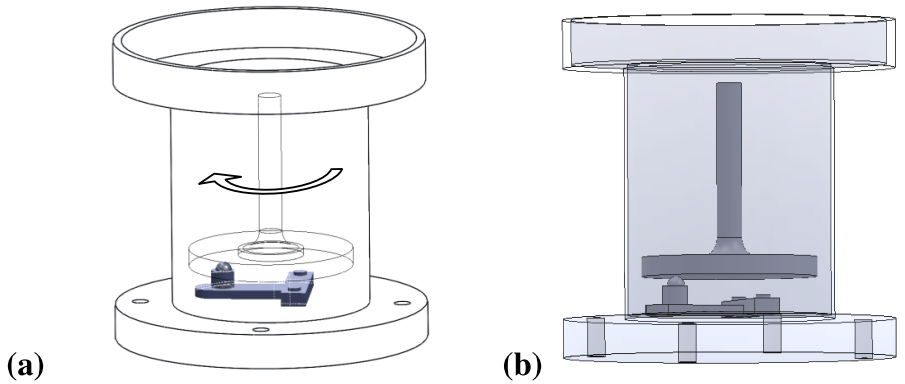

Figure 3. Tribometer scheme: a),b) schematic of tribosystem and vegetal oil reservoir

In order to achieve different lubrication modes, four normal loads will be imposed on the tribo pair of 6N, 8N, 10N, 12N, equivalent to a mean Hertz contact pressure respectively of 0.65 GPa, 0.71 GPa, 0.77 GPa, 0.81 GPa. The measurement of the normal force was performed through a force transducer. Three tests will be executed for each oil and each test will ran for 30 min, in which three constant acceleration ramps from 0 m/s to 1 m/s in sliding tangential ball velocity and three inverse decelerations ramps will be imposed. This procedure allows to achieve information on the wear of the contact specimens by taking in to account all the three fundamental lubrication modes.

After the tribological tests the three used oils will be shaken for 30 seconds to disperse the wear debris particles and will be put in an ultrasonic bath for 45 seconds to remove air bubbles. The oils will be analysed by using a novel optical technique based on the use of an apparatus available at the same Laboratory (*LaserNet Fines C* setup). The apparatus is an automated microscope able to capture by using a high power infrared laser source with sophisticated high speed (100 frames/s) camera (640 x 480 dpi) the images of the wear debris particles in the used oils. The captured images are stored and after classified by ausing a neural network algorithm trained on the basis of an extensive library of wear particles shapes achieved over the years by scientists who used microscopical and ferro graphical methods.

LaserNet system is able to store a great number of acquired images; in this way the statistical significance of the investigation can be assumed. The apparatus within an area of 1600 x 1200 μm accurately measures particles simultaneously. Air bubbles and water droplets (> 20 μm) are recognized, quantified and eliminated from the total particles count.

The statistical analysis of the obtained data will provide details about the comparative wear protection ability of the investigated oils.

Conclusions

In the framework of a running research, this paper aims to describe in details the design of the experiments which will be provided, in order to give a complete tribological characterization of the investigated vegetal oils.

Accounting for environmental, sustainability, availability in nature, and scientific issues will be selected the vegetal basestocks to be investigated and will be prepared the oil samples.

The experimental investigation will be devoted to both a physicochemical and to a tribological (friction and wear protection ability) characterization of the selected basestock.

The physicochemical characterization foresees the measurement of the density, the kinematic and the dynamic viscosity, the flash point and total acid number (TAN), while the tribological investigation will be based on novel reciprocating tribo-tests, able to characterize in each test all the lubrication mechanisms acting in the lubricated gap following the Stribeck approach. Subsequently, the accurate optical worn surfaces analysis and a novel approach based on the optical analysis of the used oils will be able to furnish detailed information about the wear type affecting the lubricated tribosystem. Even if in the present perspective paper no experimental results were showed, from the analysis of the firsts obtained data, the authors believe that the proposed novel experimentation protocol furnishes a promising procedure for the accurate and complete tribological investigation of vegetal base stocks, which should be usefully employed for obtaining a complete and accurate tribological investigation of the investigated vegetal base stocks by minimizing the required time for the experiments.

References

[1] A. Cameron, Basic Lubrication Theory. Wiley, New York (1976).
[2] Y.M. Shashidhara, S.R. Jayaram, Vegetable oils as a potential cutting fluid—An evolution, Tribology International 43 (2010) 1073–1081
[3] Kline & Company, Inc. Competitive intelligence for the global lubricants industry, 2004–2014. Kline & Company, Inc., 2006.

[4] Loredana P, Cosmina P, Geza B, Gabriela V, Remus N. Basestock oils for lubricants from mixtures of corn oil and synthetic diesters. J Am Oil Chem Soc 2008;85:71–6.
[5] HSE. Metal working fluids (MWF) exposure assessment, EH74/4. London: HSE Books; 2000.
[6] Nagendramma, Ponnekanti, and Savita Kaul. "Development of ecofriendly/biodegradable lubricants: An overview." Renewable and sustainable energy reviews 16.1 (2012): 764-774.
[7] Wang, Congxin, et al. "One-Step Hydrotreatment of Vegetable Oil to Produce High Quality Diesel-Range Alkanes." ChemSusChem 5.10 (2012): 1974-1983.
[8] D'Agostino, Vincenzo. Fondamenti di tribologia. Cooperativa universitaria editrice napoletana, 1984.
[9] Lansdown, Tony. Lubrication and lubricant selection. Professional Engineering Publishing, 2004.
[10] ASTM D445 - 65 Standard Method Of Test For Viscosity Of Transparent And Opaque Liquids (Kinematic And Dynamic Viscosities)
[11] ASTM D664 - 18e2 Standard Test Method for Acid Number of Petroleum Products by Potentiometric Titration
[12] ASTM G133 - 05(2016) Standard Test Method for Linearly Reciprocating Ball-on-Flat Sliding Wear
[13] Szeri, Andras Z. Fluid film lubrication. Cambridge university press, 2010.
[14] Gross, William A., et al. Fluid film lubrication. No. DOE/TIC-11301. John Wiley and Sons, Inc., New York, NY, 1980.